UNIVERSITÀ
DEGLI STUDI
DI PADOVA

Head Office: Università degli Studi di Padova

Department of Industrial Engineering

Ph.D. Course in Industrial Engineering
Curriculum Chemical and Environmental Engineering
32° SERIES

NUMERICAL AND EXPERIMENTAL METHODS FOR STREAM AND WETLAND MODELLING

Coordinator: Prof. Paolo Colombo
Supervisor: Prof. Andrea Marion
Co-Supervisor: Prof. Andrea Bottacin-Busolin

Ph.D. student: Eleonora Dallan

Abstract

The general aim of my research was the development of innovative numerical and experimental methods for the study of water bodies, in particular wetlands and streams. The use of constructed wetlands (CWs) for waste water treatment is one technique that has shown potential to remove a variety of contaminants including municipal, agricultural, industrial wastewater and storm water. Also, for terrestrial environments and human activities is of primary importance to ensure quality and health safety of rivers and streams. Water quality degradation is mostly caused by the transport and transformation of solutes (pollutants) in rivers. The study of solute transport in wetlands and in rivers appears scientifically significant within a Doctoral Degree in Industrial Engineering since it is related to anthropogenic impacts mainly of industrial origin on the natural environment and on ecosystem services, in particular on surface water bodies and aquatic ecosystems. For these reasons, the improvements of both numerical and experimental methods used for understanding transport phenomena in transitional environments (rivers and wetlands) has a fundamental role for achieving better knowledge on the pollutants removal processes in such zones and thus better management and design of these water bodies.

In Chapter 1 a short literature review is presented about: (i) hydrodynamics and removal performance modelling in constructed wetland systems, (ii) conservative and smart tracer techniques and (iii) solute transport modelling in rivers. Then the specific aims of my doctorate research are described.

Chapter 2 presents the numerical modelling developed in COMSOL Multiphysics for the study of suspended sediment transport in vegetated wetlands, with different vegetation densities. The removal efficiencies were estimated and compared for the different vegetation densities and grain sizes.

Chapter 3 presents the numerical modelling developed combining Telemac2D and Matlab codes for simulating hydrodynamics and solute transport in wetland with randomly generated bathymetries, but characterized by different statistical parameters determining different configurations of the bed forms. The removal efficiencies were then estimated and compared for the different bathymetries.

Chapter 4 introduces first activities carried out on numerical and experimental methods for streams and executed with a classical approach at the retention processes study. The

numerical model STIR was applied at several conservative tracer datasets, measured for the same reaches in different flow rate conditions. Classical retention parameters, such as diffusion coefficient, exchange rate, mean residence time, were calibrated and compared for the different flow rates.

Chapter 5 focuses on the development and application of an innovative numerical tool for the study of reactive and smart tracers. The theoretical basis of STIR-RST software tool is described, in particular about the introduction of parameters representing decay and transformation of the smart tracer and about the chance of choosing if the 2 storage zones are arranged in-series or in-parallel with the main channel. Finally it is shown its application on a smart tracer field test case where Resazurin was used.

Chapter 6 reports the experimental study developed for investigating the mass balance closure of the Resazurin-Resorufin (Raz-Rru) system at the cellular scale. In the designed laboratory experiments, the sorption and photodecay of the tracers were minimized and the use of different microbial communities allowed analysing recovery patterns independent of specific microbial species. For each test, total recovery (Raz + Rru) was monitored in the time for evaluating if tracer mass disappeared during the experiments for uptake by cells.

A summary of main results and conclusions obtained in this 3-years research is given in Chapter 7.

For an easier search of the bibliographic sources used in the text, references are given separately for each chapter and included at the end of the related chapter.

Sommario

L'obiettivo generale della mia ricerca è stato lo sviluppo di metodi numerici e sperimentali innovativi per lo studio dei corpi idrici, in particolare delle zone umide e dei corsi d'acqua. L'uso di zone umide artificiali ("constructed wetland", CW) per il trattamento delle acque reflue è una tecnica che ha mostrato il potenziale di rimuovere una varietà di contaminanti tra cui acque reflue municipali, agricole, industriali e acque piovane. Inoltre, garantire la qualità e la sicurezza sanitaria di fiumi e torrenti è di primaria importanza per gli ambienti terrestri e le attività umane. Il degrado della qualità dell'acqua è principalmente causato dal trasporto e dalla trasformazione dei soluti (inquinanti) nei fiumi. Lo studio del trasporto di soluti nelle zone umide e nei fiumi appare scientificamente significativo nell'ambito di un Dottorato in Ingegneria Industriale poiché è legato agli impatti antropogenici spesso di origine industriale sull'ambiente naturale e sui servizi ecosistemici, in particolare sui corpi idrici superficiali e sugli ecosistemi acquatici. Per questi motivi, il perfezionamento dei metodi numerici e sperimentali utilizzati per comprendere i fenomeni di trasporto in ambienti di transizione (fiumi e zone umide) ha un ruolo fondamentale per ottenere una migliore conoscenza dei processi di rimozione degli inquinanti in tali zone e quindi una migliore gestione e progettazione di questi corpi idrici .

Nel capitolo 1 viene presentata una breve rassegna della letteratura riguardante: (i) la modellazione dell'idrodinamica e delle prestazioni di rimozione nelle aree umide artificiali, (ii) le tecniche con traccianti conservativi e "smart" e (iii) la modellazione del trasporto di soluti nei fiumi. Infine vengono descritti gli obiettivi specifici della mia ricerca di dottorato.

Il capitolo 2 presenta la modellistica numerica sviluppata in COMSOL Multiphysics per lo studio del trasporto di sedimenti sospesi in aree umide vegetate, con diverse densità di vegetazione. Le efficienze di rimozione sono state stimate e confrontate per le diverse densità di vegetazione e granulometria dei sedimenti.

Il capitolo 3 presenta la modellistica numerica sviluppata combinando i codici Telemac 2D e Matlab per simulare l'idrodinamica ed il trasporto di soluti in aree umide con batimetrie generate casualmente, ma caratterizzate da parametri statistici diversi che determinano la diversa configurazione delle forme di fondo. Le efficienze di rimozione sono state quindi stimate e confrontate per le diverse batimetrie.

Il capitolo 4 introduce le prime attività condotte riguardo i metodi numerici e sperimentali per i fiumi e svolte utilizzando un approccio classico allo studio dei processi di

ritenzione. Il modello numerico STIR è stato applicato a diversi set di dati da tracciante conservativo, misurati per gli stessi tratti di fiume per diverse condizioni di portata. I classici parametri di ritenzione, come coefficiente di diffusione, tassi di scambio di massa, tempi medi di ritenzione, sono stati calibrati e confrontati per le diverse portate.

Il capitolo 5 si concentra sullo sviluppo e l'applicazione di un innovativo strumento numerico per lo studio di traccianti reattivi e "intelligenti" (smart). Viene descritta la base teorica del software STIR-RST, nello specifico riguardo l'introduzione di parametri che rappresentino il decadimento e la trasformazione del tracciante intelligente e riguardo la possibilità di scegliere se le due zone di ritenzione siano disposte in serie od in parallelo con il canale principale. Infine viene mostrata la sua applicazione ad un caso sperimentale, cioè un test di campo con tracciante "smart" in cui è stata utilizzata Resazurina.

Il capitolo 6 riporta lo studio sperimentale sviluppato per esaminare la chiusura del bilancio di massa del sistema resazurina-resorufina (Raz-Rru) a scala cellulare. Negli esperimenti di laboratorio progettati, l'assorbimento e il fotodecadimento dei traccianti sono stati ridotti al minimo e l'uso di diverse comunità microbiche ha permesso di studiare il recupero di massa indipendentemente da specifiche specie microbiche. Per ogni test, il recupero di massa totale (Raz + Rru) è stato monitorato nel tempo per valutare se la massa del tracciante scomparisse durante gli esperimenti a causa di un suo trattenimento da parte delle cellule.

Una sintesi dei principali risultati e conclusioni ottenuti in questi tre anni di ricerca è data nel Capitolo 7.

Per facilitare la ricerca delle fonti bibliografiche utilizzate nel testo, i riferimenti sono stati forniti separatamente per ogni capitolo e sono stati allegati al termine del relativo capitolo.

Content

List of figures

Chapter 1

1 Background and research aims

1.1 Introduction

Constructed Wetlands (CWs) for wastewater treatment are increasingly recognized as a suitable alternative to conventional water treatments combining valuable ecological services. Their use for waste water treatment has shown the potential for removing a variety of contaminants including municipal, agricultural, industrial wastewater and storm water. Although CWs can significantly improve water quality, proper design and accurate optimization of wetland properties are required to achieve high-level performance. One of the general aim of the present research was to obtain a more complete understanding of the removal processes of contaminants in wetlands. In particular, a numerical approach was implemented to address the definition of the most significant physical and ecological quantities affecting the efficiency of artificial phytodepurative environments.

In the last two decades, knowledge on mass transport processes in stream has seen a larger development than for wetlands. While numerical methods have been applied to both systems, experimental research using tracers to mimic the fate of contaminants has effectively been applied only to streams. This is mainly due to the fact that streams allow the application of one-dimensional models which is still an extremely valuable simplification when dealing with tracers technology. Application of tracer technique to two-dimensional water bodies like CWs can certainly been foreseen as a research target for the near future. At the time of this

thesis we are not there yet and this is the reason why my study on wetlands has found is natural confinement within the numerical work. Application of tracer technologies to wetlands, although considered as an option at the beginning of my doctorate research, was excluded at an early stage due to financial and temporal limitations. Then I focused fully on tracer techniques applied to one-dimensional water bodies, i.e. streams, looking at the current frontier of knowledge, which is where reactive tracers resides. In my research work, smart tracers were used in both field and lab activities to increase knowledge about biological activity in the hyphoreic zones. Conversely, an innovative numerical model was implemented expanding an existing multi-compartments model for conservative tracers. This numerical model was validated on a field smart-tracers dataset obtained in an Italian open channel. This technique can provide useful information on the interaction of hydrodynamic conditions and biological or metabolic respiration in aquatic ecosystems.

In the following sections, theoretical background and specific research aims are presented.

1.2 Numerical methods for wetland study

The numerical study of treatment wetlands focused on free water surface constructed wetlands (FWS CWs), which are man-made vegetated aquatic systems similar in appearance to natural marshes, with typical water depths of less than 0.5 m (Figure 1.1 and Figure 1.2). Free Water Surface (FWS) wetlands represent an efficient ecological system for treating several forms of wastewater thanks to biochemical processes linked to hydrodynamic processes. They are engineered to optimize the treatment conditions found in natural wetlands, that are combinations of water, substrate, plants, and microorganisms. The effectiveness of constructed wetlands in reducing contaminants is well documented in particular for effluent from secondary or tertiary treatment processes (Vymazal, 2013, 2014; Vymazal and Březinová, 2015). Several studies report about their use for treatment of a variety of contaminants: municipal wastewater, storm water, industrial wastewater, agricultural wastewater, road runoff, wood waste leachate, and landfill leachate (for example, in: Kipasika et al., 2014; Carleton et al., 2001; Wu et al., 2015; Maucieri et al., 2014; Gill et al., 2014; Tao et al., 2006; Yang and Tsai, 2011). Compared to technical treatment options such as activated sludge, they need larger specific surface area but in contrast they exhibit several benefits: lower operation and maintenance costs, tolerance against fluctuations of flow and pollution load, advantage of water reuse and recycling, provision of habitat for many organisms, a more natural and aesthetic appearance (Kadlec et al., 2000; Haberl et al., 2003).

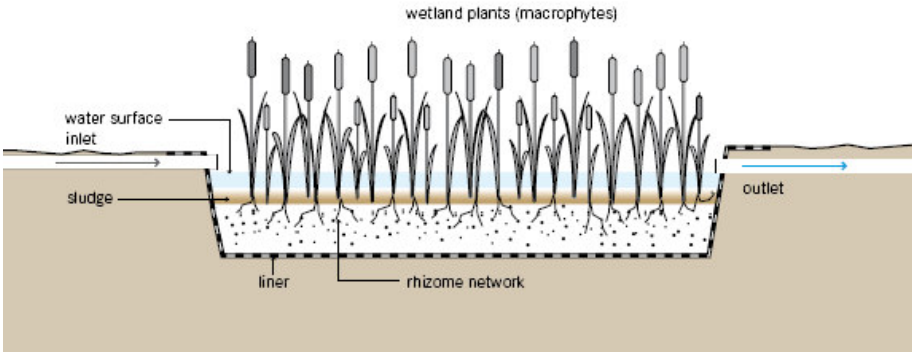

Figure 1.1 Basic elements of a Free Water Surface Constructed Wetland (Tilley et al, 2014)

Figure 1.2 Pictures of the constructed wetland Ca' di Mezzo (Codevigo, PD) (source: website of Consorzio di Bonifica Adige Euganeo, http://www.adigeuganeo.it) .

Although CWs can significantly improve water quality, they require proper designing and accurate optimization of their properties to achieve high-level performance (Kadlec and Wallace, 2009). Development of numerical modelling is fundamental for obtaining a more complete understanding of key parameters controlling the removal processes of contaminants in wetlands and for improving the existing design criteria. CWs were initially considered as black boxes in which water is treated, and their design was mainly based on empirical approaches and specific surface area requirements, or on simple first-order decay models (e.g., Brix and Johansen, 2004; Kadlec and Knight, 1996; Rousseau et al., 2004). A study by Kadlec (2000) showed the inadequacy of first-order models for the design of treatment wetlands. The CW system is effectively complex to understand and to model because of the large number of physical, chemical, and biological processes operating simultaneously and influencing each other. Wetlands ability to enhance water quality is mostly governed by hydrodynamics, controlling the residence time and thus the time available for water quality enhancement to take place. Treatment FWS wetlands have usually a water depth limited to

the maximum level plants can survive under flooded conditions, that is in the range 0.30÷0.60 m. Moreover, very low velocities are presents in order to ensure adequate retention times. For these factors, flow is usually in the laminar or transitional regime, and numerical models can't utilize turbulent-flow dependent equations commonly applied for modelling other type of free surface environments.

In recent years wetland numerical models have received increasing attention because they can provide insight into the black box and improvements in our understanding of the complexity of the wetland system. Some studies (Martinez and Wise, 2003; Keefe et al., 2004) using one-dimensional approach (transient storage models) provided in some cases a good approximation of the breakthrough curves, but they can't properly describe the different flow paths through vegetation and the main flow channels. Werner and Kadlec (2000) modeled the non ideal flow of CWs with a network of an infinite number of small stirred tanks distributed along a set of main plug flow channels. They suggested that new paradigms are needed for incorporating the description of short-circuiting and spatial distributions of vegetation. Experimental observation demonstrated that flow in constructed wetlands is not uniform as it was assumed in the initial approach to their design and this is one of the most influencing factors in decreasing residence time and wetland removal performance. Therefore, considering that spatial heterogeneity has a fundamental role in controlling the fate of contaminants, a two-dimensional approach appears more appropriate to describe transport dynamics in wetlands. Depth-averaged models are often applied for studying free surface systems because of their efficiency and reasonable accuracy. They can be considered accurate when the width-to-depth ratio of a basin is large and the vertical variations in mean-flow quantities are insignificant (Ye and McCorquodale 1997). The depth-averaged approach is adequate for modelling wetland hydrodynamics when not interested in modelling density stratification, which could be present in some periods of the year. Although two-dimensional (2-D) hydrodynamic models have already been used in the past (Persson et al., 1999; Somes et al., 1999), the formulation of more detailed models accounting for vegetation distribution or different configurations is relatively recent (Arega and Sanders, 2004; Jenkins and Greenway, 2005; Abbas et al., 2006; Ligthbody et al., 2007). Arega and Sanders (2004) presented a Godunov-based scheme as the basis of a tidal flow and transport model, emphasizing the ability of the scheme to validate using physically realistic and consistent flow resistance and dispersion parameters. Jenkins and Greenway (2005) developed a 2-D numerical model and studied hypothetical wetlands with aspect ratios in range of 1 to 18 and emergent fringing and banded vegetation. They concluded that higher aspect ratio increases

residence time with improvements on treatment ability of wetlands and that inappropriate layout of wetland vegetation results in poor performance of a wetland system. Abbas et al. (2006) simulated waste stabilization ponds of different aspect ratios and with multiple berms creating sinuosity. Higher length-to-width ratio and more internal baffles were effective in promoting biogeochemical oxygen demand (BOD) reduction. Lightbody (2007) found that improvements in reducing short-circuiting due to channels that cut through vegetated regions could be achieved with the insertion of unvegetated deep zones perpendicular to the flow path. However, the use of these models did not display a clear relationship between RTDs, vegetation density, vegetation distribution, bathymetric heterogeneity.

The Department of Industrial Engineering of the University of Padua was already involved in these topics as coordinator of the European research project "Hydrodynamic Transport in Ecologically Critical Heterogeneous Interfaces (HYTECH). In particular, part of the research group of Padova implemented a 2-dimensional numerical model to study the influence of design parameters on hydrodynamics and on processes of solid transport in wetlands and on their performance of purification (Musner et al., 2014), using COMSOL Multiphysics. Musner et al. (2014) used a two-dimensional depth-averaged model to study the residence time distribution of a tracer under different vegetation patterns in a channelized wetland. This model was then used for several studies. Savickis et al. (2016) performed numerical simulations of mass transport in a channelized wetland and analyzed the hydraulic efficiency. They found that the degree of channelization significantly affects wetland hydraulic performance and channel sinuosity reduces short-circuiting and increases hydraulic performance. Sabokrouhiyeh et al. (2016, 2017) investigated the relationship between hydraulic efficiency of a wetland and wetland shape and vegetation density. The simulated velocity fields demonstrated that wetland configuration (shape, inlet-outlet position, and width-to-length ratio) can have significant impact on the size of dead zone areas, which is also reflected in the RTD. Moreover, they found that for stem density higher than 300 stems/m^2, which is typical of treatment wetlands, the model predictions were not sensitive to the exact value of stem density selected, which simplifies the parameterization of models. These quantitative analyses of the effect of wetland configuration on removal efficiency could help engineers to achieve more efficient and cost-effective design solutions for wastewater treatment wetlands.

Since wetlands are characterized by a variety of ecological, biological, geochemistry, hydrodynamic processes, affecting the interfaces water/biota and water/sediment, it is essential to deepen their knowledge and adequately include them in modelling.

1.3 Solute transport in streams

1.3.1 Tracer technique

Tracers are usually soluble substances that follow the movement of water. They are useful for the study of the physical or chemical properties of the surface water, the sediment bed or the storage zones. Tracers allow to investigate the behavior of solid particles in the water (i.e. heavy suspended sediments, colloids, spores, etc.) or to understand the retardation or degradation potential of a substrate containing surface or sub-surface water. Tracer tests are conducted by injecting a tracer in a study reach. Injection can be performed with a pulse (slug) release or by a constant (plateau) concentration release of fixed duration of the tracer in the stream. The concentration distributions generated by the injection, known as breakthrough curves (BTCs), are measured over time at one or more sections downstream the injection point, at a distance greater than the length scale of transverse mixing. Concentration measurements can be taken directly by the use of on-line instruments placed in the flow, or by laboratory analysis of water samples taken in the field. BTCs contain information relevant to surface processes, namely advection and longitudinal dispersion, but also signatures of retention phenomena that produce deviations from the asymptotic dispersion regimes described by the classical advection–dispersion equation (ADE; Taylor, 1954). Tracer BTCs carry signatures of complex stream-storage zone mixing and exchange dynamics and the challenge of modelling and designing field tracer tests lies in the identification and the parameterization of these signatures. It is known that the tails of surface concentration distributions are affected by transient storage processes, but the major issue with their characterization is given by the detection limit of solute concentrations. The geometry of the study reaches and the choice of the tracer are thereby important factors for the success of an experimental campaign aiming to determine surface dispersion, fast exchange and the deeper transfer of solutes into the hyporheic zones.

Many kinds of substances can be used as tracers. Conservative tracers don’t decay or react with any other compounds, and are not subject to sorption and deposition processes; non-conservative tracers (reactive tracers) are instead subjected to decay or reaction. Environmental tracers are substances or water properties that naturally exist in the environment: chemical compounds, water properties (conductivity or temperature), microbes or algae. Their analysis can be particularly useful when groundwater and surface water, with different tracer content, mix at the sediment-water interface. For instance, Radon-222 is an environmental tracer released from radon-bearing rock; its concentrations are higher in groundwater than in surface water and can be used to identify groundwater inputs to a stream

(Yoneda et al., 1991). Anthropogenic environmental tracers result from their accidental release into the environment due to human activities. An example of anthropogenic environmental tracer is CFCs, which were released between the 1950s and 1980s and can be used to trace 50 year old water at a low detection limit (Busenberg and Plummer, 1992). Temperature could be used as environmental tracer in groundwater studies. Considering that groundwater has a relatively constant temperature compared to surface or stream water (Constantz, 1998), Conant (2004) investigated stream-groundwater exchange profiling water temperature through a depth profile of hyporheic sediments. Becker (2004) used heat as a tracer and estimated ground water discharge in a stream by combining meter measurements, stream temperature surveys, and heat transport modelling. The work of Anderson (2005) offers a comprehensive background review of existing literature on the use of temperature as a tracer.

Tracers that are purposely introduced in the environment are called “artificial” (Ward et al., 1998) and their addition in stream is widely used for the study of hyporheic retention and natural attenuation processes. Several artificial tracers can be used in river studies. For example, radioisotopes like tritium (conservative, 3H as tritiated water) and chromium (reactive, 51Cr as Cr (III)), were used in field studies in the Säva Brook, Sweden (Johansson et al., 2001; Jonsson and Worman, 2001). The use of different tracers at the same time permitted to detect the retardation of the non-conservative (reactive) tracer relative to the conservative (inert) tracer. The sorption of strontium (Sr) and potassium (K) tracers in bed sediments was investigated by Bencala and Walters, (1983). Other researchers used caesium (Cs) to investigate the sorption processes in aquatic sediments (Comans and Hockley, 1992; N.J. Comans et al., 1991; Nyffeler et al., 1984; Smith and Comans, 1996). In these studies Caesium (Cs) was an environmental tracer originated from the 1986 Chernobyl accident in the Ukraine. Nitrate was used for analyzing transport and retention in the hyporheic zone (Duff and Triska, 1990; Triska et al., 1993, 1990, 1989). Storey et al., (2003) used the 15N isotope to describe de-nitrification processes in laboratory column experiments with sediments cores.

An important group of tracer for hydrologic field studies in rivers and wetlands is represented by fluorescent dyes. Among a variety of commercial dyes available in a range of different colors, uranine, lissamine FF and rhodamine WT are the most used fluorescent water tracers (Wilson et al., 1986). Thanks to their relative low cost, high solubility, low toxicity and easy detection by fluorometric methods, fluorescent dyes have been widely used for stream tracing applications, especially rhodamine WT (some examples in: Atkinson and

Davis, 2000; Bencala, 1984; Bottacin-Busolin et al., 2011; Fernald et al., 2001). Among the fluorescent dyes, particular attention should be given to bio-reactive ("smart") tracers. Conservative tracers provide information about water transport and arrival time, but they have limitations in distinguishing the different stream compartments. In recent years, improvements have been obtained by the development of a smart tracer technique, which allows having information about microbiological activity and sediment-water interactions. Haggerty et al. (2008) proposed the use of Resazurin (Raz, blue colour, weak fluorescence) as smart tracer, converted in Resorufin (Rru, fluorescent pink colour) under reducing conditions. The Raz-Rru system has been successfully used by researchers to quantify parameters and fluxes related to water-sediment interface and metabolically active zone at the reach-scale: Argerich et al. (2011), Lemke, Liao, et al. (2013), González-Pinzón et al. (2014, 2015, 2016). Most of the hydrological studies using the Raz-Rru system have found that the total mass recovered (Raz+Rru) is smaller than the mass of Raz injected after accounting for dilution. This lack of mass balance closure has been reported as a non-ideality of this tracer system and it is still unclear what drives incomplete recovery: existence of additional reaction products, the long-term sorption of the tracers, some degree of photodecay, all combined, or some other mechanism of uptake at the cellular scale. Further study is needed for improving this smart tracer technique.

Tracer tests in surface water provide a picture of stream transport and exchange processes through BTCs of designed solute injections. Modern technologies and new generation tracers improved the quality of information collected with field tests, but adequate modelling is required for obtaining information from the measured datasets.

1.3.2 Numerical modelling

The understanding of solute transport processes has a fundamental role for improving water quality measures and ecological services of rivers and streams. The fate of solutes in natural stream is influenced by surface hydrodynamics, mass exchanges between the surface water and retention zones, biogeochemical processes. Over the last few decades, researchers have developed models and experimental techniques for studying the transport mechanisms of nutrients and pollutants in stream corridors. Usually, parameters for these models are calibrated to the datasets obtained by field tracer tests carried in the reach of interest. Most of the modelling frameworks are based on the advection-dispersion equations and the concept of transient storage zones interacting with the stream. Indeed, the classical ADE from the Taylor dispersion theory could give accurate results in simulation of transport in prismatic channels and rivers with relatively uniform cross-sections, but field studies indicated that in many cases

it fails in fitting measured concentration curves. For example, particularly in mountain pool-and-riffle streams, it was observed that BTCs have a lower peak concentration and longer tails than the ADE equation predictions (Godfrey and Frederick, 1970; Nordin and Sabol, 1974; Nordin and Troutman, 1980; Day, 1975). Some researchers modified the ADE with the addition of extra terms for taking into account the impact of stagnant areas that were so-called storage zones (Bencala et al., 1990; Bencala and Walters, 1983; Jackman et al., 1984; Runkel, 1998; Czernuszenko and Rowinski, 1997; Singh, 2003). Transient storage zones mainly include eddies, stream poolside areas, gravel bed, bed sediments, porous media of river bed and banks, stagnant areas behind flow obstructions such as big boulders, stream side vegetation, woody debris and so on (Jackson et al., 2013). In general, these areas affect solute transport by temporarily retaining and gradually releasing it, and this is reflected in an asymmetric shape in the observed BTCs which could not be explained by the classical ADE. Moreover, it is also affected by the opportunity for reactive pollutants to be in contact with streambed sediments that in-directly affect solute sorption, especially in low-flow conditions (Bencala, 1983, 1984; Bencala et al., 1990; Bencala and Walters, 1983). A widely applied model developed with this concept of storage zones was the Transient Storage Model (TSM), presented by Bencala and Walters (1983), and it served as basis for many single-storage-zone one-dimensional models, for example, for the OTIS and OTIS-P models (Runkel and Chapra, 1993; Runkel, 1998). These models improved the study of solute transport in rivers, but they could not discriminate between different types of storage zones, characterized by different flow conditions, exchange mechanisms, biogeochemical conditions.

New models were developed with two-storage zones, discerning surface transient storage (STS) and hyporheic transient storage (HTS): Choi et al., 2000, Marion et al., 2008, Briggs et al., 2009. In particular, the Solute Transport in River (STIR) model (Marion et al., 2008, Bottacin-Busolin et al, 2011) allows to separate the processes using a stochastic approach to determine the residence time distribution (RTD) of distinct storage domains and proposes several forms of the RTDs.

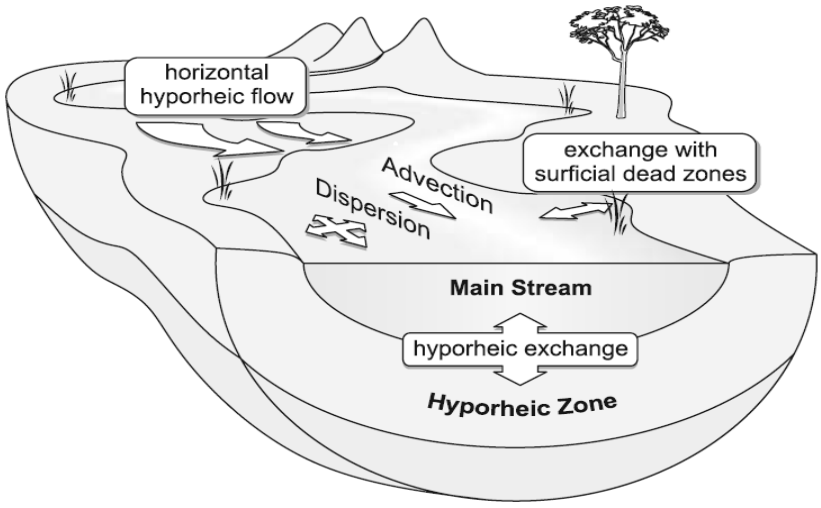

Figure 1.3 Sketch of the main transport processes acting in a river. In the main stream, advection and hydrodynamic dispersion govern the downstream transport of solutes. Moreover, it is affected by mass exchanges with different retention zones: underlying sediments, where adsorption process may take place; superficial dead zones, typically vegetated pockets; horizontal hyporheic flows induced by planimetric variation of the stream direction. (Marion et al., 2008)

Other descriptions of the hyporheic exchange have been implemented, for example in Haggerty and Reeves (2002), Worman et al. (2002), Deng et al. (2006), Boano et al. (2007), Kelly at al. (2017). The Solute Transport and Multirate Mass Transfer - Linear Coordinates (STAMMT-L) proposed by Haggerty and Reeves (2002) was the first model used to represent wide ranges of storage timescales in rivers. It used an advection-dispersion mass transfer equation (ADMTE), where a source-sink term accounting for mass exchange with immobile (storage) domains was added to the classical advection-dispersion equation (ADE). Worman et al (2002) proposed the advective storage path model and expressed the hyporheic residence time distribution using the advective pumping theory. The fractional model of Deng et al. (2006) used the fractional advection-dispersion equation (FADE). FracFit (Kelly et al., 2017) is a parameter estimation tool supporting four different fractional models. In Boano et al. (2007) the continuous time random walks (CTRW) theory was the framework for modelling the solute transport in stream. Most of 2-storage-zones models have a "competing" structure, which are storage zones acting in parallel with the main channel. Kerr et al. (2013) proposed a "nested" model, where storage zones are arranged in series, and demonstrated that calibrated model parameters were affected by the model structure and this was better shown using a reactive tracer.

As mentioned above, transient storage zones also differ for their biogeochemical characteristics and this factor affects the biological activity. Smart tracer technique has the potential to enhance our understandings about biogeochemical features of the stream.

Together with this new technique, adequate models have been developed for the estimation of parameters representing exchange between the surface and hyporheic zones. These models aim to define parameters for describing both physical and biochemical features of the river compartments. They are optimized by calculation of the best fit between measured and simulated breakthrough curves (Argerich et al., 2011; Lemke, Liao, et al., 2013; Yakirevich et al., 2017). For example, Argerich et al. (2011) developed a model separating the transient storage in a metabolically active part and a metabolically inactive storage (MATS-MITS model). Lemke, Liao, et al. (2013) demonstrated that a joint fit of conservative and reactive tracer gives a different transport parameters estimation from that obtained by fitting conservative data only, and they used a Markov chain Monte Carlo approach to avoid the problem of dependency by initial guess. Yakirevich et al. (2017) developed a STS-HTS model for smart tracers and compared it with a MATS-MITS model, finding better fit but uncertain results when STS-HTS calibrates all reaction parameters for all model compartments.

1.4 Research aims

This research aimed to obtain a more complete understanding of the removal processes of contaminants in wetlands and streams and to improve models and experimental techniques for their study and the quantification of physical and ecological parameters.

The main general intents of the research were:

(i) the study with numerical modelling of some characteristics of the wetlands, in particular bathymetry and vegetation distribution, for investigating their effects on the purification efficiency;

(ii) the improvement of experimental techniques to have new understandings about the transformation processes of the organic matter in water bodies,

(iii) the analysis of experimental tracer datasets in order to link mass exchange, metabolic activity, retention processes.

The specific goals of my research, and activities carried for achieving them, were:

(i) investigation on effect of vegetation density on sedimentation in wetlands, using the COMSOL model developed in previous studies (Musner et al., 2004),

(ii) development of a new numerical modelling for wetland, using Telemac-2D, for including the analysis of bathymetric heterogeneity (flat, isotropic and anisotropic bed forms),

(iii) application of original STIR model (Marion et al., 2008) for the study of solute transport in a stream at different flow rates, in collaboration with prof. Wallis (Heriot-Watt University, UK),

(iv) updating of STIR model, in collaboration with prof. Bottacin-Busolin (University of Manchester, UK) for application on smart tracer datasets and for including in-series and in-parallel arrangements for storage zones,

(v) laboratory experiments to investigate mass balance of smart tracers at the cellular scale, in collaboration with prof. Gonzalez-Pinzon's group at University of New Mexico.

In the following chapters, each of these activities is widely described.

1.5 Bibliography

Abbas, H., Nasr, R., Seif, H., (2006). Study of waste stabilization pond geometry for the wastewater treatment efficiency. Ecol. Eng. 28, 25–34. doi:10.1016/j.ecoleng.2006.03.00

Anderson, M.P., (2005). Heat as a Ground Water Tracer. Ground Water 43, 951–968. doi:10.1111/j.1745-6584.2005.00052.x

Arega, F., Sanders, B.F., (2004). Dispersion model for tidal wetlands. J. Hydraul. Eng. 130, 739– 754. doi:10.1061/(ASCE)0733-9429(2004)130:8(739)

Argerich, A., Haggerty, R., Marti, E., Sabater, F., & Zarnetske, J. (2011). Quantification of metabolically active transient storage (MATS) in two reaches with contrasting transient storage and ecosystem respiration. Journal of Geophysical Research, 116, G03034. https://doi.org/ 10.1029/2010JG001379

Atkinson, T.C., Davis, P.M., (2000). Longitudinal dispersion in natural channels: l. Experimental results from the River Severn, U.K. Hydrol. Earth Syst. Sci. 4, 345–353. doi:10.5194/hess4-345-2000

Becker, M.W., Georgian, T., Ambrose, H., Siniscalchi, J., Fredrick, K., (2004). Estimating flow and flux of ground water discharge using water temperature and velocity. J. Hydrol. 296, 221–233. doi:10.1016/j.jhydrol.2004.03.025

Bencala, K. E., Mcknight, D. M., and Zellweger, G. W. (1990): Characterization of transport in an acidic and metal-rich mountain stream based on a lithium tracer injection and simulations of transient storage, Water Resour. Res., 26, 989–1000

Bencala, K. E. and Walters, R. A. (1983): Simulation of Solute Transport in a Mountain Pool-and-Riffle Stream: A Transient Storage Model, Water Resour. Res., 19, 718–724, doi:10.1029/wr019i 003p00718

Bencala,K.E. (1984): Interactions of solutes and stream bed sediment:A dynamic analysis of coupled hydrologic and chemical processes that determine solute transport, Water Resour. Res., 20, 1804– 1814, doi:10.1029/WR020i012p01804

Boano, F., A. I. Packman, A. Cortis, R. Revelli, and L. Ridolfi (2007b), A continuous time random walk approach to the stream transport of solutes, *Water Resour. Res.*, 33, W10425, doi:10.1029/2007WR006062.

Bottacin-Busolin, A., Marion, A., Musner, T., Tregnaghi, M., Zaramella, M., (2011). Evidence of distinct contaminant transport patterns in rivers using tracer tests and a multiple domain retention model. Adv. Water Resour. 34, 737–746. doi:10.1016/j.advwatres.2011.03.005

Briggs, M. A., M. N. Gooseff, C. D. Arp, and M. A. Baker (2009), A method for estimating surface transient storage parameters for streams with concurrent hyporheic storage, *Water Resour. Res.*, 45, W00D27, doi:10.1029/2008WR006959

Brix, H., and N.H. Johansen. (2004). Guidelines for vertical fl ow constructed wetland systems up to 30 PE. (In Danish.) Økologisk Byfornyelse og Spildevandsrensning No. 52. Miljøstyrelsen, Miljøministeriet, Copenhagen, Denmark.

Busenberg, E., Plummer, L.N., 1992. Use of chlorofluorocarbons (CCl 3 F and CCl 2 F 2) as hydrologic tracers and age-dating tools: The alluvium and terrace system of central Oklahoma. Water Resour. Res. 28, 2257–2283. doi:10.1029/92WR01263

Carleton, J.N., Grizzard, T.J., Godrej, a. N., Post, H.E., (2001). Factors affecting the performance of stormwater treatment wetlands. Water Res. 35, 1552–1562. doi:10.1016/S00431354(00)00416-4

Choi, J., J. W. Harvey, and M. H. Conklin, (2000), Characterizing multiple timescales of stream and storage zone interaction that affect solute fate and transport in streams, *Water Resour. Res.*, 36, 1511– 1518, doi:10.1029/2000WR900051.

Comans, R.N.J., Hockley, D.E. (1992). Kinetics of cesium sorption on illite. Geochim. Cosmochim. Acta 56, 1157–1164. doi:10.1016(/0016-7037(92)90053-L

Conant, B., 2004. Delineating and Quantifying Ground Water Discharge Zones Using Streambed Temperatures. Ground Water 42, 243–257. doi:10.1111/j.1745-6584.2004.tb02671.x

Constantz, J., 1998. Interaction between stream temperature, streamflow, and groundwater exchanges in alpine streams. Water Resour. Res. 34, 1609–1615. doi:10.1029/98WR00998

Czernuszenko, W. and Rowinski, P. (1997): Properties of the dead-zone model of longitudinal dispersion in rivers, J. Hydraul. Res., 35, 491–504, doi:10.1080/00221689709498407

Day, T. J. (1975) : Longitudinal dispersion in natural channels, Water Resour. Res., 11, 909–918, doi:10.1029/WR011i006p00909

Deng, Z.-Q., L. Bengtsson, and V. P. Singh (2006), Parameter estimation for fractional dispersion model for rivers, *Environ. Fluid. Mech.*, 6 (5), 451– 475.

Duff, J.H., Triska, F.J., (1990). Denitrifications in Sediments from the Hyporheic Zone Adjacent to a Small Forested Stream. Can. J. Fish. Aquat. Sci. 47, 1140–1147. doi:10.1139/f90-133

Fernald, A.G., Wigington, P.J., Landers, D.H., (2001). Transient storage and hyporheic flow along the Willamette River, Oregon: Field measurements and model estimates. Water Resour. Res. 37, 1681–1694. doi:10.1029/2000WR900338

Gill, L.W., Ring, P., Higgins, N.M.P., Johnston, P.M., (2014). Accumulation of heavy metals in a constructed wetland treating road runoff. Ecol. Eng. 70, 133–139. doi:10.1016/j.ecoleng.2014.03.056

Godfrey, R. G. and Frederick, B. J. (1970): Stream dispersion at selected sites, US Government Printing Office

González-Pinzón, R., Haggerty, R., & Argerich, A. (2014). Quantifying spatial differences in metabolism in headwater streams. Freshwater Science, 33(3), 798–811. https://doi.org/10.1086/677555

González-Pinzón, R., Ward, A. S., Hatch, C. E., Wlostowski, A. N., Singha, K., Gooseff, M. N., et al. (2015). A field comparison of multiple techniques to quantify groundwater–surface-water interactions. Freshwater Science, 34(1), 139–160. https://doi.org/10.1086/679738

González-Pinzón,R.,Peipoch,M.,Haggerty,R.,Martí,E.,&Fleckenstein,J.H. (2016). Night time and day time respiration in a head water stream. Ecohydrology, 9(1), 93–100. https://doi.org/10.1002/eco.1615

Haberl, R., S. Grego, G. Langergraber, R.H. Kadlec, A.R. Cicalini, S. Martins Dias, J.M. Novais, S. Aubert, A. Gerth, H. Th omas, and A. Hebner. (2003). Constructed wetlands for the treatment of organic pollutants. J. Soils Sediments 3:109–124.

Haggerty, R., A. Argerich, and E. Martí (2008), Development of a “smart” tracer for the assessment of microbiological activity and sediment-water interaction in natural waters: The resazurin-resorufin system, Water Resour. Res., 44, W00D01, doi:10.1029/2007WR006670.

Haggerty, R., and P. C. Reeves (2002), STAMMT□L 1.0, formulation and user's guide, *Tech. Rep. ERMS #520308*, Sandia Natl. Lab., Albuquerque, N. M.

Jackman, A., Walters, R., and Kennedy, V. (1984): Transport and concentration controls for Chloride, Strontium, potassium and lead in Uvas Creek, a small cobble-bed stream in Santa Clara County California, USA:2,Mathematical modelling, J.Hydrol.,75,111–141, doi:10.1016/0022-1694(84)90046-5

Jackson, T. R., Haggerty, R., and Apte, S. V. (2013): A fluid-mechanics based classification scheme for surface transient storage in riverine environments: quantitatively separating surface from hyporheic transient storage, Hydrol. Earth Syst. Sci., 17, 2747– 2779, doi:10.5194/hess-17-2747-2013

Jenkins, G. a., Greenway, M., (2005). The hydraulic efficiency of fringing versus banded vegetation in constructed wetlands. Ecol. Eng. 25, 61–72. doi:10.1016/j.ecoleng.2005.03.001

Johansson, H., Jonsson, K., Forsman, K., Worman, A., (2001). Retention of conservative and sorptive solutes in streams — simultaneous tracer experiments. Sci. Total Environ. 266, 229–238. doi:10.1016/S0048-9697(00)00758-0

Jonsson, K., Worman, A., (2001). Effect of sorption kinetics on the transport of solutes in streams. Sci. Total Environ. 266, 239–247. doi:10.1016/S0048-9697(00)00743-9

Kadlec, R.H. (2000). The inadequacy of first-order treatment kinetic models. Ecol. Eng. 15:105–119.

Kadlec, R.H., and R.L. Knight. (1996). Treatment wetlands. CRC Press, Boca Raton, FL.

Kadlec, R.H., R.L. Knight, J. Vymazal, H. Brix, P. Cooper, and R. Haberl (ed.). 2000. Constructed wetlands for pollution control: Processes, performance, design, and operation. IWA Scientifi c and Technical Rep. 8. Int. Water Assn., London.

Kadlec, R., Wallace, S., (2009). Treatment Wetlands, Second edition. CRC Press, Boca raton, Florida.

Keefe, S.H., Daniels, J.S., Runkel, R.L., Wass, R.D., Stiles, E.A., Barber, L.B., (2010). Influence of hummocks and emergent vegetation on hydraulic performance in a

surface flow wastewater treatment wetland. Water Resour. Res. 46, W11518. doi:10.1029/2010wr009512

Kelly, J. F., Bolster, D., Meerschaert, M. M., Drummond, J. D., and Packman, A. I. (2017), FracFit: A robust parameter estimation tool for fractional calculus models, *Water Resour. Res.*, 53, 2559– 2567, doi:10.1002/2016WR019748.

Kerr, P.C. , Gooseff, M.N., Bolster, D. (2013), The significance of model structure in one-dimensional stream solute transport models with multiple transient storage zones – competing vs. nested arrangements, Journal of Hydrology, Volume 497, 2013, Pages 133-144, doi:10.1016/j.jhydrol.2013.05.013.

Kipasika, H.J., Buza, J., Lyimo, B., Miller, W.A., Njau, K.N., (2014). Efficiency of a constructed wetland in removing microbial contaminants from pre-treated municipal wastewater. Phys. Chem. Earth, Parts A/B/C 72–75, 68–72. doi:10.1016/j.pce.2014.09.00

Lightbody, A., Nepf, H., Bays, J., (2007). Mixing in deep zones within constructed treatment wetlands. Ecol. Eng. 29 (2), 209–220. http://dx.doi.org/10.1016/j.ecoleng. 2006.11.001.

Lemke, D., Liao, Z. J., Wohling, T., Osenbruck, K., & Cirpka, O. A. (2013). Concurrent conservative and reactive tracer tests in a stream undergoing hyporheic exchange. Water Resources Research, 49, 3024–3037. https://doi.org/10.1002/wrcr.20277

Marion, A., M. Zaramella, and A. Bottacin-Busolin (2008b), Solute transport in rivers with multiple storage zones: The STIR model, *Water Resour. Res.*, 44, W10406, doi:10.1029/2008WR007037

Martinez, C.J., and W.R.Wise (2003). Analysis of constructed treatment wetland hydraulics with the transient storage model OTIS, Ecological Engineering, 20(3), 211–222.

Maucieri, C., Salvato, M., Tamiazzo, J., Borin, M., (2014). Biomass production and soil organic carbon accumulation in a free water surface constructed wetland treating agricultural wastewater in North Eastern Italy. Ecol. Eng. 70, 422–428. doi:10.1016/j.ecoleng.2014.06.020

Musner, T., Bottacin-Busolin, A., Zaramella, M., Marion, A., (2014). A contaminant transport model for wetlands accounting for distinct residence time bimodality. J. Hydrol. 515, 237– 246. doi:10.1016/j.jhydrol.2014.04.04

N.J. Comans, R., Haller, M., De Preter, P., (1991). Sorption of cesium on illite: Non-equilibrium behaviour and reversibility. Geochim. Cosmochim. Acta 55, 433–440. doi:10.1016/00167037(91)90002-M

Nyffeler, U.P., Li, Y.-H., Santschi, P.H., (1984). A kinetic approach to describe trace-element distribution between particles and solution in natural aquatic systems. Geochim. Cosmochim. Acta 48, 1513–1522. doi:10.1016/0016-7037(84)90407-1

Nordin, C. F. and Sabol, G. V. (1974): Empirical data on longitudinal dispersion in rivers, WRI, 74–20, 372 pp.

Nordin, C. F. and Troutman, B. M. (1980): Longitudinal dispersion in rivers: The persistence of skewness in observed data, Water Resour. Res., 16, 123–128, doi:10.1029/WR016i001p00123

Persson, J., Somes, N., Wong, T., (1999). Hydraulics efficiency of constructed wetlands and ponds. Water Sci. Technol. 40, 291–300. doi:10.1016/S0273-1223(99)00448-5

Rousseau, D.P.L., P.A. Vanrolleghem, and N. De Pauw. (2004). Model-based design of horizontal subsurface fl ow constructed treatment wetlands: A review. Water Res. 38:1484–1493.

Runkel, R. L. (1998): One-dimensional transport with in flow and storage (otis): a solute transport model for streams and rivers, Water Resources Investigations Report

Runkel, R. L., and S. C. Chapra (1993), An efficient numerical solution of the transient storage equations for solute transport in small streams, *Water Resour. Res.*, 29, 211–215, doi:10.1029/92WR02217.

Sabokrouhiyeh, N., Bottacin-Busolin, A., Nepf, H., Marion, A., (2016). Effects of vegetation density and wetland aspect ratio variation on hydraulic efficiency of wetlands, GeoPlanet: Earth and Planetary Sciences. doi:10.1007/978-3-319-27750-9_9

Sabokrouhiyeh, N., Bottacin-Busolin, A., Savickis, J., Nepf, H., Marion, A., (2017). A numerical study of the effect of wetland shape and inlet-outlet configuration on wetland performance. Ecol. Eng. 105, 170–179. doi:10.1016/j.ecoleng.2017.04.062

Savickis, J., Bottacin-Busolin, A., Zaramella, M., Sabokrouhiyeh, N., Marion, A., (2016). Effect of a meandering channel on wetland performance. J. Hydrol. 535. doi:10.1016/j.jhydrol.2016.01.082

Singh, S. K. (2003): Treatment of stagnant zones in riverine advection-dispersion, J. Hydraul. Eng., 129, 470–473, doi:10.1061/(ASCE)0733-9429(2003)129:6(470)

Smith, J.T., Comans, R.N.J., (1996). Modelling the diffusive transport and remobilisation of 137Cs in sediments: The effects of sorption kinetics and reversibility. Geochim. Cosmochim. Acta 60, 995–1004. doi:10.1016/0016-7037(96)00030-0

Somes, N.L.G., Bishop, W.A., Wong, T.H.F., (1999). Numerical simulation of wetland hydrodynamics. Environ. Int. 25, 773–779. doi:10.1016/S0160-4120(99)00058-6

Storey, R.G., Howard, K.W.F., Williams, D.D., (2003). Factors controlling riffle-scale hyporheic exchange flows and their seasonal changes in a gaining stream: A three-dimensional groundwater flow model. Water Resour. Res. 39. doi:10.1029/2002WR001367

Tao, W., Hall, K.J., Duff, S.J.B., (2006). Performance evaluation and effects of hydraulic retention time and mass loading rate on treatment of woodwaste leachate in surface-flow constructed wetlands. Ecol. Eng. 26, 252–265. doi:10.1016/j.ecoleng.2005.10.006

Taylor, G. I. (1954), The dispersion of matter in turbulent flow through a pipe, Proc. Roy. Soc. A, 223, 446–468.

Tilley, E., Ulrich, L., Luethi, C., Reymond, P. and Zurbruegg, C. (2014) Compendium of Sanitation Systems and Technologies. 2nd Revised Edition, Swiss Federal Institute of Aquatic Science and Technology (Eawag), Duebendorf.

Triska, F.J., Duff, J.H., Avanzino, R.J., (1993). Patterns of hydrological exchange and nutrient transformation in the hyporheic zone of a gravel-bottom stream: examining terrestrial aquatic linkages. Freshw. Biol. 29, 259–274. doi:10.1111/j.1365-2427.1993.tb00762.x

Triska, F.J., Duff, J.H., Avanzino, R.J., (1990). Influence of Exchange Flow Between the Channel and Hyporheic Zone on Nitrate Production in a Small Mountain Stream. Can. J. Fish. Aquat. Sci. 47, 2099–2111. doi:10.1139/f90-235

Triska, F.J., Kennedy, V.C., Avanzino, R.J., Zellweger, G.W., Bencala, K.E., (1989). Retention and Transport of Nutrients in a Third-Order Stream: Channel Processes. Ecology 70, 1877– 1892. doi:10.2307/1938119

Vymazal, J., (2014). Constructed wetlands for treatment of industrial wastewaters: A review. Ecol. Eng. 73, 724–751. doi:10.1016/j.ecoleng.2014.09.034

Vymazal, J., (2013). Emergent plants used in free water surface constructed wetlands: A review. Ecol. Eng. 61, 582–592. doi:10.1016/j.ecoleng.2013.06.023

Vymazal, J., Březinová, T., 2015. The use of constructed wetlands for removal of pesticides from agricultural runoff and drainage: A review. Environ. Int. 75, 11–20. doi:10.1016/j.envint.2014.10.026

Ward, R.S., Williams, A.T., Barker, J.A., Brewerton, L.J., Gale, I.N., (1998). Groundwater tracer tests: a review and guidelines for their use in British aquifers. British Geological Survey, London

Werner, T.M., and R.H. Kadlec. (2000). Wetland residence time modelling. Ecol. Eng. 15:77–90.

Wilson, J., Cobb, E., Kilpatrick. FA, (1986). Fluorometric procedures for dye tracing. Department of the Interior, US Geological Survey.

Wörman, A., A. I. Packman, and K. Jonsson (2002), Effect of flow□induced exchange in hyporheic zones on longitudinal transport of solutes in stream and rivers, *Water Resour. Res.*, 38(1), 1001, doi:10.1029/2001WR000769.

Wu, S., Wallace, S., Brix, H., Kuschk, P., Kirui, W.K., Masi, F., Dong, R., (2015). Treatment of industrial effluents in constructed wetlands: Challenges, operational strategies and overall performance. Environ. Pollut. 201, 107–120. doi:10.1016/j.envpol.2015.03.006

Yang, L., Tsai, K.-Y., (2011). Treatment of landfill leachate with high levels of ammonia by constructed wetland systems. J. Environ. Sci. Heal. 46, 736–741. doi:10.1080/10934529.2011.571586

Yakirevich, A.; Shelton, D.; Hill, R.; Kiefer, L.; Stocker, M.; Blaustein, R.; Kuznetsov, M.; McCarty, G.; Pachepsky, Y. (2017) Transport of Conservative and “Smart” Tracers in a First-Order Creek: Role of Transient Storage Type. Water 2017, 9, 485

Ye, J., and McCorquodale, J. A.(1997a). “Depth-averaged hydrodynamic model in curvilinear collocated grid.”J. Hydr. Engrg., ASCE, 123(5), 380–388.

Yoneda, M., Inoue, Y., Takine, N., (1991). Location of groundwater seepage points into a river by measurement of 222Rn concentration in water using activated charcoal passive collectors. J. Hydrol. 124, 307–316. doi:10.1016/0022-1694(91)90021-9

Chapter 2

2 Numerical study of sedimentation in uniformly vegetated wetlands [1]

2.1 Introduction

Free water surface constructed wetlands (FWS CWs) have received increasing attention in recent years due to their potential for treatment of municipal, agricultural, industrial wastewater and storm water. Although CWs can improve water quality significantly, satisfactory performance depends on an efficient wetland design. The development of more effective criteria and protocols based on measurable physical and ecological parameters requires an improved understanding of contaminant removal processes in these complex environments.

In the last decades, growing interest in the construction and restoration of wetlands (Marion et al. 2014) has led to an increasing development of conceptual, analytical and numerical models for wetlands. Initial studies analyzed wetland performance using

1 The content of this chapter is described in: Dallan E., Bottacin-Busolin A., Sabokrouhiyeh N., Tregnaghi M., Marion A. (2018) *Numerical Study of Sedimentation in Uniformly Vegetated Wetlands*. In: Kalinowska M., Mrokowska M., Rowiński P. (eds) Free Surface Flows and Transport Processes. GeoPlanet: Earth and Planetary Sciences. Springer, Cham; indexed by Scopus and by Web of Science. Doi: 10.1007/978-3-319-70914-7_9. It was also presented at 37th International School of Hydraulics, Łąck, Poland (May 2017).

continuously stirred tank reactor (CSTR) models (Kadlec and Knight, 1996; Stone et al., 2004). Subsequent studies used experimental, numerical and analytical methods to analyze wetland processes. Most of the mechanistic models presented in the literature have been developed for urban wastewater treatment in subsurface flow CWs (SSFCWs), e.g. Constructed Wetlands 2D (CW2D) (Langergraber, 2001), whilst models for free water surface constructed wetlands (FWSCWs) remain fewer (Gargallo at al., 2016). Since the fate of contaminants in wetlands depends on the heterogeneity of various factors such as vegetation, two- or three-dimensional models appear more appropriate to describe wetland processes. Recent 2D modelling approaches combine shallow water depth-averaged hydrodynamic models with advection-dispersion models for mass transport. These approaches have been applied to investigate the effect of wetland geometry and vegetation distribution (Musner et al., 2014; Savickis et al., 2016; Sabokrouhiyeh et al., 2016). Wetland contaminant removal is also influenced by sediment transport processes, because they influence soil particles retention, water transparency, interactions between pathogens and dissolved oxygen exchanges across the water-sediment interface.

The aim of this study was to analyze the deposition of suspended sediment in FWS CWs. Numerical simulations are performed using the model presented by Musner et al. (2014), adapted to include a first simplified description of sediment transport, settling and resuspension. The analysis focused on the effect of grain size and vegetation density on sediment removal in a uniformly vegetated wetland. The overarching aim of this research was to develop practical criteria for optimal wetland design based on an improved physical understanding of the fate of sediments in free surface wetlands.

2.2 Theoretical background

2.2.1 Two-dimensional wetland model

A 2-dimensional numerical model of a wetland was developed to simulate flow dynamics and transport of suspended sediment. Assuming that vertical gradients are smaller than the horizontal gradients, the transport of a solute in a wetland can be represented by a two-dimensional depth-averaged model. This assumption has often been used in wetland studies (Somes et al., 1999; Arega and Sanders, 2004; Jenkins and Greenway, 2005) and is consistent with the simplified wetland topography and geometry analyzed in this work.

The hydrodynamic model solved the 2-D shallow-water equations, whereas the transport model solved the advection-dispersion equation with a source/sink term. In the hydrodynamic model, the effect of vegetation was represented as an equivalent flow

resistance that depended on vegetation density, stem diameter and submerged stem length. The solute transport model relied on the velocity field predicted by the hydrodynamic model and took into account the additional mechanical and turbulent dispersion induced by vegetation via an appropriately defined dispersion tensor. In the next paragraphs an abridge description of the mathematical formulation of the model is presented. The detailed formulation can be found in Musner et al. (2014). The model flow and solute transport equations were solved using a Finite Element formulation with quadratic shape functions.

2.2.2 Hydrodynamic model

The governing equations included mass conservation Eq. (2.1) and the conservation of linear momentum in the horizontal plane Eqs. (2.2) - (2.3). Assuming hydrostatic pressure, stationary flow, negligible wind and Coriolis forces, the depth-averaged velocity field and water depth can be described by the following equations (Wu, 2007):

$$\frac{\partial(hU_x)}{\partial x}+\frac{\partial(hU_y)}{\partial y}=0 \tag{2.1}$$

$$\frac{\partial(hU_x{}^2)}{\partial x}+\frac{\partial(hU_xU_y)}{\partial y}=-gh\frac{\partial(z_s)}{\partial x}-\frac{\tau_{bx}}{\rho}-\frac{\tau_{vx}}{\rho} \tag{2.2}$$

$$\frac{\partial(hU_xU_y)}{\partial x}+\frac{\partial(hU_y{}^2)}{\partial y}=-gh\frac{\partial(z_s)}{\partial y}-\frac{\tau_{by}}{\rho}-\frac{\tau_{vy}}{\rho} \tag{2.3}$$

where: U_x, U_y, velocity components along the x- and y-direction, respectively; h, water depth; z_s, water surface elevation; ρ, water density; $\tau_{bx}$and τ_{by}, bed shear stresses; τ_{vx} and τ_{vy}, vegetation drag stresses in the x- and y- direction, respectively. Equations (2.2) and (2.3) assume that Reynolds stresses are negligible compared to bed and vegetative resistance.

Bed shear stresses were determined from the following equations (Kadlec and Wallace, 2008):

$$\tau_{bx}=\rho C_bU_x\sqrt{U_x{}^2+U_y{}^2} \tag{2.4}$$

$$\tau_{by}=\rho C_bU_y\sqrt{U_x{}^2+U_y{}^2} \tag{2.5}$$

in which the bed-drag coefficient, C_b, was defined as:

$$C_b=\frac{3\mu}{h\rho\sqrt{U_x{}^2+U_y{}^2}}+\frac{m^2g}{h^{\frac{1}{3}}}=\frac{3}{Re_h}+\frac{m^2g}{h^{\frac{1}{3}}} \tag{2.6}$$

where μ, water dynamic viscosity and m, Manning friction coefficient. In Eq. (2.9) the first term dominates under laminar and transitional flow ($Re_h \leq 500$), whereas the second one becomes significant for larger Reynolds numbers ($Re_h \geq 1250$).

Vegetation drag was modeled using the following expressions for the drag exerted by the stems (Kadlec and Wallace, 2008):

$$\tau_{vx} = \frac{1}{2}\rho C_{vD} n_v d l U_x \sqrt{U_x{}^2 + U_y{}^2} \tag{2.7}$$

$$\tau_{vy} = \frac{1}{2}\rho C_{vD} n_v d l U_y \sqrt{U_x{}^2 + U_y{}^2} \tag{2.8}$$

where: C_{vD}, vegetation-drag coefficient (dimensionless); n_v, number of vegetation stems per unit area; d, cylinder diameter of vegetation; l, submerged stem length (here taken as equal to water depth h). The coefficient C_{vD} was expressed as:

$$C_{vD} = \frac{10\mu}{\rho d \sqrt{U_x{}^2 + U_y{}^2}} + 1 = \frac{10}{Re_d} + 1 = \frac{10}{Re_h}\frac{h}{d} + 1 \tag{2.9}$$

where $Re_d = Ud/\nu$ is the stem Reynolds number.

2.2.3 Solute transport model

The transport of suspended sediment was simulated using the 2D depth-averaged advection-dispersion equation with a first-order source/sink term:

$$\frac{\partial(hC)}{\partial t} + \frac{\partial(hU_x C)}{\partial x} + \frac{\partial(hU_y C)}{\partial y} = \frac{\partial}{\partial x}\left(hE_{xx}\frac{\partial C}{\partial x} + hE_{xy}\frac{\partial C}{\partial y}\right) + \frac{\partial}{\partial y}\left(hE_{yx}\frac{\partial C}{\partial x} + hE_{yy}\frac{\partial C}{\partial y}\right) - KC \tag{2.10}$$

where: C, depth-averaged sediment concentration and KC, source term representing sediment settling and resuspension (see section 2.2.4). The coefficients E_{ij} accounted for both turbulent diffusion and shear dispersion due to vertical velocity gradients (Arega and Sanders 2004), and were expressed in terms of the transverse diffusivity (k_t) and longitudinal dispersion coefficient (k_l):

$$E_{xx} = k_l + (k_l - k_t)\frac{U_x{}^2}{U_x{}^2 + U_y{}^2} \tag{2.11}$$

$$E_{xy} = E_{yx} = (k_l - k_t)\frac{U_x U_y}{U_x{}^2 + U_y{}^2} \tag{2.12}$$

$$E_{yy} = k_t + (k_l - k_t)\frac{{U_y}^2}{{U_x}^2 + {U_y}^2} \tag{2.13}$$

Transverse diffusion for flow through emergent vegetation was expressed as a combination of mechanical and turbulent diffusion as proposed by Nepf (1999):

$$\frac{k_t}{U_x d} = \alpha_h (C_{vD} ad)^{\frac{1}{3}} + \frac{\beta^2}{2} ad \tag{2.14}$$

where: α_h and β are o(1) factors; a, plant area projected on a plane perpendicular to the flow direction per unit volume (m^{-1}) and $a = n_v d$ for cilindric stems. Based on experimental data, Nepf (1999) suggested $\alpha_h = 0.81$ and $\beta = 1$.

The longitudinal dispersion k_l included the effects of stem-scale longitudinal dispersion and the dispersion induced by vertical velocity gradients. The non-dimensional form of the coefficient k_l was written as a combination of the stem-scale and the depth-scale dispersion process as (Lightbody and Nepf, 2006):

$$\frac{k_l}{U_x \mathrm{d}} = \frac{1}{2}(C_{vD})^{\frac{3}{2}} + \frac{U_x h}{D_z} \Gamma \tag{2.15}$$

where $D_z = \alpha_z (C_{vD} ad)^{\frac{1}{3}} Ud$ was the vertical turbulent diffusion coefficient; $\alpha_z = 0.1$, and Γ, non-dimensional velocity shape factor. Typically the first term in Eq. (2.15) is smaller than the second term. For the range of stem Reynolds numbers investigated in this study it was reasonable to consider only the first term of Eq. (2.14) and the second term of Eq. (2.15).

2.2.4 Sediment transport processes

Sediment transport was represented in the model considering the processes of deposition and resuspension that affected the concentration C of suspended particles. These were represented by an effective deposition rate $K(x,y)$ in Eq. (2.10) expressed as:

$$K = k_s - k_r \tag{2.16}$$

where k_s, settling rate, and k_r, resuspension rate. The settling rate k_s depended on the fall velocity w_s and water depth h:

$$\mathrm{k_s} = \frac{\mathrm{w_s}}{\mathrm{h}} \tag{2.17}$$

Since variations in water depth within the wetland were negligible in this study, k_s was taken as constant for a given class size.

The fall velocity w_s was expressed using the Newton-Stokes formula. A particle suspended in a still fluid is subjected to the opposite forces of submerged weight W and viscous drag R_D:

$$W = (\rho_s - \rho_f) g V_p \tag{2.18}$$

$$R_D = C_D \frac{\rho_f w_s^2 A_p}{2} \tag{2.19}$$

where ρ_s and ρ_f, sediment and fluid density; V_p, particle volume; C_D, drag coefficient; A_p, projected particle area perpendicular to the direction of motion. The terminal particle settling velocity was found by imposing the equilibrium of the forces:

$$w_s = \sqrt{\frac{2 g V_p (\rho_s - \rho_f)}{C_D \rho_f A_p}} \tag{2.20}$$

For a spherical particle of diameter *D*, Eq. (2.20) becomes (Newton's Law):

$$w_s = \sqrt{\frac{4}{3} \frac{g(\rho_s - \rho_f) D}{C_D \rho_f}} \tag{2.21}$$

The drag coefficient C_D was function of the particle Reynold number, $Re_p = \frac{w_s D}{\nu}$. For spherical particles:

$$C_D = \frac{24}{Re_p} + \frac{3}{\sqrt{Re_p}} + 0.34 \tag{2.22}$$

The last two terms on the right-hand side of Eq. (2.22) can be neglected if $\mathrm{Re_p} < 1$, and Eq. (2.21) was expressed as (Stoke's law):

$$w_s = \frac{1}{18} \frac{g(\rho_s - \rho_f) D^2}{\mu_f} \tag{2.23}$$

If $\mathrm{Re_p} > 1$, the value of w_s obtained from Eq. (2.21) was used as a first approximation of an iterative procedure to determine C_D from Eq. (2.22) and w_s from Eq. (2.23).

As a first conceptual approximation, resuspension was modelled as a threshold process dependent on the Rouse number r,

$$r = \frac{w_s}{k u^*} \tag{2.24}$$

where: k, von Karman coefficient (k = 0.4); u^*, bed shear velocity. In general, $r > 2.5$ corresponds to a condition of very little to no suspended sediments. For $2.5 < r < 1.8$ a partial suspension takes place. For $r < 1.8$ there is full suspension. The largest size of suspended material was determined from the condition r = 2.5, which leaded to:

$$w_s = u^* \tag{2.25}$$

This condition was used in the model as a threshold for determining whether a given grain size would be in suspension or not. This provided a threshold condition in terms of the

bed shear stress: if $u^* < u^*_{th}$, there was no resuspension of sediments and the resuspension rate was equal to zero. If $u^* \geq u^*_{th}$, it was assumed that $k_r = k_s$. This condition applied locally as a function of the shear velocity:

$$u^* = \sqrt{\frac{\tau_b}{\rho}} \tag{2.26}$$

where the bed shear stress $\tau_b = \sqrt{\tau_{bx}^2 + \tau_{by}^2}$ was calculated from Eqs. (2.4) and (2.5). The effective settling rate was therefore:

$$K = k_s - k_r = \begin{cases} k_s & if\ u^* < u^*_{th} \\ 0 & if\ u^* \geq u^*_{th} \end{cases} \tag{2.27}$$

When the bed shear velocity exceeded the threshold shear velocity, non-cohesive sediments were resuspended and, according to the assumption above, K = 0. When the bed shear velocity became lower than the threshold, suspended sediments were deposited with a settling rate $K = k_s$.

2.3 Model application

Simulations were performed for a rectangular wetland of width B = 50 m, length L = 200 m and flat topography with zero bed slope. The wetland inlet and outlet were positioned symmetrically around the wetland central axis and were both 10 m in width. The boundary conditions were given by the inflow at the inlet, $Q_{in} = 0.0083$ m^3 s^{-1}, and the water depth at the outlet, H=0.5 m. Bottom resistance was represented by a uniform value of the Manning's roughness coefficient, M = 0.02 m$^{-1/3}$ s (Musner et al., 2014), whereas a no-slip condition was applied at the walls of the computational domain. The vegetation shear stresses were determined by Eqs. (2.7) and (2.8) assuming a stem diameter d =10 mm, which is typical of many constructed FWS wetland (Serra et al., 2004). Simulations were performed for 4 different values of uniform vegetation densities n_v = 1, 10, 100, 1000 stems m^{-2}.

The transport equation (2.10) was solved for a constant concentration C_{in} at the inlet, an open boundary condition at the outlet, and the no-flux condition on the remaining part of the flow boundary. The sediment particles were considered uniform, spherical, with no mutual interaction. Fall velocity was prescribed as an input parameter. Table 2.1 shows the grain sizes considered in the simulations and their fall velocity, determined as described in Section 2.2.3 and assuming a particle density value of $\rho_s = 2600$ kg m^{-3}. Although the diameters chosen belong to the category of cohesive sediments, they were treated as non-cohesive under the assumption of instant resuspension.

The outlet concentration of the suspended solid was used to estimate the removal efficiency of the wetland for the different grain sizes and vegetation densities. The removal efficiency E was taken as the ratio between the outlet concentration C_{out} and the inlet concentration C_{in}:

$$E = \frac{C_{out}}{C_{in}} \tag{2.28}$$

Table 2.1 Diameter D and fall velocity w_s of sediment particles used in the simulations.

D [$\times 10^{-6}$ m]	1	2	3	4	5	6	7	8	9	10
w_s [$\times 10^{-6}$m/s]	0.9	3.5	7.8	13.9	21.8	31.4	42.7	55.8	70.6	87.1

2.4 Results and discussion

The efficiency values obtained from the numerical simulations are presented in Table 2.2 and Figure 2.1. The curves showed a common behavior: efficiency increases slowly with sediment size for very small particles, whereas the slope increases for higher grain sizes until the condition of complete removal is achieved. This behavior is similar for all the vegetation densities. For the highest density, the difference between the first and the final part of the graph is more evident: a slight increase in efficiency up to D = 6 μm followed by a significant increase in the slope of the curve. Figure 2.2 shows the steady-state concentration distribution obtained for 2 different diameters. Up to D = 6 μm the concentration of suspended sediment is significantly different from zero over most of the wetland and the average concentration at the outlet is close to the inlet concentration. Conversely, for D = 8 μm most of the sediment is detained inside the wetland.

Table 2.2 Removal efficiency obtained from the numerical simulations for different grain diameters, D, and vegetation densities, nv.

D [$\times 10^{-3}$]	1	2	3	4	5	6	7	8	9	10
w_s [$\times 10^{-6}$ m s^{-1}]	0.9	3.5	7.8	13.9	21.8	31.4	42.7	55.8	70.6	87.1
E[%], n_v 1 stems m^{-2}	1.3	1.3	2.4	6.1	12.6	22.9	36.5	55.9	100.0	100.0
E [%], n_v 10 stems m^{-2}	1.5	1.5	1.7	3.3	7.9	16.4	29.9	67.9	100.0	100.0
E [%], n_v 100 stems m^{-2}	1.2	1.2	1.3	2.4	4.5	9.8	22.6	100.0	100.0	100.0
E [%], n_v 1000 stems m^{-2}	0.9	0.9	1.0	1.4	3.2	6.2	17.4	100.0	100.0	100.0

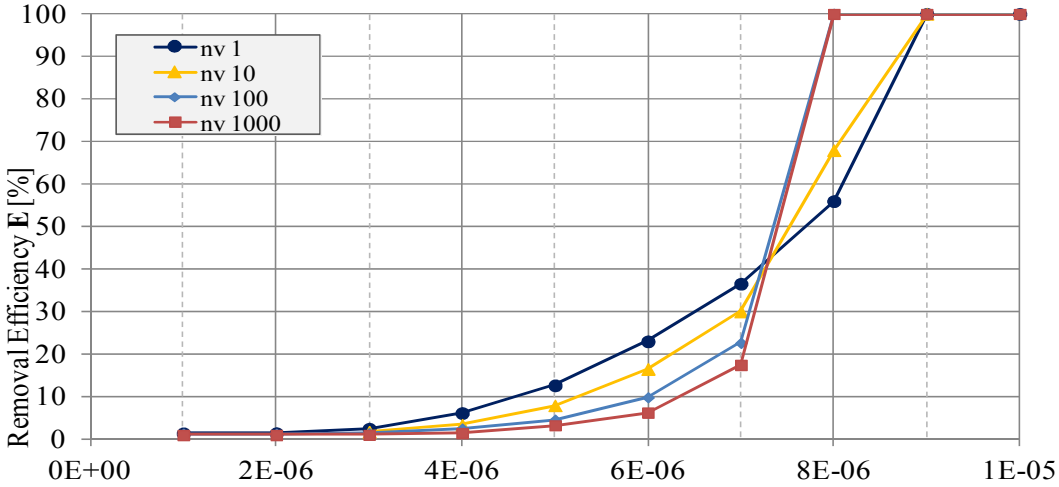

Figure 2.1 Calculated removal efficiency, E, versus grain diameter, D, and vegetation density, n_v

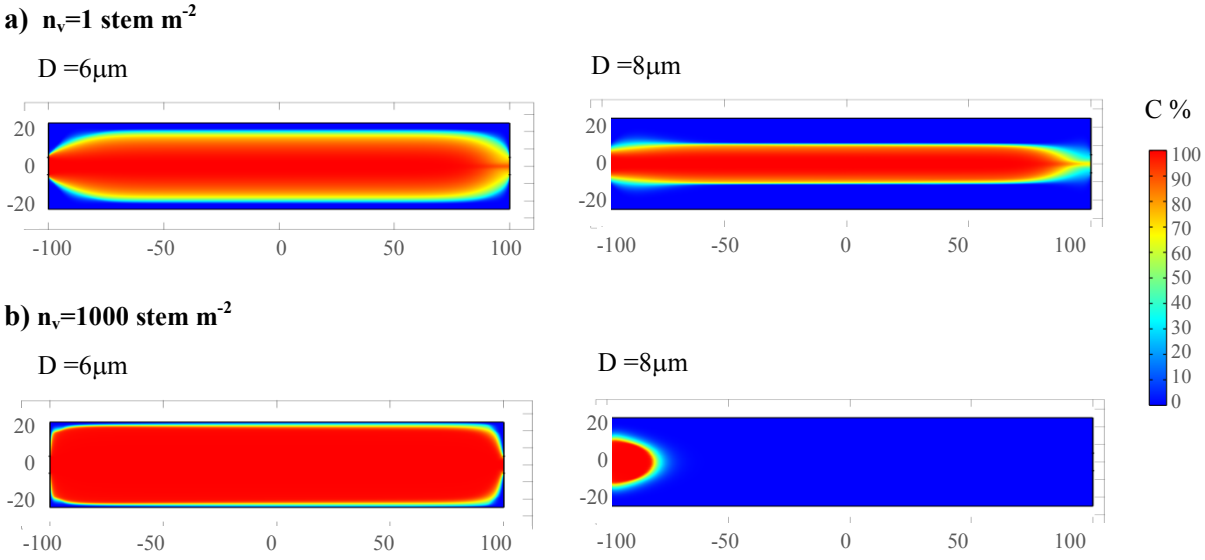

Figure 2.2 Steady-state concentration distributions of suspended sediment in the wetland, for two different grain diameters, $D = 6$ µm (left side) and $D = 8$ µm (right side) and two vegetation densities (n_v=1 stems m-2 and n_v=1000 stems m-^{2}, respectively in row a) and row b)).

The efficiency curves in Figure 2.1 exhibit an unexpected behavior: for the same inflow discharge, efficiency decreases as vegetation density increases. In the final part of the curves, just before the condition of total removal is achieved (E=100%), this trend is reversed: wetlands with higher vegetation density have higher efficiency and achieve total removal of suspended sediment for finer grain sizes. This behaviour can be understood by looking at the spatial distribution of the shear velocity (examples in Figure 2.3). Although the shear velocity (as well as the flow velocity) decreases as vegetation density increases, in the case where n_v=1 stems m^{-2}, the flow occurs mostly in a narrow central strip of the domain. Thus, for

lower vegetation densities, the flow is more channelized, and the shear velocity averaged over the entire wetland, u^*_{mean}, is lower, whereas the shear velocity at the center of the wetland $u^*(0,0)$ is higher (see Table 2.3). As the vegetation density increases, the mean shear velocity u^*_{mean} increases because the flow distribution becomes more uniform, whereas the value at the middle point $u^*(0,0)$ decreases. In the simulations, the velocity distribution is symmetrical and the velocity in proximity of the middle point represents the minimum velocity along the central streamline. If sediments can pass the central section at $x = 0$, they are more likely to reach the outlet. Hence, for higher vegetation densities, corresponding to smaller values of $u^*(0,0)$, the condition of complete removal is achieved for smaller grain diameters (see E=100% in Figure 2.4). The shear velocity u^*_{mean} can explain the general trend of efficiency: for finer grain sizes, efficiency is lower in more densely vegetated wetlands because the velocity distribution is more uniform (hence u^*_{mean} is higher). Figure 2.5 shows the behavior of the efficiency and the mean shear velocity versus vegetation density for a few grain diameters: removal efficiency decreases with increasing mean shear velocity, which increases with increasing vegetation density.

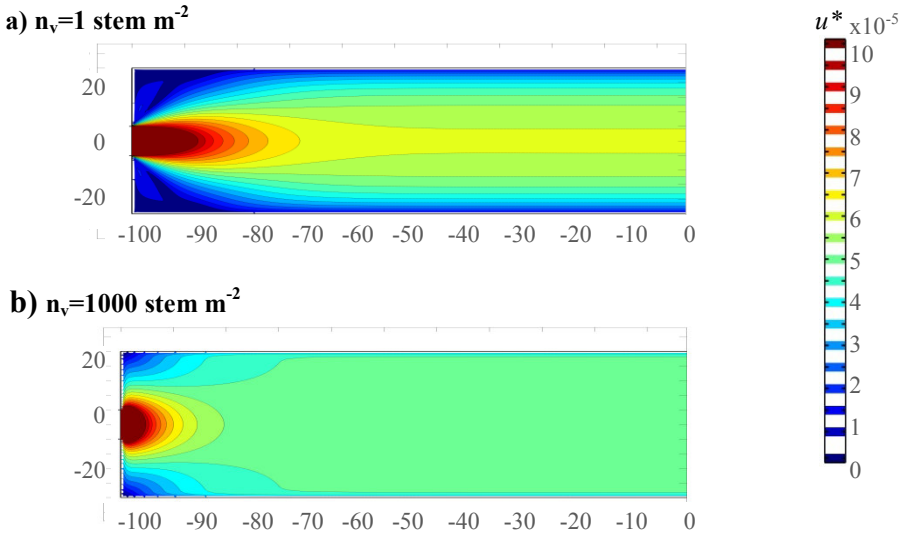

Figure 2.3 Spatial distribution of shear velocity (in the first half of the wetland domain) for two different vegetation densities: (a) 1 stems m^{-2} and (b) 1000 stems m^{-2}.

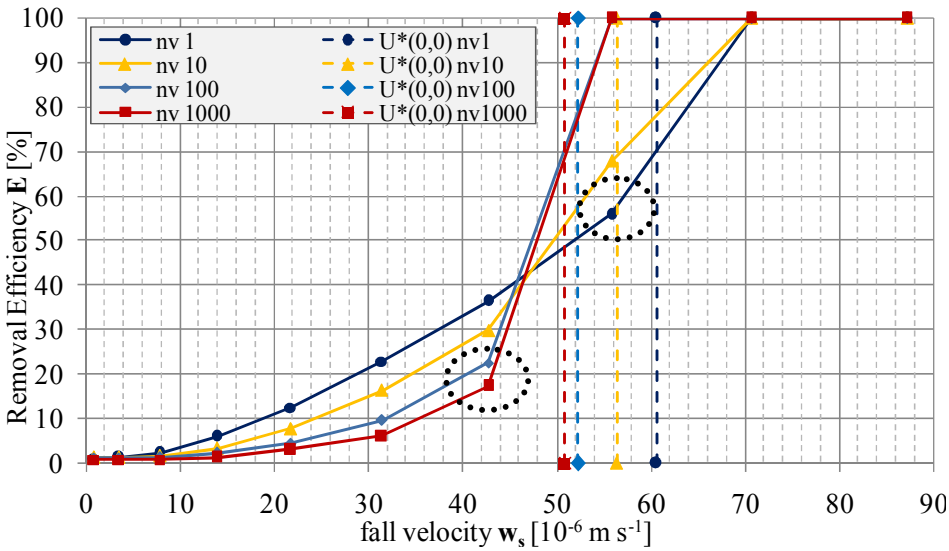

Figure 2.4 Comparison between removal efficiency E and shear velocity in the middle of the wetland, u*(0,0), for different vegetation densities n_v. The dotted circles highlight the largest sediment size, among those considered, for which there is a significant sediment concentration at the outlet. These have threshold shear velocity (equal to their fall velocity) just lower than u*(0,0). For higher n_v, u*(0,0) decreases, and total removal is achieved for lower diameters.

Table 2.3 Shear velocity for different vegetation densities, nv. The values reported in the table are the average shear velocity u^*_{mean} and the shear velocity in the center of the wetland, u*(0,0).

n_v [stems/m^2]	1	10	100	1000
u^*_{mean} [$\times 10^{-6}$ m/s]	48.9	49.6	50.5	50.8
$u^*(0,0)$ [$\times 10^{-6}$ m/s]	60.6	56.4	52.2	50.8

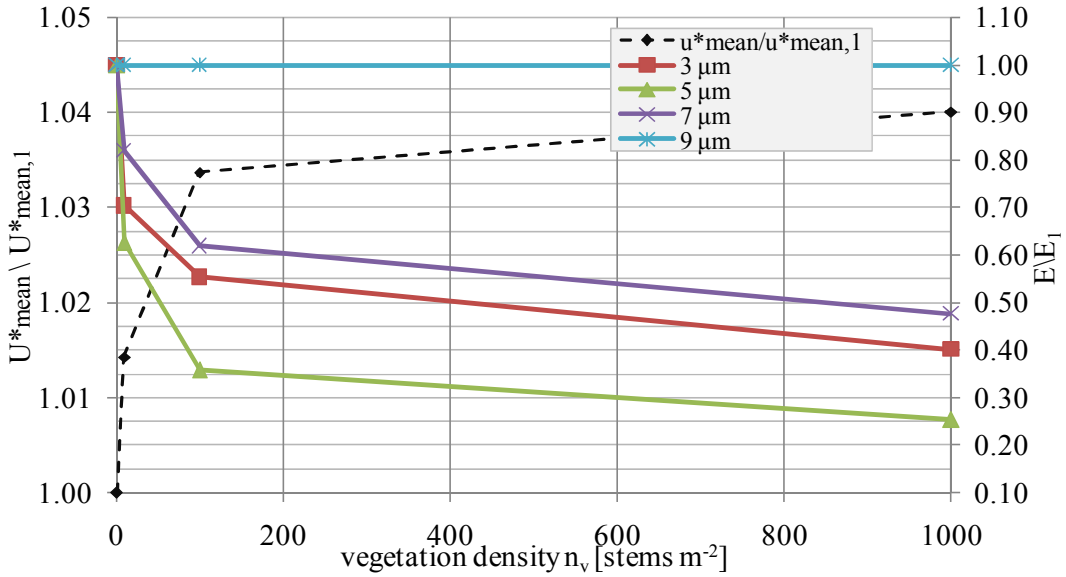

Figure 2.5 Comparison between removal efficiency for some diameters and average shear velocity u^*_{mean} as function of n_v. Values are normalized by the average shear velocity, $u^*_{mean,1}$, and removal efficiency, E_1, obtained for n_v = 1 stems m^{-2}.

The results show that the presence of vegetation in a wetland affects its capacity to remove suspended sediment particles. Under a few simplifying assumptions on the settling/resuspension rate, it has been shown that the presence of vegetation may cause a greater amount of fine sediment particles to remain in suspension as compared to the case of a less densely vegetated wetland. In contrast, more densely vegetated wetlands achieve complete settling for smaller particle sizes.

2.5 Conclusions

This study has analyzed the removal of suspended sediment in a vegetated wetland. The analysis is based on a simplified model in which settling and resuspension is represented by a first-order source/sink term in the advection-dispersion equation. This term depends on the definition of a settling/resuspension rate, K, which is expressed as a function of sediment diameter and vegetation density.

The removal efficiency E as a function of grain size exhibits an unexpected behavior for different vegetation densities. For very fine particles, E decreases as vegetation density increases. However, in the final part of the efficiency curve, where E approaches 100%, this trend is reversed: E is higher for higher vegetation densities and E = 100% for finer grain sizes. This can be explained by the spatial distribution of velocity (and shear velocity) in wetlands with different vegetation densities. More densely vegetated wetlands are characterized by more uniform velocity distributions, resulting in a greater value of the average shear velocity. A larger amount of sediment remains in suspension and can reach the outlet. On the other hand, since the maximum velocity is smaller, total removal (by settling) is achieved for smaller grain sizes.

The proposed model is intended as a possible conceptual model to study sediment transport processes in constructed wetlands. In particular, the formulation of the settling and the resuspension rate is based on a few simplifying assumptions that will need to be tested and further refined in a future study. More detailed numerical simulations and improved theoretical models of sediment transport in wetlands will underpin the development of improved criteria for wetland design.

2.6 Bibliography

Arega F, Sanders BF (2004). Dispersion model for tidal wetlands. J. Hydraul. Eng.130 (8), 739–754.

Gargallo S, Martín M, Oliver N, Hernández-Crespo C (2016). Sedimentation and resuspension modelling in free water surface constructed wetlands. Ecol Eng 98:318-329. doi: 10.1016/j.ecoleng.2016.09.014

Jenkins G a., Greenway M (2005). The hydraulic efficiency of fringing versus banded vegetation in constructed wetlands. Ecol Eng 25:61-72. doi: 10.1016/j.ecoleng.2005.03.001

Kadlec R, Knight R (1996). Treatment Wetlands. CRC Press, Boca raton, FL

Kadlec R, Wallace S (2008). Treatment Wetlands, 2nd edition. CRC Press, Boca raton, FL

Langergraber G (2001). Development of a simulation tool for subsurface flow constructed wetlands. Wiener Mitteilungen 196, Vienna, Austria (Ph. D. thesis)

Lightbody AF, Nepf HM (2006). Prediction of velocity profiles and longitudinal dispersion in salt marsh vegetation. Limnol Oceanogr 51:218–228. doi: 10.4319/lo.2006.51.1.0218

Marion A, Nikora V, Puijalon S, Bouma T, Koll K, Ballio F, Tait S, Zaramella M, Sukhodolov A, Hare O, Wharton G, Aberle J, Tregnaghi M, Davies P, Parker G, Statzner B (2014). Aquatic interfaces : a hydrodynamic and ecological perspective. J Hydraul Res 52:744–758. doi: 10.1080/00221686.2014.968887

Musner T, Bottacin-Busolin a., Zaramella M, Marion A (2014). A contaminant transport model for wetlands accounting for distinct residence time bimodality. J Hydrol 515:237–246. doi: 10.1016/j.jhydrol.2014.04.043

Nepf HM (1999). Drag, turbulence, and diffusion in flow through emergent vegetation. Water Resour Res 35:479–489. doi: 10.1029/1998WR900069

Sabokrouhiyeh N, Bottacin-Busolin A, Nepf H, Marion A (2016). Effects of vegetation density and wetland aspect ratio variation on hydraulic efficiency of wetlands. Hydrodynamic and Mass Transport at Freshwater Aquatic Interfaces, 101-113

Savickis J, Bottacin-Busolin A, Zaramella M, Sabokrouhiyeh N, Marion A,(2016). Effect of a meandering channel on wetland performance. J Hydrol 535:204–210. doi: 10.1016/j.jhydrol.2016.01.082

Serra T, Fernando HJS, Rodríguez R V (2004). Effects of emergent vegetation on lateral diffusion in wetlands. Water Res 38:139–47. doi: 10.1016/j.watres.2003.09.009

Somes NLG, Bishop WA, Wong THF (1999) Numerical simulation of wetland hydrodynamics. Environ Int 25:773–779. doi: 10.1016/S0160-4120(99)00058-6

Stone K, Poach M, Hunt P, Reddy G (2004). Marsh-pond-marsh constructed wetland design analysis for swine lagoon waste water treatment. Ecol Eng 23:127–133

Wu W (2007) Computational River Dynamics. CRC Press

Chapter 3

3 Modelling bed heterogeneity in wetlands

3.1 Introduction

Researchers have verified that the treatment efficiency of a reactor could be established using the hydraulic residence time as main parameter (Kadlec and Knight, 1996; Martinez and Wise, 2003). The best functioning condition for a detention pond or constructed wetland is when the flow approaches the "plug flow", in which all of the water entering the system remains for the nominal residence time, T_n, equal to the ratio between wetland volume V and inflow Q. But the theoretical mean residence time is not achieved in most of the wetlands because of incomplete use of the wetland volume. Non-uniform flow conditions are due to the formation of both stagnant or reduced mixing areas and faster velocities paths, which results in short-circuiting decreasing the residence time in wetlands (much of the water exits in less than T_n) and thus the time available for reactions to take place. Many of the biochemical, filtering, and settling processes that reduce pollutant concentration are first-order reactions, for which the highest rates of reduction ($\partial C/\partial t$) occur at early time. Therefore, concentration reduction is lower in water parcels leaving at times shorter than the design time, i.e. short-circuiting, than in parcels leaving at the design time.

If the hydrodynamics of a wetland, and more specifically the reduction of short-circuiting, could be linked with its design parameters, more informed decisions regarding constructed wetland design and natural wetland modification could be made in order to build

more efficient and less expensive water treatment facilities. As reported in section 1.1, several studies focused on modelling vegetation distribution and geometrical features in wetlands (Thackston et al., 1987; Arega and Sanders, 2004; Jenkins and Greenway, 2005; Abbas et al., 2006; Lightbody, 2007). However, the use of these models did not display a clear relationship between RTDs, vegetation density, vegetation distribution, bathymetric heterogeneity. The model developed by Musner et al. (2014), based on COMSOL Multiphysics, was applied for quantify the effect on removal efficiency of different wetland parameters: vegetation patterns in a channelized wetland, sinuosity of the channel in a channelized wetland, shape, position of inlet and oulet, width-to-length ratio, vegetation heterogeneity (Musner et al, 2004; Savickis et al., 2016; Sabokrouhiyeh et al. 2016, 2017). The simulated velocity field demonstrated that these parameters could significantly impact the size of dead zone areas, which was also reflected in the residence time distribution (RTD). In those studies, relationships between RTD, removal efficiency, and bottom topography had not been directly addressed. Some studies have suggested to deflect inflow and improve the circulation pattern within treatment wetlands and ponds by the insertion of islands (German and Kant, 1998). Numerical simulations by Persson et al. (1999, 2000) showed that the configuration with an island at the inlet reduced short-circuiting, compared to a basin with no island or with berms. Contrasting results from Adamsson et al. (2002) and Khan et al. (2011) suggested that the potential impact of a deflector island was sensitive to the size of the island, the position within the basin and the basin geometry. A physical modelling study by Guzman et al. (2018) investigated several configurations of berms, islands, clusters inside a basin through tracer experiments. They evaluated short-circuiting, ecological diversity, construction cost. Regarding hydraulic performance alone, specifically the elimination of short-circuiting, they found that a cluster of islands near the inlet provided the greatest improvement in the short-circuiting and that there were several options for high performing configurations with different amounts of topography. A numerical study by Conn and Fiedler (2006) focused on quantitatively estimating the effects of bottom topography on hydraulic retention time (HDT). They simulated a rectangular wetlands with different topographic features (flat bottom, emerging islands, meandering baffled wetlands,..) for four inflows hydrographs having different peak flow rates. They evaluated the performance of each simulation as increase of HDT with respect to the flat bottom simulation, founding that baffles increased the flow path length through the wetland and thus the detention time. Moreover, because overtopping of baffles reduced the flow path length, using baffles with multiple scale of topography leaded to a higher efficiency of the wetland under variable inflow conditions.

Therefore, while some promising results have been reported in previous researches, additional studies are needed to better relate removal efficiency to bathymetric features of a wetland. For example, by numerically modelling a large number of bottom topographies, by identifying main parameters for describing the bed forms, by varying one parameter a time, and by evaluating the removal efficiency using suitable indexes (not only retention time).

3.2 The numerical model system

For including in the numerical study key parameters (bathymetric heterogeneity, bathymetric dataset resolution, not homogeneous roughness) affecting hydrodynamics and removal efficiency in wetlands, a new 2D numerical model was implemented because the model presented in Chapter 2 wasn't suitable for this purpose. The new hydrodynamics model was based on an open source code, Telemac 2D, developed by the National Hydraulics and Environment Laboratory (Laboratoire National d'Hydraulique et Environnement - LNHE) of the Research and Development Directorate of the French Electricity Board (EDF-R&D), in collaboration with other research institutes. Telemac could be applied to heterogeneous fields of bathymetry and/or roughness generated by specifically coded Matlab scripts. Matlab scripts were also developed in order to simulate the transport of a passive tracer with a depth-averaged solute transport model once the flow field (steady-state) was computed. After completion of each hydrodynamics-transport simulation, the analysis of results was performed through the estimation of the statistical moments of the probability density function of residence times. Hydraulic residence time distributions (RTDs) provide a measure of the variability of the retention time and represent a valuable tool for assessing the efficiency of contamination removal. The conceptual modelling flow is shown in Figure 3.1.

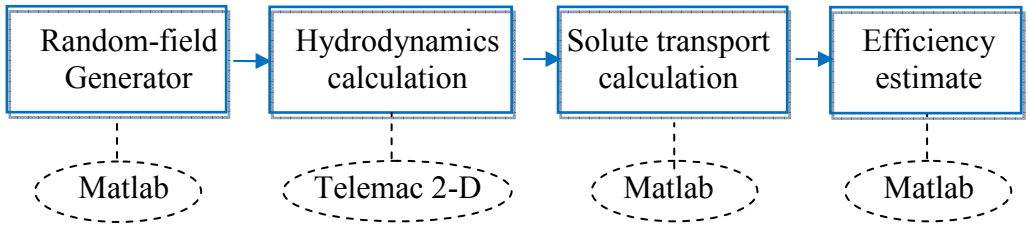

Figure 3.1 Conceptual working flow of the new modelling system

The new modelling system was initially tested with a simpler quasi 1-D domain, represented by a straight channel, before application to the more complex 2-D wetland domain. This system allowed studying statistically the bathymetric configurations, because the fundamental idea was to generate several random fields with the main geometric parameters unchanged: spatial resolutions d_x, d_y, longitudinal correlation length L_x, transverse

correlation length L_y, standard deviation of the bottom elevation σ_z. Running a simulation many times, while keeping the same parameters unchanged, means generating new fields, because of the random process, with the same geometric characteristics. This could permit to statistically analyze the relationship between each of the above parameters, the domain topography, and the removal efficiency by isolating each parameter and varying it, while maintaining all the other parameters constant. In order to assess the intrinsic variability of the studied model, each simulation should be performed at least 10-15 times.

As the first step in this study, the modelling investigation was performed by analyzing different topographies in order to have initial indications about which parameters could affect the removal efficiency. In the following sections, each part of the model is better described.

3.2.1 Random bathymetry generator

Matlab scripts were coded in order to create random fields (of bathymetry and/or bed roughness) with prescribed statistical parameters. The effect of each bathymetric distribution on the removal efficiency was then numerically evaluated by a coupled hydrodynamic and solute transport.

The algorithm allowed reproducing random fields characterized by different spatial probability density functions; here a simple Gaussian space probability density function was adopted. For the purpose of this work, it was chosen to make only the topography vary and fix a constant roughness for the entire wetland. The bathymetry was treated as a random variable characterized by some statistical parameters: mean bottom elevation $\bar{z} = 0$, elevation variance σ_z, longitudinal and transversal correlation lengths, L_x and L_y. By varying these parameters, bed forms with different features could be generated. The random bathymetries were created as a grid of points with a user-defined spatial resolution. The spatial resolution defined the distance between two points along the longitudinal and the transverse direction (d_x and d_y, respectively). It was assumed d_x=d_y=0.1 m, a dense resolution that allowed to properly describe the wetland bathymetries. It is possible to infer the relationship between each of the above parameters and the topography by isolating the parameter of interest and making it vary, while maintaining all the other parameters fixed. The standard deviation of the water depth constitutes the range of variability for the elevation of the channel bottom z. For small values of σ_z the bottom is quite flat; increasing σ_z the bottom becomes irregular and shows "pools" and bumps that can also emerge from water (compare Figure 3.2 a) and b), with σ_z=0.1 m and 0.2 m respectively). The longitudinal correlation length L_x influences the distribution of the lowest heights of the bottom in the longitudinal direction. The transverse

correlation length L_y influences the distribution of the wetland bottom in the transverse direction. When $L=L_x=L_y$, the topography is characterized by isotropic bed forms; by increasing L bed forms passes from small patches to large-scale patchiness (compare Figure 3.2 b) and c), with L=2 m and 10 m respectively). With $L_x<L_y$, the topography is characterized by anisotropic bed forms in the transversal direction (Figure 3.2 d); while bed forms in the longitudinal directions are obtained with $L_x>L_y$ (Figure 3.2 e).

In this way, random topographies were generated as (x, y, z) data points and then interpolated on the Telemac mesh for the flow calculations.

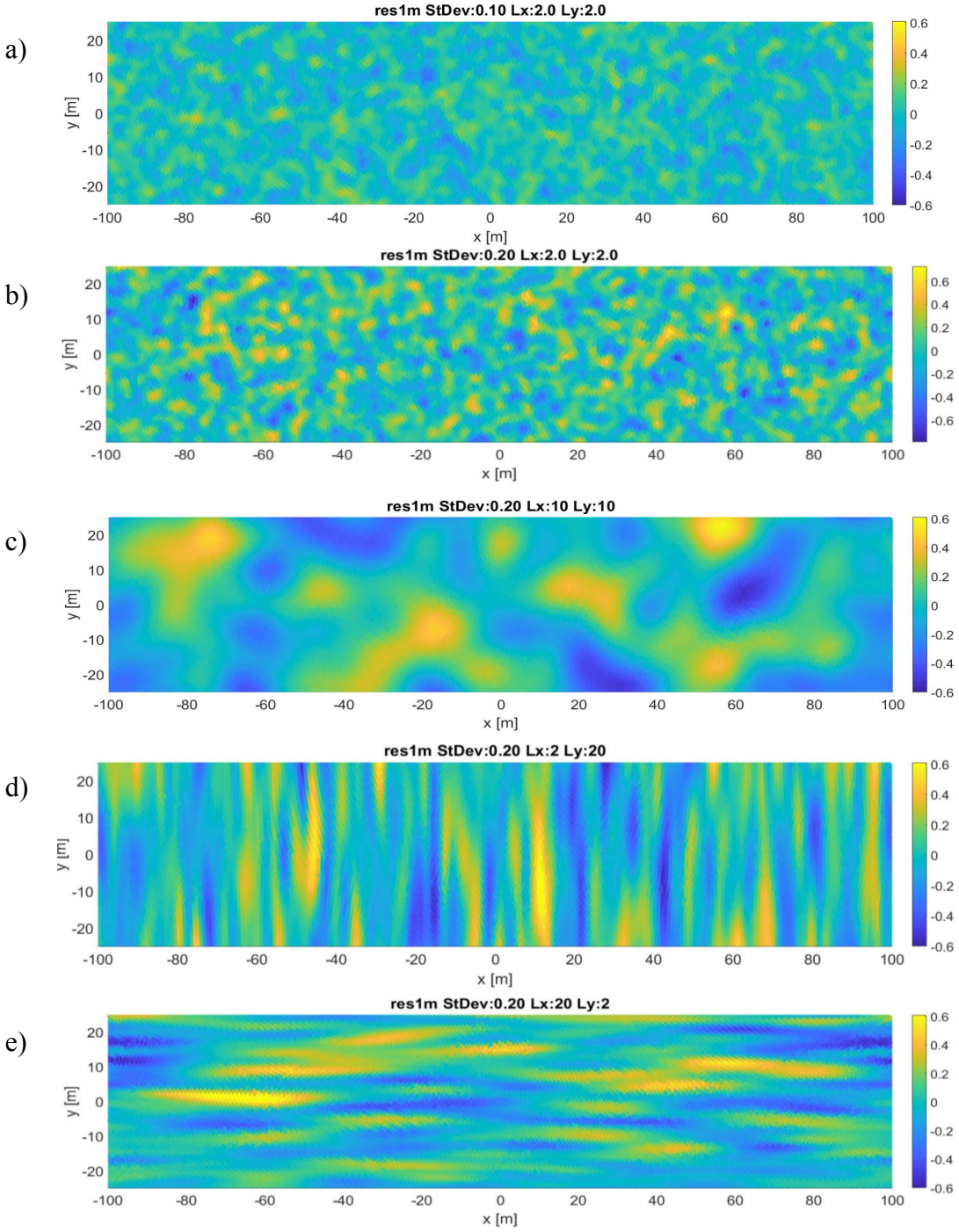

Figure 3.2 Randomly generated bathymetries with different statistical properties

3.2.2 Hydrodynamics modelling

Telemac-Mascaret is an open source and Telemac 2D is one of its modules that was initially developed by the National Hydraulics and Environment Laboratory (Laboratoire National d'Hydraulique et Environnement - LNHE) of the Research and Development Directorate of the French Electricity Board (EDF-R&D), in collaboration with other research institutes. Telemac 2D solves the shallow water De Saint Venant equations concerning depth-averaged free surface flow, expressed in Cartesian coordinates by the following continuity equation (3.1), momentum along x Eq. (3.2) and momentum along y Eq. (3.3) :

$$\frac{\partial h}{\partial t} + \vec{u} \cdot \nabla(h) + h\nabla\vec{u} = S_h \tag{3.1}$$

$$\frac{\partial u}{\partial t} + \vec{u} \cdot \nabla(U_x) = -g\frac{\partial \eta}{\partial x} + \frac{1}{h}\nabla(h\nu_t \nabla U_x) + S_x \tag{3.2}$$

$$\frac{\partial v}{\partial t} + \vec{u} \cdot \nabla(U_y) = -g\frac{\partial \eta}{\partial x} + \frac{1}{h}\nabla(h\nu_t \nabla U_y) + S_y \tag{3.3}$$

where:

- x, y (m) horizontal space coordinates
- h (m) water depth
- $\vec{u}$ (m/s) velocity vector
- U_x, U_y (m/s) velocity components along x and y direction
- η (m) free water surface elevation
- t (s) time
- g (m/s^2) gravity acceleration
- ν_t (m^2/s) momentum diffusion coefficient
- S_h (m/s) source or sink of fluid
- S_x and S_y source terms (bottom friction, Coriolis force, wind stress, etc.)

The unknowns are h, U_x, U_y. The equations are solved using the finite-element method. Many kind of input files could be used for properly describe the hydraulic problem, but the minimum mandatory input files required by the model are:

- the steering file, that is a text file containing the configuration of the computation and representing the control panel of the computation. It contains a number of keywords to which values are assigned,

- the geometry file, that is a binary file containing the mesh and information associated with the mesh (for example, values about bottom elevation and roughness)
- the boundary conditions file that contains the description of the type of each boundary.

The obtained output files are:

- The results file in which Telemac 2D stores information during the computation. It is normally in Serafin format. It carries information on the mesh geometry and on the names of the stored variables. It also contains the time for each time step and the values of the different variables for all mesh points. Moreover, it can be visualized with specific software such as BlueKenue.
- The listing printout that is the "log file" of the computation. If necessary, the user can get additional information in this file by activating the integer keyword DEBUGGER. This is useful in case of crash, to locate the guilty subroutine.

In our application, the geometry file was created by generating a triangular computational mesh using the graphical user interface BlueKenue that allows the user to set the mesh growth ratio. By interpolating on this mesh the random bathymetry dataset previously generated, bottom elevation values were associated with the vertices of the triangles. This could be done in the same way for the roughness, but in our study it was assumed a constant value of the Manning coefficient (i.e. 0.025 s $m^{-1/3}$).

In Telemac 2D, the initial depths of water is calculated by subtracting the bottom elevation z from the initial water surface elevation η. Therefore, in areas where the bottom elevation is higher than the initial free water surface elevation, the initial depth of water is zero. It is mandatory to specify the type of boundary conditions at each boundary point. A boundary can be rigid or liquid, the former concerns the hypothesis of impermeability while the latter supposes the existence of a fluid domain that does not belong to the domain of calculation but that can influence it. Boundary conditions concern the dependent variables of Telemac 2D or the values deduced from them: water depth h, the two components of velocity u and v and/or flow rate Q. In our study, they were an open boundary with prescribed flow rate at the inlet and an open boundary with prescribed both surface elevation and flow rate at the outlet. For the computation, a variable time steps option was chosen and a Courant number = 0.9. Especially when advection dominates dispersion, designing a model with a small Courant number (i.e. less than 1) will decrease oscillations and numerical dispersion and will improve accuracy. The time step defines the time separating two consecutive instants of the computation. Telemac 2D adjusts the calculation time step in order to satisfy the Courant number criterion. The duration of the simulations was chosen long enough to reach a steady-

state in the calculated flow field. This condition was verify for each resulting file by extracting time series at several points distributed in the wetland domain.
Modelling details about the studied wetland case are given in section 3.5.

3.2.3 Solute transport modelling

Solute transport of a passive tracer entering at the inlet was simulated with a depth-averaged solute transport model:

$$\frac{\partial(\mathrm{hC})}{\partial \mathrm{t}} + \frac{\partial(\mathrm{hU_xC})}{\partial \mathrm{x}} + \frac{\partial(\mathrm{hU_yC})}{\partial \mathrm{y}} = \frac{\partial}{\partial x}\left(hE_{xx}\frac{\partial C}{\partial x} + hE_{xy}\frac{\partial C}{\partial y}\right) + \frac{\partial}{\partial y}\left(hE_{yx}\frac{\partial C}{\partial x} + hE_{yy}\frac{\partial C}{\partial y}\right) \quad (3.4)$$

where:

- C (g m^{-3}) depth-averaged solute concentration
- h (m) water depth
- x, y (m) horizontal space coordinates
- U_x, U_y (m s^{-1}) velocity components along x and y direction
- t (s) time
- E_{xx}, E_{yy}, E_{xy}, E_{yx} (m^2 s^{-1}) Elder's dispersion tensor components

For the dispersion a zero equation model was considered: it assumes that the turbulent viscosity depends on known or easily calculable parameters. Thus, the Elder's dispersion tensor was calculated according to Arega and Sanders (2004) as follows:

$$E_{xx} = k_l + (k_l - k_t)\frac{\mathrm{U_x}^2}{\mathrm{U_x}^2 + \mathrm{U_y}^2} \quad (3.5)$$

$$E_{yy} = k_t + (k_l - k_t)\frac{\mathrm{U_x}^2}{\mathrm{U_x}^2 + \mathrm{U_y}^2} \quad (3.6)$$

$$E_{xy} = E_{yx} = (k_l - k_t)\frac{\mathrm{U_xU_y}}{\mathrm{U_x}^2 + \mathrm{U_y}^2} \quad (3.7)$$

The Elder model offers the possibility of specifying different mixing coefficient values along and across the current (k_l and k_t, respectively). The used formulae are:

$$k_l = a_l U^* h \quad (3.8)$$

$$k_t = a_t U^* h \quad (3.9)$$

where $U*$ (m s^{-1}), shear velocity; a_l and a_t, dimensionless dispersion coefficients equal to 6 and 0.6, respectively. Shear velocity was computed as:

$$U^* = \sqrt{\frac{\tau}{\rho_o}} = \sqrt{\frac{\sqrt{\tau_{bx}^2 + \tau_{by}^2}}{\rho_o}} = \sqrt{C_D}\bar{U} \quad (3.10)$$

This expression was derived by computing the contribution of bed friction to bed shear stresses adapting the 1D relationships proposed by Kadlec (1990) to a 2D velocity field:

$$\tau = \sqrt{\tau_{bx}^2 + \tau_{by}^2} \quad (3.11)$$

$$\tau_{bx} = \rho_o C_b u \bar{U} \quad (3.12)$$

$$\tau_{by} = \rho_o C_b v \bar{U} \quad (3.13)$$

$$\bar{U} = \sqrt{\mathrm{U_x}^2 + \mathrm{U_y}^2} \quad (3.14)$$

The bed Drag coefficient C_b combines both laminar and turbulent stresses and can be calculated according to Kadlec (1990):

$$C_b = \frac{3\nu}{h\bar{U}} + \frac{gm^2}{h^{1/3}} = \frac{3}{Re_h} + \frac{gm^2}{h^{1/3}} \quad (3.15)$$

where Re_h, the depth-Reynolds number; m (s $\mathrm{m}^{-1/3}$), Manning's coefficient. If $Re_\mathrm{h} < 500$ the first term on the right side of the equation prevails, if $Re_\mathrm{h} > 12500$ the second term on the right side of the equation prevails.

Matlab scripts were coded in order to simulate solute transport in the calculated flow domains, according to the Elder's model. Once the flow field was computed, the script in Matlab read the Telemac output file and interpolated the required values (h, $\mathrm{U_x}$, $\mathrm{U_y}$) on its own computational grid. In particular, a mesh grid size of 0.5 m was assigned for both the longitudinal and transversal direction. The Elder's dispersion tensor was computed and at each time step the transport of the solute was calculated according to Eq.(3.4). The advection-diffusion equation was solved by using a finite-volume scheme with shock-capturing for the advective part and an explicit method for the diffusive part. It was based on ClawPack libraries (Calhoun and LeVeque, 2000). A reference constant concentration C_{in}=1 of a conservative tracer was assumed entering the domain at the inlet and an open boundary condition at the outlet. The mass transport simulations were stopped when the standard deviation of the mass within the domain equals 10^{-6} or when the simulation time exceeds 10^7 s. From the concentration values in the time exiting the domain, $C_{out}(t)$, efficiency indexes were derived, as explained in next section.

3.3 Efficiency metrics

The concentration calculated at the wetland outlet versus time was used to define the residence time distribution (RTD). The removal efficiency of the wetland was derived from the calculation of the statistical moments of the RTD. A statistical description in terms of probability distributions was preferred for the analysis of the residence time because it can significantly vary due to different flow paths, velocity gradients and hydraulic short-circuits. Hydraulic residence time distributions (RTDs) provide a measure of the variability of the detention time and can be a valuable tool for assessing the efficiency of contaminant removal. Thackston et al. (1987) defined the concept of hydraulic efficiency as a function of the RTD's centroid position. Any reduction in wetland retention time (a shift of the centroid towards the origin), for example associated with the presence of stagnant areas, causes a decreased efficiency. When the observed retention time (t_m) is lower than the nominal retention time ($t_n=V/Q$), not all of the wetland volume (V) is utilized in the detention (and treatment) of the tracer. Dispersion levels within a wetland are quantified by the second moment (the variance) of the RTD. Under ideal plug-flow conditions, the RTD appears as a spike at the nominal retention time (t_n) with zero variance: all particles have the same retention time t_n.

From the outlet concentration in the time, $C_{out}(t)$, the residence time distribution function *F(t)* was derived as:

$$F(t) = \frac{Q_{out}(t)C_{out}(t)}{\int_0^\infty Q_{out}(t)C_{out}(t)dt} \quad (3.16)$$

where $Q_{out}(t)$, outlet tracer concentration; dt , time step.

The mean residence time, t_m, that is the average time the particles pass in the domain, was calculated as the first moment of RTD (Werner and Kadlec, 1996):

$$t_m = \mathrm{m}_1 = \int_0^\infty tF(t)dt \quad (3.17)$$

The variance (σ^2), i.e. the second moment, represents the variation in the times spent by individual parcels of water within the wetland and it was calculated as:

$$\sigma^2 = \mathrm{m}_2 = \int_0^\infty (t - t_m)^2 F(t)dt \quad (3.18)$$

The variance represents the degree of dispersion and is equal to zero for ideal plug flow. In presence of different flow paths, e.g. short circuiting flow paths, recirculation zones, or of high level of turbulent mixing, the variance is large.

From these statistical parameters, researchers defined several indexes for quantify wetland removal efficiency. A wetland can be modeled by a number of continuously stirred tank reactors (CSTRs). The number of CSTRs is a key factor in wetland modelling. The number of CSTRs in series can be determined according to Fogler (1992), from the inverse of the dimensionless variance (σ_θ):

$$N = (\sigma_\theta)^{-2} = (\frac{\sigma}{t_n})^{-2} \quad (3.19)$$

N could be considered as the degree of plug flow: the higher N, the more plug-flow-like the flow is and also less mixed, while few tanks suggest a high degree of mixing and flow path variance (high RTD variance). A dispersion efficiency index can be define as:

$$e_d = 1 - \frac{1}{\mathrm{N}} \quad (3.20)$$

The higher limit of e_d is 1, representing a better treatment, and it is obtained for an ideal plug-flow, with $\sigma^2 = 0$ and $\mathrm{N} = \infty$.

Thakston et al., (1987) introduced another index, the volumetric efficiency or dimensionless retention time:

$$e_v = \frac{t_m}{t_n} = \frac{V_{eff}}{V_{tot}} \quad (3.21)$$

It represents the effective volume V_{eff} of a wetland system of nominal volume V_{tot}. Low values e_d indicate the presence of dead zones and/or dispersion allowing the tracer to exiting the wetland in a time shorter than t_n.

Combining both effects of retention time (effective volume) and amount of dispersion, Persson et al. (1999) defined the hydraulic efficiency index, λ_p:

$$\lambda_p = \mathrm{e_v e_d} = \frac{t_m}{t_n}(1 - \frac{1}{N}) \quad (3.22)$$

The efficiency λ_p varies 0÷1, and it is high (better performance) when: i) the degree of mixing is low, which is preferable since all fluid elements reside around the nominal residence time and ii) the effective volume ratio is high, since this gives a longer detention time for a given volume. Persson classified the wetland removal performance as: poor for $\lambda_p < 0.5$, satisfactory when $0.5 < \lambda_p < 0.75$, good with $\lambda_p > 0.75$

In this study, these parameters were calculated and we examined their variation for different bathymetric configuration with respect to the flat topography.

3.4 Channel test case

For initially testing the modelling procedure, the model system was applied on a random-bathymetry channel (examples in Figure 3.3), that represented a simpler and faster test case than the wetland: a quasi 1-D domain, turbulent regime instead of the transitional/laminar flows characterizing the hydrodynamics in wetlands, less bathymetric statistical features to vary (in a straight long channel only L_x varies within a wide range), lower computational time required. The main features of the modeled channel were: width W=20 m, length L=2000 m, initial water surface elevation η_0=2.5 m, fixed inflow Q_{in}=49 m^3 s^{-1}, fixed surface elevation at the outlet η_{out}=2.5 m. Simulations were performed for different bathymetric configurations for testing the capability of the system to properly reproduce different flow fields and associated solute transport. In particular, three series of bathymetries with same bottom elevation variance σ_z, transversal correlation length L_y, and varying longitudinal correlation length L_x were tested:

- "series C1": σ_z=0.3 m, L_y=5 m, Lx=20,50,100,125,150,200
- "series C2": σ_z=0.1 m, L_y=5 m, Lx=20,50,100,125,150,200
- "series C3": σ_z=0.1 m, L_y=10 m, Lx=20,50,100,125,150,200

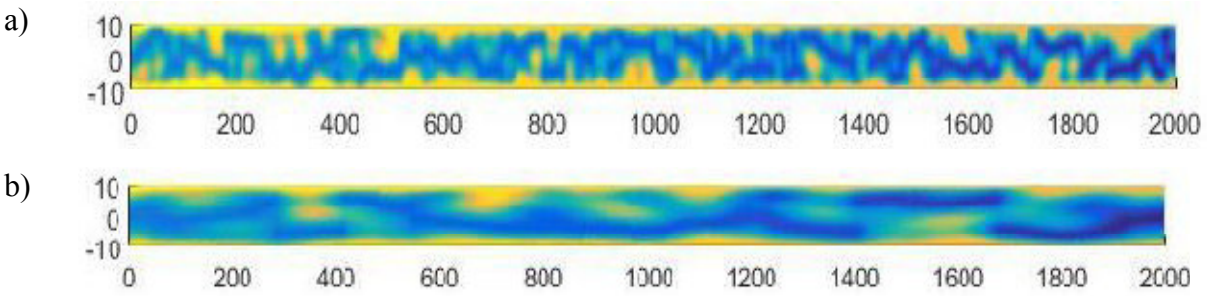

Figure 3.3 Two examples of random bathymetry for the channel, characterized by same standard deviation of bed elevation and same transversal correlation length (L_y=5), and different value of longitudinal correlation length L_x: a) L_x = 20 m, b) L_x = 100 m

From concentration curves C(t) calculated at several cross-sections along the channel length, RTDs were calculated and first and second moment plotted against the distance x from the inlet. For each simulation, the averaged velocity U_x and the dispersion coefficient D were inferred from these plots as:

$$U_x = \frac{1}{\frac{d\,m_1(x)}{dx}} \qquad (3.23)$$

$$D = \frac{1}{2}u^3 \frac{d\,m_2(x)}{dx} \qquad (3.24)$$

where: $\frac{d\,m_1(x)}{dx}$, slope of the first moment m_1 plot and $\frac{d\,m_2(x)}{dx}$, slope of the second moment m_2 plot (example in Figure 3.4).

These first simulations gave a set of preliminary data about the correlation between bathymetry and dispersion variability (Figure 3.5). Results showed that the dispersion coefficient slightly decreased with increasing correlation lengths, due to the channelization.

However, the channel case study wasn't further developed because it was specifically used for testing all the procedure steps of the new modelling system: (i) random bathymetry generation, (ii) Telemac hydrodynamics simulation, (iii) Matlab mass transport calculation, (iv) RTD estimate from $C_{out}(t)$.

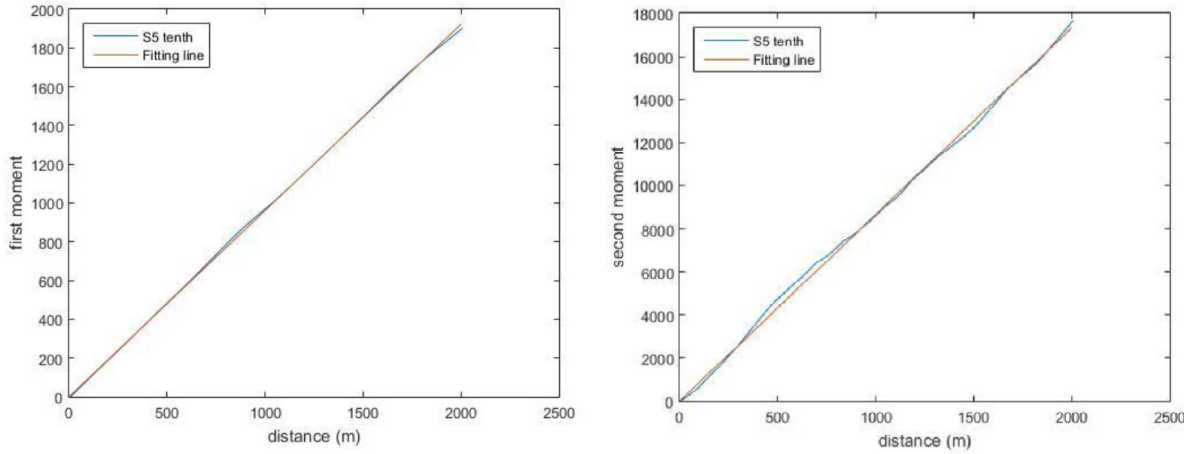

Figure 3.4. Example of first moment (on the left) and second moment (on the right) plots versus the distance x along the channel.

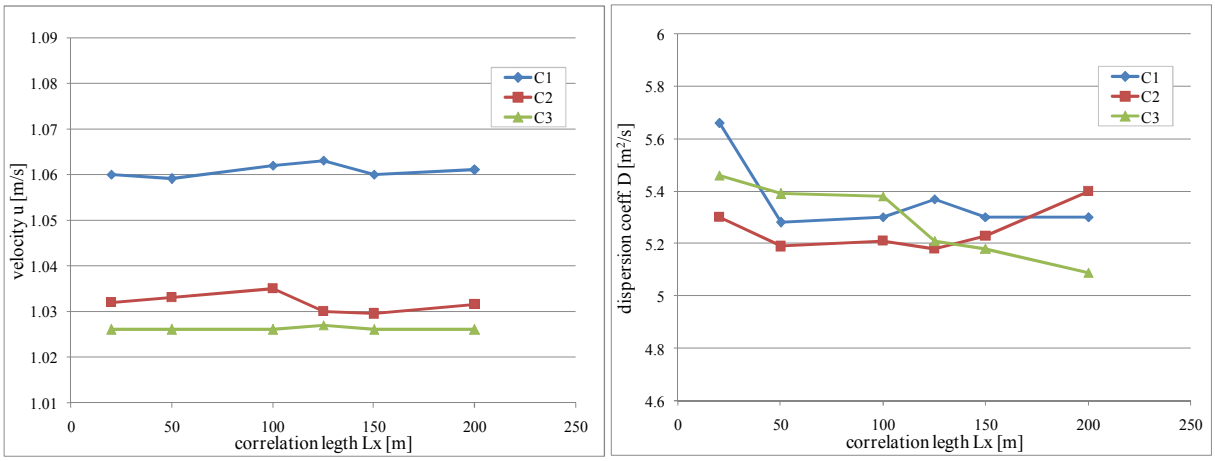

Figure 3.5 Velocity U_x (left) and dispersion coefficient D (right) versus the longitudinal correlation length L_x of the bed forms.

3.5 Wetland application

3.5.1 The modeled wetland

The subsequent step was the numerical study of constructed wetlands. The model was applied on a rectangular 2D domain, with very low flow velocities, which represent conditions for wetland devoted to water treatment. The generation of the random bathymetry was applied at the 2D domain, as explained in section 3.2.1 (example in Figure 3.6: isotropic case a), longitudinal bed forms b), transversal bed forms c)). Moreover, the model could reproduce not homogeneous roughness field, and could interpolate bathymetry data at different resolutions (Figure 3.6, resolution 1 m for c), 10 m for d), 20 m for e)). This last option could mimic real applications where the availability of bathymetric data is relatively poor and performing low time-consuming numerical simulations is required. However, in the present study, only bathymetry was varied.

The flow domain was given as a 200m-long-by-50m-wide rectangular wetland, with a total area A_w=10000 m^2. Inlet and outlet sections were 10 m wide and located symmetrically in the middle of the shorter sides of the domain. The triangular mesh generated for Telemac calculations was composed by about 13000 nodes and 25300 triangular elements. The triangles size was at maximum 1 m and a higher resolution mesh was defined at the inlet and outlet areas (Figure 3.7). The mesh was, for each new simulation, interpolated on the bathymetric data randomly generated with different statistical features of the bed forms. For the hydrodynamics calculation, the boundary conditions imposed were: constant flow rate $Q_{in} = 0.025\ m^3s^{-1}$ at the inlet, constant water surface elevation η_{out}=0.5 m and constant outflow $Q_{out} = 0.025\ m^3s^{-1}$ at the outlet. The remaining boundaries were treated as impermeable (no flux conditions) and no friction was applied to the lateral walls. An initial constant surface elevation $\eta = 0.5$ m was assigned on the whole domain, and the total volume was $V_{tot} = 5000\ m^3$.

After the completion of the Telemac simulation, when the flow reached a steady-state condition, Matlab scripts were applied for determining the solute transport. A conservative solute with a constant unitary concentration was injected at the inlet, an open boundary condition were given at the outlet, and the no-flux condition on the remaining part of the flow boundary. The average values of concentration were calculated at each time step at several cross-sections along the domain. From the concentration curve obtained at the final section, $C_{out}(t)$, RTDs statistical parameters and efficiency metrics were derive (see section 3.3).

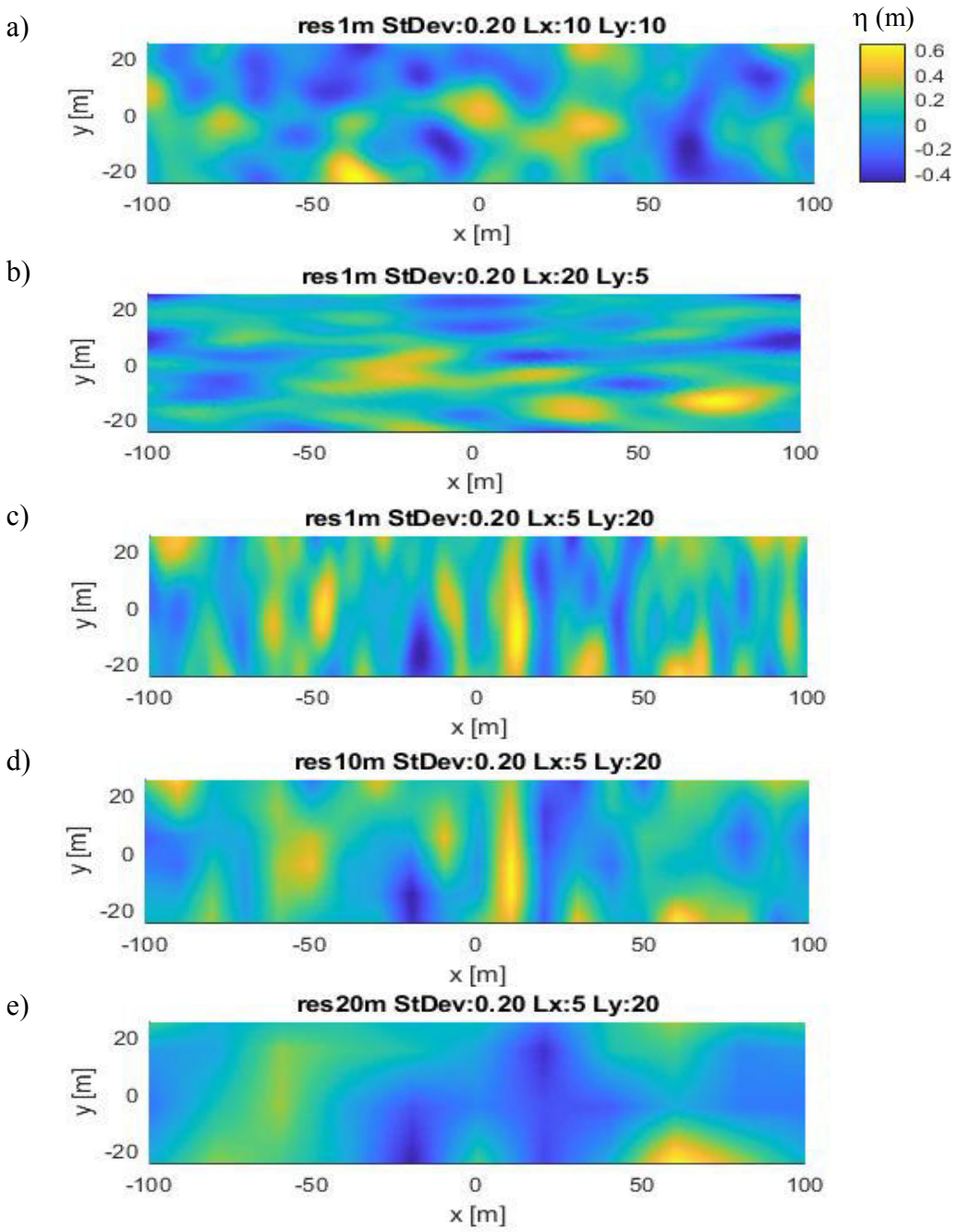

Figure 3.6 Examples of generated random bathymetries: in a), b), c), bed morphologies with different correlation lengths; in c), d), e) same bathymetry at decreasing resolutions.

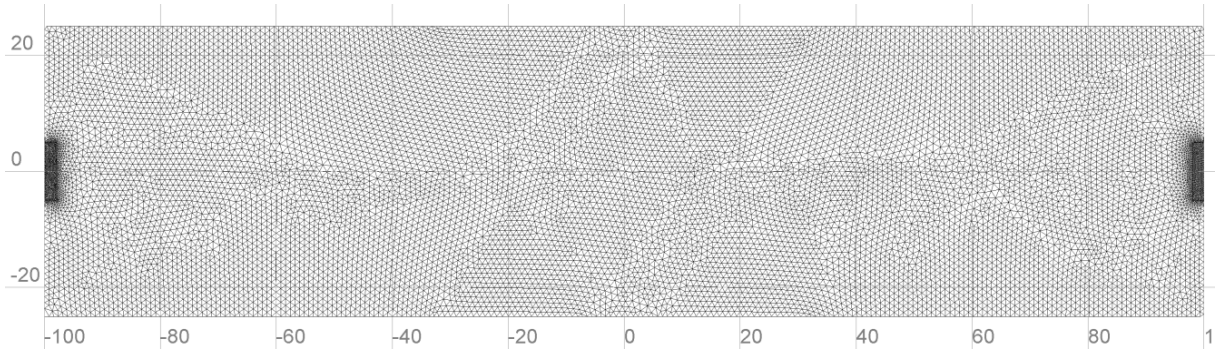

Figure 3.7 Telemac 2D computational mesh for the wetland case.

3.5.2 Simulated bathymetric configurations

First simulations in this study were performed for different transversal and longitudinal correlation lengths, comparing the effect on removal performance of flat, isotropic, anisotropic bed forms of different sizing. The performed simulations at the present stage are reported in Table 3.1. A total of 17 cases (bathymetries) were generated, with one flat bathymetry as reference case and two series of 8 bathymetries with same bottom elevation variance σ_z (i.e., 0.1 m and 0.2 m) and varying correlation lengths. After some initial results (cases s1÷s5) showed a greater efficiency increase for the isotropic morphology, more effort was made in exploring isotropic bed forms characterized by different correlation lengths. Following results showed that also anisotropic bathymetries could improve efficiency metrics.

In order to compare isotropic and anisotropic bed forms, a dimensionless parameter f was introduced for characterize topographies with similar "frequency" of the bed forms:

$$\mathrm{f} = A_w (L_x L_y)^{-1} \qquad (3.25)$$

It takes into account both longitudinal and transversal correlation lengths; with lower L_x and/or L_y, f was greater and the bathymetry was characterized by a bigger number of smaller bed forms (isotropic bumps/pools or elongated "wrinkles"/channels); with higher L_x and/or L_y, f was smaller and the domain contained less bed forms of bigger size.

Table 3.1 Studied bathymetries, with their bathymetric features: type (flat, isotropic, anisotropic with transversal forms, anisotropic with longitudinal forms) and statistical parameters (bottom elevation variance σ_z, correlation lengths L_x and L_y, dimensionless parameter f). In blue color and *italics*, bathymetries with equal f value.

Simul.	type	σ_z (m)	L_x (m)	L_y (m)	$f = A(L_x L_x)^{-1}$ (%)
s1	flat	0	0	0	∞
s2	isotropic	0.2	10	10	100
s3	*transversal*	*0.2*	*2*	*20*	*250*
s4	*longitudinal*	*0.2*	*20*	*2*	*250*
s5	*isotropic*	*0.2*	*6.3*	*6.3*	*252*
s6	*transversal*	*0.1*	*2*	*20*	*250*
s7	*longitudinal*	*0.1*	*20*	*2*	*250*
s8	*isotropic*	*0.1*	*6.3*	*6.3*	*252*
s9	isotropic	0.2	4	4	625
s10	isotropic	0.2	2	2	2500
s11	isotropic	0.1	4	4	625
s12	isotropic	0.1	2	2	2500
s13	isotropic	0.1	10	10	100
s14	isotropic	0.2	3	3	1111
s15	isotropic	0.1	3	3	1111
s16	transversal	0.2	5	5	400
s17	longitudinal	0.1	5	5	400

For each simulation, the mean residence time $t_m$and the variance $\sigma^2$of the residence time distribution function F(t) were calculated from the concentration curve at the outlet $C_{out}(t)$. From these parameters, the efficiency indexes were estimate (see section 3.3): number of continuously stirred tank reactors $N = (t_n/\sigma)^2$, dispersion efficiency $e_d = 1 - 1/N$, volumetric efficiency $e_v = t_m/t_n$, hydraulic efficiency index or Persson's index $\lambda_p = e_v * e_d$.

3.6 Results and discussion

The flat bathymetry was used as reference case (simulation s1) and its efficiency indexes were the base for comparing the removal performances obtained for the not-flat bathymetries. The tested cases had same volume V_{tot} (the magnitude of bed forms were symmetrically distributed below and above the mean water depth) and same inflow, thus the nominal residence time was the same, $t_n = \frac{V}{Q} = \frac{5000}{0.025} = 200000s = 2.3d$. Their performances were directly comparable because they only depended on the variations of $t_m$and σ^2 caused by variations of the topographic configuration. In particular, it was quantified the relative difference in Persson's index $\Delta\lambda_p$ between each simulation and the flat one $\lambda_{p,flat}$:

$$\Delta\lambda_p = \frac{(\lambda_p - \lambda_{p,flat})}{\lambda_{p,flat}} \qquad (3.26)$$

Table 3.2 Efficiency indexes for the tested bathymetry cases. In blue color and *italics*, bathymetries with equal f value.

Simul.	σ_z (m)	L_x (m)	L_y (m)	f %	T_m (x10^5s)	σ^2 (x10^9s^2)	N	e_d	e_v	λ_p	$\Delta\lambda_p$
s1	0	0	0	∞	1.37	1.28	31.33	0.968	0.685	0.663	0%
s2	0.2	10	10	100	1.33	1.31	30.57	0.967	0.666	0.644	-2.9%
s3	*0.2*	*2*	*20*	*250*	*0.83*	*1.87*	*21.34*	*0.953*	*0.417*	*0.398*	*-40.1*
s4	*0.2*	*20*	*2*	*250*	*1.48*	*1.64*	*24.44*	*0.959*	*0.738*	*0.708*	*6.7%*
s5	*0.2*	*6.3*	*6.3*	*252*	*1.51*	*1.86*	*21.54*	*0.954*	*0.753*	*0.719*	*8.3%*
s6	*0.1*	*2*	*20*	*250*	*1.55*	*1.05*	*37.97*	*0.974*	*0.776*	*0.756*	*13.9%*
s7	*0.1*	*20*	*2*	*250*	*1.44*	*1.14*	*35.16*	*0.972*	*0.721*	*0.700*	*5.5%*
s8	*0.1*	*6.3*	*6.3*	*252*	*1.48*	*1.14*	*35.09*	*0.971*	*0.741*	*0.720*	*8.5%*
s9	0.2	4	4	625	1.46	1.84	21.78	0.954	0.732	0.698	5.2%
s10	0.2	2	2	2500	1.58	1.31	30.48	0.967	0.79	0.764	15.10%
s11	0.1	4	4	625	1.34	1.34	29.82	0.966	0.672	0.649	-2.1%
s12	0.1	2	2	2500	1.40	1.20	33.36	0.97	0.701	0.68	2.5%
s13	0.1	10	10	100	1.32	1.06	37.62	0.973	0.658	0.641	-3.4%
s14	0.2	3	3	1111	1.54	1.28	31.32	0.968	0.769	0.745	12.3%
s15	0.1	3	3	1111	1.28	1.27	31.49	0.968	0.642	0.622	-6.3%
s16	0.2	5	5	400	1.38	2.11	18.93	0.947	0.691	0.654	-1.4%
s17	0.1	5	5	400	1.44	1.32	30.4	0.967	0.72	0.697	5.0%

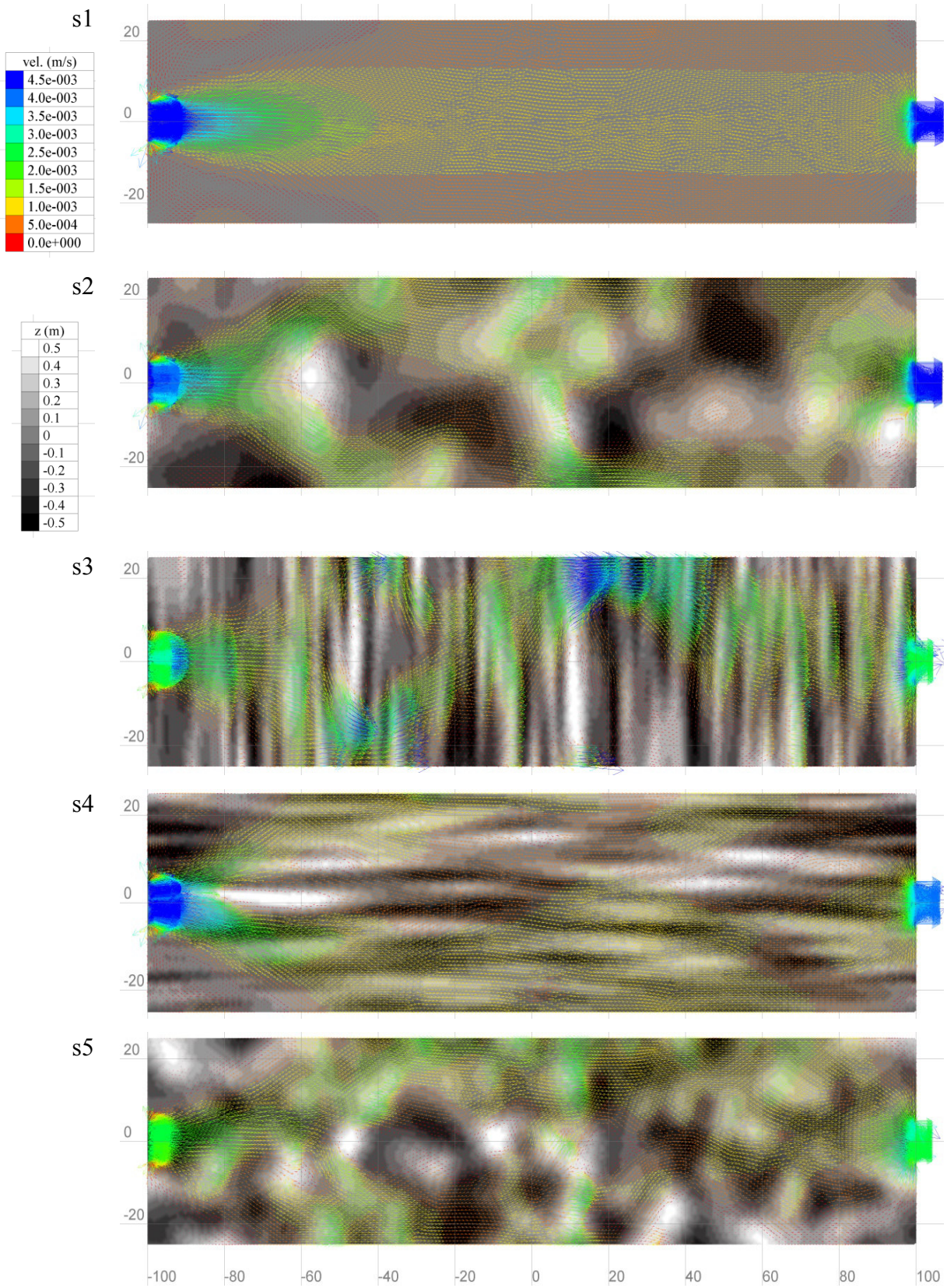

Figure 3.8 Flow field and bottom elevation for the first 5 simulations.

Table 3.2 reports the efficiency indexes obtained for the simulations. The parameter $\Delta\lambda_p$ represented a comprehensive metric for evaluating if there were or not improvements in the removal performance with respect to the flat case. The mean residence time t_m and the

variance σ^2 could explain how the bathymetry affected the hydraulic efficiency index. The flow paths from Telemac calculations gave a visual confirmation about the variations of the hydrodynamic field (Figure 3.8).

First simulations carried (s1÷s5) showed very different values $\Delta\lambda_p$. In particular, there were an evident worsening for case s3, the transversal-bed-forms bathymetry, for which $\Delta\lambda_p = -40.1\%$ and a 8.3% improvement for case s5, with isotropic patches with L=5m. In addition, comparing the two isotropic cases s2 and s5, it was found that higher L could decrease $\Delta\lambda_p$: -2.9% for case s2 (L=10 m), +8.3% for s5 (L=6.3 m). Looking at the flow paths of these simulations, it was evident that bottom topography affected short-circuiting and formation of stagnant areas. This produced not always efficient ways for using the wetland volume. Especially in case s3 there were wide recirculation zones or "hidden" zones downstream the elongated bed forms and some preferential paths were velocities increased (blue colour in Figure 3.8). In this condition t_m decreased and σ^2 increased: the two combined had the effect of lowering λ_p. In the best case, s5, the flow paths were quite heterogeneous, with some stagnant areas and some faster paths, so the variance σ^2 was similar to that of case s3. In contrast, there were a higher spreading of the flow in the domain and a general decreasing of velocities, leading to the highest t_m in these 5-simulations series. The two combined gave the highest increase of λ_p, thanks to a better use of the wetland volume.

From these first observations, the study was addressed to analyze more isotropic morphologies and only a few anisotropic topographies. Considering the improvement had from L = 10 m (case s2) to L = 6.3 m (case s5), they were generated case with smaller L (and smaller size of patches): L = 5, 4, 3, 2 m. Then, the whole set of bathymetries with σ_z =0.2 m (cases: s2, s3, s4, s5, s9, s10, s14, s16) was replied with a smaller bottom elevation variance, i.e. σ_z = 0.1 m (cases: s6, s7, s8, s11, s12, s13, s15, s17). In this way it was possible to study the variations of λ_p for bed forms with smaller size in both the horizontal and /or the vertical plane.

Results are reported in Table 3.2 and graphically summarized in some plots in Figure 3.9 for isotropic bed forms, and in Figure 3.10 for comparing the three type of morphologies (isotropic, transversal, longitudinal). For the isotropic series with σ_z =0.2 m, decreasing L (higher f) showed a general improvement in efficiency λ_p, passing from a minimum value 0.644 (-2.9% lower than $\lambda_{p,flat}$ of the flat bathymetry) to the higher value 0.764 for case s10 (+15.1% than $\lambda_{p,flat}$). Considering Persson's classification, efficiency passed from satisfactory to good level ($\lambda_p > 0.75$). One case, s5, with L = 6.3 m, showed a λ_p value

greater than the apparent trend showed by the other cases. The same sequence of isotropic bathymetries with $\sigma_z = 0.1$ m resulted in efficiencies with no evident trend and values in the range 0.622 ÷ 0.756 (- 6.3% ÷ + 13.9% than the flat case). Analyzing t_m and σ^2, it could be noticed that series with $\sigma_z = 0.2$ m had T_m generally increasing with increasing f values, indicating a greater effective volume V_{eff}, while variance showed both high and low values, representative of different uniformity grade in the flow fields. In this series, decreasing L improved the use of the wetland volume (simulation s10 in Figure 3.11). On the other hand, isotropic series with $\sigma_z = 0.1$ m had generally lower T_m than series $\sigma_z = 0.2$ m, but also lower values of σ^2. Thus, for this series the lower vertical magnitude of the bed forms seemed to less improve the use of the volume (lower T_m means lower V_{eff}) but to more improve in lowering the mixing (lower σ^2).

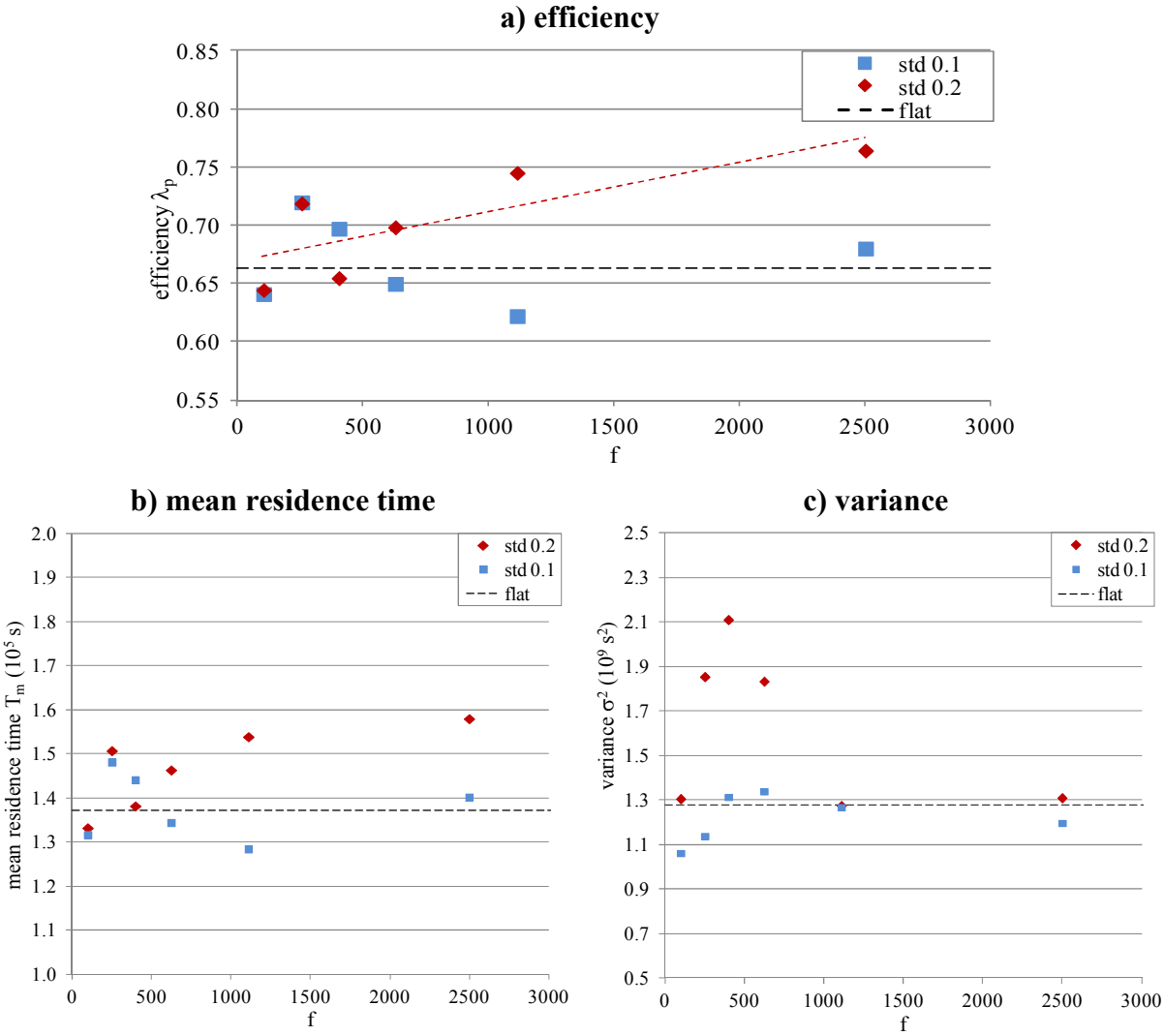

Figure 3.9 Isotropic morphologies results: a) Persson's efficiency index λ_p; b) mean residence time T_m; c) variance σ^2. "std" indicates the bottom elevation variance σ_z of the series. In dashed black line the values for the reference flat case. In dotted red line the regression line for efficiency for series "std 0,2".

Comparing bathymetries with same f value but different type of bed forms (isotropic, transversal, longitudinal), the results were similar for isotropic and longitudinal cases, while transversal cases gave much different efficiency: -40.1% for case s3 with σ_z = 0.2 m and +13.9% for case s6 with σ_z = 0.1 m (Figure 3.10). They were only a few cases, thus no general conclusions could be made about which type of bathymetry could be the "better" for efficiency improvement. They showed that the type of bathymetry and its magnitude could greatly affect hydraulic efficiency.

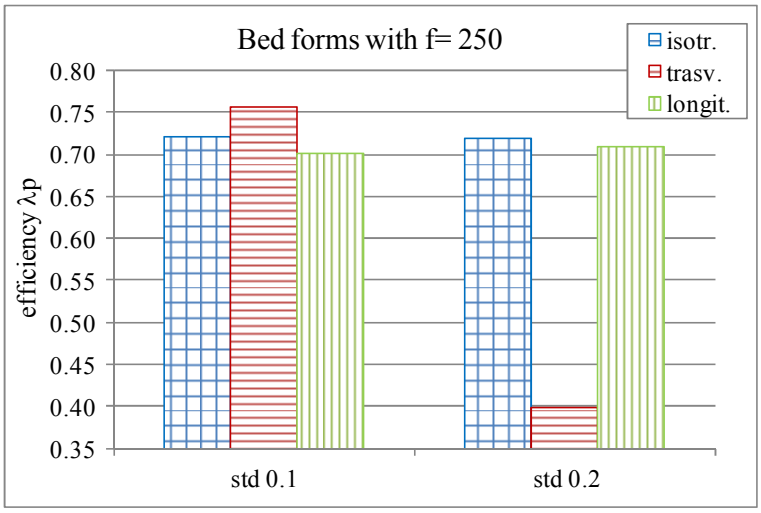

Figure 3.10 Comparison between different type of bathymetries (isotropic, anisotropic transversal, anisotropic longitudinal), for two values of σ_z =0.1 m and σ_z =0.2 m (indicated as "std 0.1" and "std 0.2").

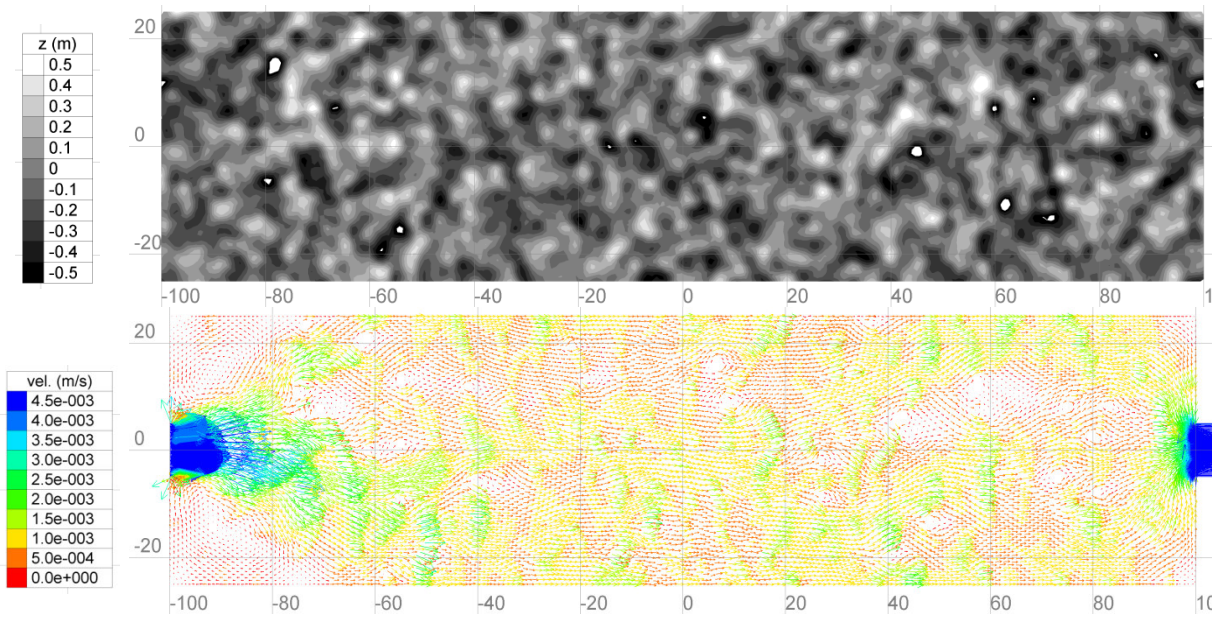

Figure 3.11 Bathymetry and velocity field for the more efficient simulation, the isotropic s10 with $\sigma_z = 0.2m, L_x = L_y = 2m$.

In the 17 simulations carried in this first application of the developed model, the greater improvement was obtained for the isotropic case s10 with σ_z =0.2 m and L= 2 m, with $\Delta\lambda_p$= +15.1% (Figure 3.11).

It should be stressed that in this exploratory study, only one random bathymetry was generated for each combination of parameters (σ_z, L_x, L_y). For inferring statistically-based conclusions at least 10-15 random bathymetries should be generated for each (σ_z, L_x, L_y) combination. That is, taking as example the presented study, at least 16 combinations x 10 random bathymetries (flat case not included).

3.7 Conclusions

A modelling system composed by random-bathymetry generator, hydrodynamic model and solute transport model was developed for the study of removal efficiency performance of free water surface constructed wetlands. It was applied at 12 cases with isotropic bed forms of different size and vertical magnitude, 4 cases with anisotropic topographies and 1 flat case used as reference. The preliminary results showed that bathymetric configuration of a wetland affects its hydrodynamics and removal performance, but more simulations are needed for obtaining a statistically-robust comparison between different bathymetric configurations.

This topic have the potential of interesting further possible developments: study of not uniform distribution of the roughness, effect of lower resolution in the bathymetric information and implementation of frameworks including removal effect of vegetation, processes of mass exchange in the hyporheic zone, biological activity.

3.8 Bibliography

Abbas, H., Nasr, R., Seif, H., (2006). Study of waste stabilization pond geometry for the wastewater treatment efficiency. Ecol. Eng. 28, 25–34. doi:10.1016/j.ecoleng.2006.03.00

Adamsson, Å., Bergdahl, L., Vikström, M. (2002). A Laboratory Study of the Effect of an Island to Extend Residence Time in a Rectangular Tank. In: Proceedings of the Ninth International Conference on Urban Drainage. American Society of Civil Engineers, 1–10. Portland, Oregon. http://dx.doi.org/10.1061/40644.

Arega F, Sanders BF (2004). Dispersion model for tidal wetlands. J. Hydraul. Eng.130 (8), 739–754.

Calhoun, D., LeVeque, R.J.,(2000). A Cartesian Grid Finite-Volume Method for the Advection-Diffusion Equation in Irregular Geometries, Journal of Computational

Physics, Volume 157, Issue 1, 2000, Pages 143-180, ISSN 0021-9991, https://doi.org/10.1006/jcph.1999.6369.

Conn RM, Fiedler FR. (2006) Increasing hydraulic residence time in constructed stormwater treatment wetlands with designed bottom topography. Water Environ. Res. 2006;78:2514– 2523.

Fogler HS (1992) Elements of chemical reaction engineering. Prentice-Hall, Englewood cliffs

German, J., Kant, H., (1998). FEM-analys av strmningsförhållanden i en dagvattendamm (FEM-analysis of the hydraulic conditions in a stormwater detention pond). Vatten 54 (3), 183–190 (in Swedish).

Guzman, C.B., Cohen, S., Xavier, M., Swingle, T., Qiu, W., Nepf, H.Hide (2018). Island topographies to reduce short-circuiting in stormwater detention ponds and treatment wetlands. Ecological Engineering, Volume 117, July 2018, Pages 182-193, ISSN 0925-8574, doi.org/10.1016/j.ecoleng.2018.02.020.

Jenkins G a., Greenway M (2005). The hydraulic efficiency of fringing versus banded vegetation in constructed wetlands. Ecol Eng 25:61-72. doi: 10.1016/j.ecoleng.2005.03.001

Kadlec R, Knight R (1996). Treatment Wetlands. CRC Press, Boca raton, FL

Khan, S., Melville, B., Shamseldin, A., (2011). Retrofitting a stormwater retention pond using a deflector Island. Water Sci. Technol. 63 (12), 2867–2872. http://dx.doi.org/ 10.2166/wst.2011.569.

Lightbody, A., Nepf, H., Bays, J., (2007). Mixing in deep zones within constructed treatment wetlands. Ecol. Eng. 29 (2), 209–220. http://dx.doi.org/10.1016/j.ecoleng. 2006.11.001.

Martinez,C.J., and W.R.Wise (2003). Analysis of constructed treatment wetland hydraulics with the transient storage model OTIS, Ecological Engineering, 20(3), 211–222.

Musner T, Bottacin-Busolin a., Zaramella M, Marion A (2014). A contaminant transport model for wetlands accounting for distinct residence time bimodality. J Hydrol 515:237–246. doi: 10.1016/j.jhydrol.2014.04.043

Persson, J., Somes, N., Wong, T., (1999). Hydraulics efficiency of constructed wetlands and ponds. Water Sci. Technol. 40 (3), 291–300. http://dx.doi.org/10.1016/S0273-1223(99)00448-5.

Persson, J., 2000. The hydraulic performance of ponds of various layouts. Urban Water 2 (3), 243–250. http://dx.doi.org/10.1016/S1462-0758(00)00059-5.

Sabokrouhiyeh N, Bottacin-Busolin A, Nepf H, Marion A (2016). Effects of vegetation density and wetland aspect ratio variation on hydraulic efficiency of wetlands. Hydrodynamic and Mass Transport at Freshwater Aquatic Interfaces, 101-113

Sabokrouhiyeh, N., Bottacin-Busolin, A., Savickis, J., Nepf, H., Marion, A., (2017). A numerical study of the effect of wetland shape and inlet-outlet configuration on wetland performance. Ecol. Eng. 105, 170–179. doi:10.1016/j.ecoleng.2017.04.062

Savickis J, Bottacin-Busolin A, Zaramella M, Sabokrouhiyeh N, Marion A, (2016). Effect of a meandering channel on wetland performance. J Hydrol 535:204–210. doi: 10.1016/j.jhydrol.2016.01.082

Thackston EL, Shields FD, Schroeder PR (1987) Residence Time Distributions of Shallow Basins. J Environ Eng 113:1319–1332. doi: 10.1061/(ASCE)0733 9372(1987)113:6(1319)

Werner TM, Kadlec RH (1996) Application of residence time distributions to stormwater treatment systems. Ecol Eng 7:213–234. doi: 10.1016/0925-8574(96)00013-4

Chapter 4

4 Application of the STIR model to a small river at different river flow rates [2]

4.1 Introduction

The need to protect the natural environment from the effects of pollution incidents has driven the development of many mathematical models based on the principles of conservative or non-conservative solute transport in open channels (Fischer et al., 1979; Rutherford, 1994). Over time, as observations revealed the weaknesses of early modelling efforts, such as the advection-dispersion equation (ADE), more processes were included in the models. Thus the major transport mechanisms of advection and dispersion were supplemented with the effects of transient storage, creating the transient storage model (TSM), in the majority of published work since the turn of the century. It is interesting to reflect, however, that the realisation that the classical ADE model was sometimes inadequate (Nordin and Sabol, 1974; Day, 1975), the likely cause being temporary trapping of solute in so-called dead zones (Valentine and Wood, 1979; Beer and Young, 1983) and the proposal to portray transient storage using a simple

[2] The content of this chapter was presented at 38th International School of Hydraulics, Łąck, Poland (May 2019). It is described in the paper: Wallis S.G. and Dallan E. (2019) *Application of the STIR model to a small river at different flow rates*, accepted for publication in the SPRINGER monographic series: "GeoPlanet: Earth and Planetary Sciences", indexed by Scopus and by Web of Science.

exchange mechanism between a river's main channel and its peripheral dead zones (Thackston and Krenkel, 1967; Bencala and Walters, 1983), all have long histories.

The promise of the TSM was augmented by the realisation that it was capable of catering both for the effects of dead zones and for the effects of the hyporheic zone (Elliott and Brooks, 1997). Furthermore, by developing a variation on the standard model, which included more than one solute exchange time-scale (Choi et al., 2000; Briggs et al., 2009), the model became potentially more widely applicable to real channels. A further innovation characterised the solute exchange between the main channel and the storage zones using a general residence time distribution approach for single (Gooseff et al., 2003b) or multiple storage zones (Marion et al., 2008; Bottacin-Busolin et al., 2011).

In this paper we report on the first stage of the application of one of these later models, namely the STIR model, to a set of tracer experiments undertaken over a range of river flow rates in a small river. Whilst the larger potential of the STIR model lies in its multiple storage zone capability, here we focus on its single storage zone form. The aims of the work are to examine the variation of the model's parameters with river flow rate and to compare the results with previously published work.

4.2 Modelling background

The STIR model describes conservative solute transport along a river as the combination of advection and dispersion in the main channel and retention of solute in storage zones. Considering n storage zones, solute mass balance in the main channel is expressed as:

$$\frac{\partial \mathrm{C(x,t)}}{\partial \mathrm{t}} + u\frac{\partial \mathrm{C(x,t)}}{\partial \mathrm{x}} = D\frac{\partial^2 \mathrm{C(x,t)}}{\partial x^2} - \sum_{i=1}^{n}\left\{\alpha_i \mathrm{C(x,t)} - \int_0^{\mathrm{t}} \alpha_i \mathrm{C(x,t)}\varphi_{\mathrm{i}}(\mathrm{t}-\tau)\,\mathrm{d}\tau\right\} \quad (4.1)$$

where: C, solute concentration in the main channel; u, velocity in the main channel; D, dispersion coefficient in the main channel; α_i, mass exchange rate for the ith storage zone; φ_i, residence time function for the ith storage zone; τ, a dummy time variable; x, distance along the river; t, time and n, number of storage zones (Marion et al., 2008).

In this study we consider the special case for n =1 and assume an exponential residence time distribution for the storage zone. Under these circumstances the model is equivalent to the TSM (Marion et al., 2008). However, the way in which the STIR model equation is solved is rather different to the usual way in which the TSM model equations are solved. In the latter a numerical solution approach is used to approximate spatial and temporal gradients (Wallis

et al., 2013) whereas STIR employs a purely time-domain convolution method (Marion et al., 2008).

4.3 Tracer data

The data used in this work came from tracer experiments undertaken in the Murray Burn. This small river runs through the Riccarton Campus of Heriot-Watt University near Edinburgh, and has previously been the focus of a travel time study (Burke, 2002; Wallis, 2005) and a longitudinal mixing study (Heron, 2015; Wallis and Heron, 2018). Herein, we use tracer data from the latter work, which used one of the reaches studied in the former work. This reach extends between its upstream boundary, designated as Site 3, and its downstream boundary, designated as Site 4. Eleven gulp-release tracer experiments were undertaken between November 2009 and November 2010 covering a river flow rate range of about 15-400 L s^{-1}. The tracer (Rhodamine WT) was injected 230 m upstream of Site 3 and water samples were collected in glass bottles at Site 3 and Site 4. The sampling interval varied between 2 minutes at low river flow rates to 20 seconds at high river flow rates. The samples were analyzed under temperature controlled laboratory conditions using a calibrated Turner Designs Model 10 instrument (Heron, 2015). The first two experiments were trials, which were used to fine tune the experimental work in the field. They did not yield complete and well-resolved temporal concentration profiles. Therefore nine sets of tracer data were available for use.

In order to prepare the data for modelling purposes, three processing steps were undertaken for each experiment. Firstly, the background signal was removed; secondly, the calibration factor of the fluorometer was used to convert the data into concentrations; thirdly the concentration data was scaled so that the area under the upstream and downstream profiles was the same. The final step is important because it removes any real or apparent non-conservative behavior of the tracer. The latter is often found in tracer data due to the presence of distributed or point inflows from land drainage or tributaries, respectively.

4.4 Application of the STIR model

The STIR model, comprising a single storage zone and an exponential residence time distribution, was optimized to the processed tracer data in three different applications. Firstly, the model was optimized to the processed tracer data at Site 3 using the gulp-release at the tracer injection site as the upstream boundary condition; secondly, the model was optimized to the processed tracer data at Site 4 using the gulp-release at the tracer injection site as the

upstream boundary condition; thirdly, the model was optimized to the processed tracer data at Site 4 using the processed tracer data at Site 3 as the upstream boundary condition. The reaches corresponding to these applications are denoted as I3, I4 and 34, respectively. Their characteristics are summarized in Table 4.1.

Table 4.1 Physical characteristics of the reaches modeled.

Reach	Length (m)	Mean width (m)	Mean slope	Description
I3	236	3.5	0.021	Upper 100 m: natural channel, meandering, boulders Lower 136 m: modified channel, straight, cobbles
I4	420	3.0	0.016	Upper 100 m: natural channel, meandering, boulders Lower 320 m: modified channel, straight, cobbles
34	184	2.4	0.009	Throughout: modified channel, straight, cobbles

In all cases, four reach-average parameters were estimated: the cross-sectional area of the main channel A, the dispersion coefficient in the main channel D, the exchange rate between the main channel and the storage zones α and the mean residence time in the storage zones T. The ratio of storage area A_s to main channel area was calculated from the latter two parameters (Marion et al., 2008).

In order to reduce the possibility that a too coarse temporal resolution of the tracer data might affect the results (Wallis and Manson, 2018), the concentration data were interpolated to a time step of 2.5 s. Furthermore, in order to prevent longer time-scale transient storage from contaminating the results the concentration profiles were truncated at a time equal to $4t_p$, where t_p, is the time delay between the first rise of a profile above background and the profile peak. This procedure was aimed at ensuring that all the concentration profiles had similar lengths to their tails: it also cut off some rather poorly defined ends to some of the tails caused by spikes in the data. Optimization was achieved using a mixed approach in which a linear fitting was applied around the peak of the observed downstream profile and a logarithmic fitting was applied on the tail of the observed downstream profile. This method tends to produce better all-round fits to the whole profile than can be achieved using either a completely linear fitting or a completely logarithmic fitting. Examples of the fits for one experiment are shown in Figure 4.1 for reaches I3 (upper panels), I4 (middle panels) and 34 (lower panels) using both linear (left-hand panels) and logarithmic (right-hand panels) concentration scales.

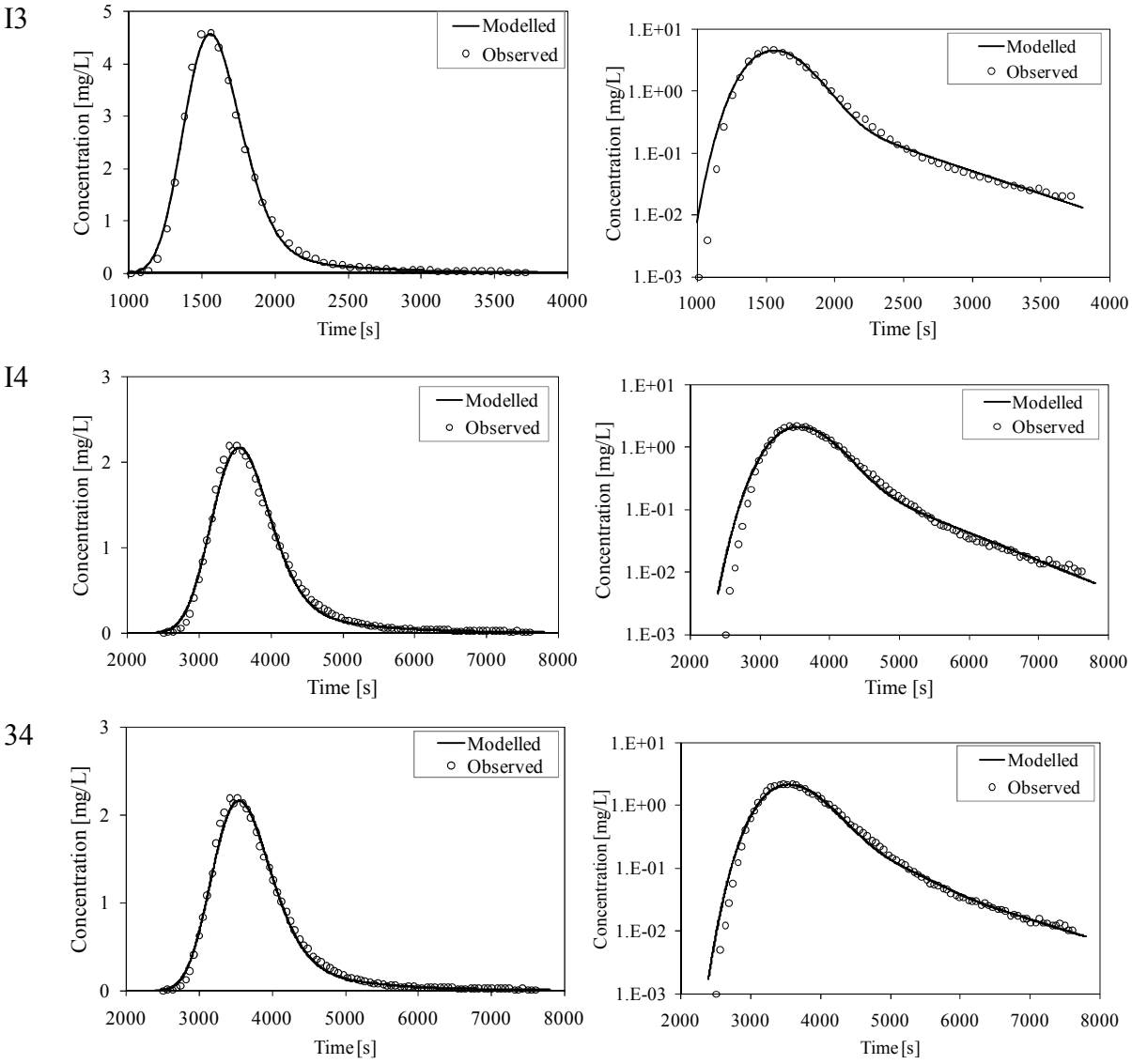

Figure 4.1 Model fits for Experiment #7 shown using linear (left-hand panels) and logarithmic (right-hand panels) concentration scales: upper panels, reach I3; middle panels, reach I4; lower panels, reach 34.

4.5 Results and discussion

Results were obtained for all three application cases for the nine experiments. Figure 4.2 shows optimized main channel cross-sectional areas and main channel dispersion coefficients plotted against river flow rate for the three application cases. In general, both parameters increase with river flow rate, as would be expected from the principles of open channel flow and from theoretical dispersion studies (Rutherford, 1994). Furthermore, in four out of five previously published studies where the TSM was optimized to field-scale tracer data observed in a single reach at several river flow rates, a positive correlation between main channel dispersion coefficient and river flow rate was found (Hart et al., 1999; Gooseff et al., 2003;

Jin and Ward, 2005; Camacho and Gonzalez, 2008). In the fifth study (Manson and Wallis, 2018), a weak decreasing trend was found.

Support for the main channel cross-sectional areas is provided by the results of Heron (2015). His results were obtained by optimizing the analytical solution to the ADE for a gulp-release of tracer, thus obtaining direct results for cross-sectional mean velocities for cases I3 and I4. Cross-sectional areas were obtained by dividing the river flow rate by the cross-sectional mean velocities. His results are plotted on the relevant parts of Figure 4.2 (left-hand side, upper two panels). In general they are slightly larger than those from the present study (typically by 1% for reach I3 and by 2% for reach I4), because they reflect the total cross-sectional area, i.e. main channel plus storage zones. Furthermore, Heron (2015) estimated the cross-sectional mean velocity for the case 34 from a travel time based weighted average of the cross-sectional mean velocities from cases I3 and I4. The corresponding cross-sectional areas are plotted on the lower panel of Figure 4.2 and are also slightly larger than the results from STIR (typically by 3%). Heron (2015) also found that his weighted average cross-sectional area results for reach 34 were consistent with estimates obtained from other methods applied directly to reach 34, such as Fischer (1968)'s routing procedure (the former being typically 2% greater than the latter). As would be expected, the cross-sectional areas are inversely correlated with the channel slopes given in

Table 4.1. Taking into account the different channel widths, this implies that the flow in reach 34 is generally slower and deeper than the flow in reach I3 at the same river flow rate. This is consistent with visual observations of the channel hydraulics.

Heron (2015)'s optimization of the analytical solution to the ADE for a gulp-release of tracer also provides direct results for dispersion coefficients for cases I3 and I4. These are shown in Figure 4.2 (right-hand side upper two panels), and are generally larger than the results from STIR (typically by 22% for reach I3 and by 25% for reach I4). This is expected because the results from STIR only reflect the main channel dispersion whilst Heron's results reflect the total dispersion occurring in the reach (main channel dispersion plus the effects of transient storage). Heron (2015) also estimated the dispersion coefficient for reach 34 using the same travel time based weighted average approach referred to above. These are plotted on the lower panel of Figure 4.2 and, as before, are generally larger (typically by 66%) than the results from STIR. In contrast to the close agreement between cross-sectional area estimates, however, Heron (2015)'s weighted average dispersion coefficients were about 32% greater than those obtained from Fischer's routing procedure, so the former may be overestimates. It

is worth noting that the magnitudes of the dispersion coefficients in all three reaches are consistent with those found in other small rivers (Heron, 2015), being of the order of 1 m^2/s.

Regarding the STIR model results, the dispersion coefficients in reach 34 are smaller than in reach I3. This is a reflection of the different physical nature of the reaches, particularly the upper part of reach I3 (see Table 4.1) which is a natural, non-uniform channel containing relatively large roughness elements whilst the remaining part of reach I3 and reach 34 have been modified by landscape management to create a much more uniform and straighter channel and which contain smaller roughness elements. The generally wider and shallower flow regime in reach I3 compared to reach 34, mentioned above, also has an influence. The dispersion coefficients in reach I4 lie between those in the other two reaches, reflecting that reach I4 consists of reach I3 in series with reach 34.

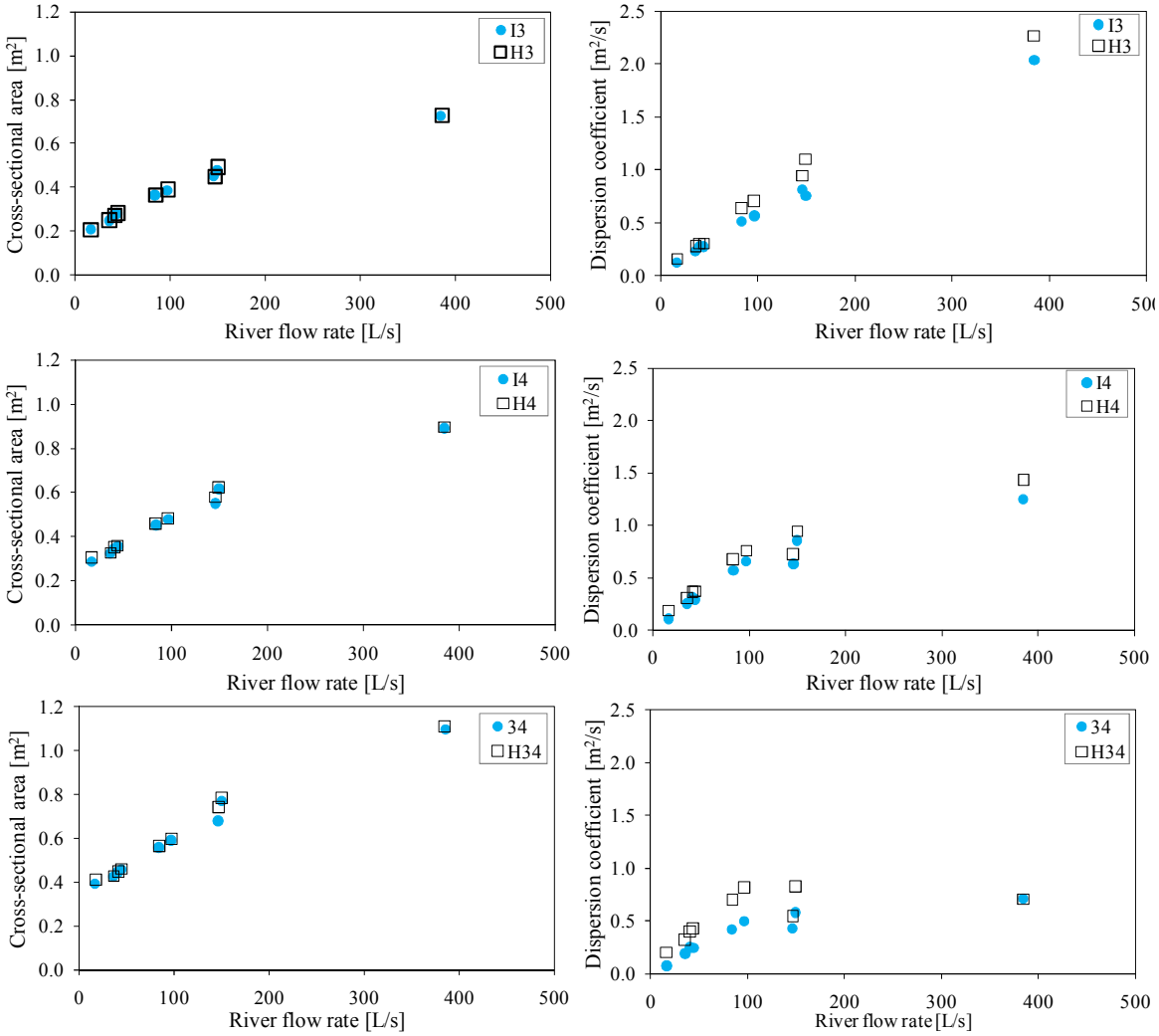

Figure 4.2 Variation of optimized main channel cross-sectional area A and main channel dispersion coefficient D with river flow rate for three application cases: STIR results indicated by I3, I4 & 34; Heron (2015)'s results indicated by H3, H4 & H34, respectively.

Figure 4.3 shows optimized exchange rates, optimized mean residence times, calculated area ratio and a normalized measure of fit between the observed and modelled downstream concentration profiles. The results are plotted against river flow rate for the three application cases. The exchange rates for I4 and 34 are similar to each other whilst those for I3 are generally larger: they are approximately constant over the range of river flow rate covered and only I3 showed a slightly increasing trend. This general invariance contrasts with an increasing trend reported by Hart et al. (1999), Gooseff et al. (2003), Camacho and Gonzalez (2008) and Manson and Wallis (2018): there is no clear pattern at all in the results of Jin and Ward (2005).

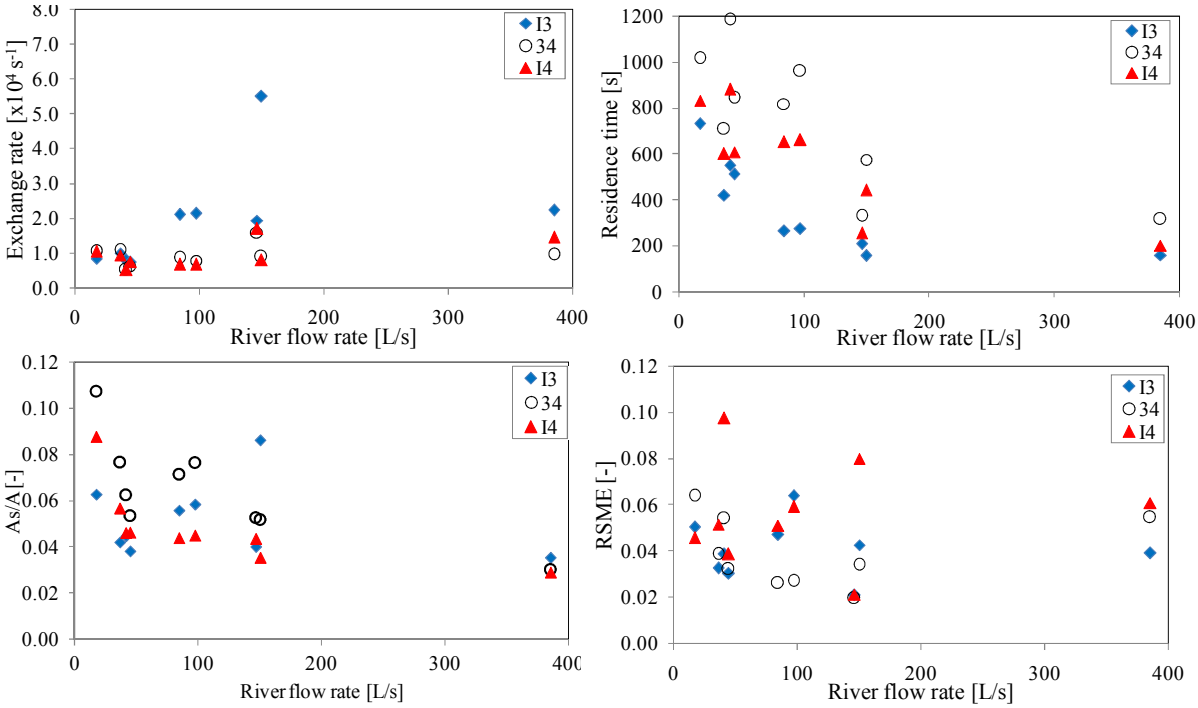

Figure 4.3 Variation of exchange rate, residence time, area ratio and normalized model fit with river flow rate for three application cases I3, I4 & 34.

The mean residence time for reach 34 is always larger than the mean residence time for reach I4, whilst reach I3 has the smallest residence time in all the experiments. The residence times for all three cases reduce with increasing river flow rate. The differing transient storage behavior of the reaches implied by the exchange rate and residence time results is probably a reflection of the different geomorphology of the reaches referred to above, but in the absence of more detailed information on the flow structures in the reaches it is difficult to propose a mechanism to justify this. There are no consistent differences between the area ratios for reaches I3 and I4, but the area ratio in reach 34 is the largest in the majority of the experiments. Interestingly, all three of the area ratios reduce as river flow rate increases,

which is consistent with Gooseff et al. (2003) and Camacho and Gonzalez (2008). In contrast Hart et al. (1999), Jin and Ward (2005) and Manson and Wallis (2018) found no trend. This different behavior is probably caused by the different geomorphologies of the rivers. For example, rivers with storage zones being predominantly located in the bed may see a reduction in area ratio with increasing river flow rate because no additional storage zones become available as water levels increase. However, rivers with storage zones being predominantly located in the banks may see little change in area ratio with increasing river flow rate because new storage zones become available as water levels rise. The magnitudes of the area ratio found in the current study are towards the lower end of the ranges reported in those sources. The model fit results reveal little substantial information. For example, model fits for reach I4 are poorer than for both reaches I3 and 34 in six of the nine experiments, whilst fits for reach 34 are poorer than for reach I3 in five of the nine experiments. There is no discernible trend between model fit and river flow rate in any of the reaches.

4.6 Conclusions

The parameters of the STIR model, comprising a single storage zone and an exponential residence time distribution, were found by optimizing the model to a set of tracer data for three reaches of the Murray Burn in Edinburgh. Both the cross-sectional area of the main channel and the dispersion coefficient in the main channel were found to increase with increasing river flow rate as would be expected from previous work. These results were generally consistent with an independent analysis of the tracer data by Heron (2015). In particular the STIR model dispersion coefficients were smaller than Heron's, which reflects that Heron's results quantify both the main channel dispersion and the effect of transient storage. Of the remaining STIR model parameters, the residence time and the area ratio tended to reduce with increasing river flow rate whilst the exchange rate was approximately constant. Overall the dispersion and transient storage parameter results suggest that the upper part of reach I3 has different longitudinal mixing characteristics to other parts of the study site, which reflects differences in the geomorphology along the channel.

4.7 Bibliography

Beer T, Young PC (1983) Longitudinal dispersion in natural streams. J Env Eng Am Soc Civ Eng 109:1049-1067

Bencala KE, Walters RA (1983) Simulation of solute transport in a mountain pool-and-rifle stream: a transient storage model. Water Resour Res 19:718-724

Bottacin-Busolin A, Marion A, Musner T, Tregnaghi M, Zaramella M (2011) Evidence of distinct contaminant transport patterns in rivers using tracer tests and a multiple domain retention model Adv Water Resour 34:737-746

Briggs MA, Gooseff MN, Arp CD, Baker MA (2009) A method for estimating surface transient storage parameters for streams with concurrent hyporheic storage. Water Resour Res 45 W00D27, doi:10.1029/2008WR006959

Burke NA (2002) Travel time and flow characteristics of a small stream system. PhD Thesis, Heriot-Watt University, United Kingdom

Camacho LA, Gonzalez RA (2008) Calibration and predictive ability of longitudinal solute transport models in mountain streams. Environ Fluid Mech 8:597-604

Choi J, Harvey JW, Conklin MH (2000) Characterizing multiple timescales of stream and storage zone interaction that affect solute fate and transport in streams. Water Resour Res 36:1511-1518

Day TJ (1975) Longitudinal dispersion in natural channels. Water Resour Res 11:909-918

Elliott AH, Brooks NH (1997) Transfer of nonsorbing solutes to a streambed with bedforms: theory. Water Resour Res 33:123-136

Fischer HB (1968) Dispersion predictions in natural streams. J San Eng Div Am Soc Civ Eng 94:927-944

Fischer HB, List EJ, Koh RCY, Imberger J, Brooks NH (1979) Mixing in inland and coastal waters. Academic Press

Gooseff MN, McGlynn BL, McGlynn RS (2003) Transient storage processes and stream discharge recession in a headwater stream, Maimai, New Zealand. Proc N Am Benthol Soc Annual Meeting, May 2003 (Poster)

Hart DR, Mulholland DJ, Marzolf ER, DeAngelis DL, Hendricks SP (1999) Relationships between hydraulic parameters in a small stream under varying flow and seasonal conditions. Hydrol Process 13:1497-1510

Heron AJ (2015) Pollutant transport in rivers: estimating dispersion coefficients. MPhil Thesis, Heriot-Watt University, United Kingdom

Jin H-S, Ward GM (2005) Hydraulic characteristics of a small coastal plain stream of the southeastern United States: effects of hydrology and season. Hydrol Process 19:4147-4160

Marion A, Zaramella M, Bottacin-Busolin A (2008) Solute transport in rivers with multiple storage zones: The STIR model. Water Resour Res 44:W10406, doi:10.1029/2008WR007037

Nordin CF, Sabol GV (1974) Empirical data on longitudinal dispersion in rivers. USGS, Water Resour Investig 74-20

Rutherford JC (1994) River Mixing. Wiley

Thackston EL, Krenkel PA (1967) Longitudinal mixing in natural streams. J Sanit Eng Div Proc Am Soc Civ Eng 93:67-90

Valentine EM, Wood IR (1979) Experiments in longitudinal dispersion with dead zones. J Hyd Div Am Soc Civ Eng 105:999-1016

Wallis SG (2005) Experimental study of travel times in a small stream. In: Czernuszenko W, Rowinski PM (eds) Water quality hazards and dispersion of pollutants. Springer 109-120

Wallis SG, Osuch M, Manson JR, Romanowicz R, Demars BOL (2013) On the estimation of solute transport parameters for rivers. In: Rowinski P (ed) Experimental and computational solutions of hydraulic problems. Springer-Verlag 415-425

Wallis SG, Heron AJ (2018) Experimental determination of longitudinal dispersion in a small stream. Proc 5th IAHR Eur Div Conf, Trento, Italy (rpsonline.com.sg/rps2prod/iahr2018)

Wallis SG, Manson JR (2018) Parameter estimation of the Transient Storage Model: sensitivity to discretization. Proc 5th IAHR Eur Div Conf, Trento, Italy (rpsonline.com.sg/rps2prod/iahr2018)

Chapter 5

5 STIR-RST: a software tool for reactive smart tracer studies [3]

5.1 Introduction

The understanding of solute transport processes in rivers has a fundamental role for improving water quality measures and ecological services of surface water bodies. The fate of solutes in rivers and wetlands is influenced by surface hydrodynamics, mass exchanges between the surface water and retention zones, biogeochemical processes.

Over the last few decades, these mechanisms have been extensively studied, and researchers have developed models and experimental techniques to observe the transport of nutrients and pollutants in stream corridors. Usually, parameters for these models are calibrated from data collected in field tracer tests. Most of the modelling frameworks are based on the advection-dispersion equations and the concept of transient storage zones interacting with the main flow. A widely applied model is the Transient Storage Model (TSM), presented by Bencala and Walters (1983), where the storage zone is considered a slow

[3] The content of this chapter is described in the paper submitted to Environmental Modelling & Software (Elsevier): Dallan E., Bottacin-Busolin A., Marion A. *STIR-RST: a software tool for reactive smart tracer studies*.

velocity domain exchanging mass with the surface water. This model served as basis of many single storage zone one-dimensional models, for example the OTIS model (Runkel and Chapra, 1993) and its extended version OTIS-P (Runkel, 1998). These models can't discriminate between different types of storage zones, characterized by different flow conditions, exchange mechanisms, biogeochemical conditions. New models have been developed with two-storage zones, discerning surface transient storage (STS, for example vegetated pocket, pools, superficial dead zones) and hyporheic transient storage (HTS, the near-stream region of the porous boundary): Choi et al., 2000, Marion et al., 2008, Briggs et al., 2009. In particular, the Solute Transport in River (STIR) model (Marion et al., 2008, Bottacin-Busolin et al, 2011) allows to separate the processes using a stochastic approach to determine the residence time distribution (RTD) of distinct storage domains and proposes various forms of the RTDs.

Other descriptions of the hyporheic exchange have been implemented, for example by Haggerty and Reeves (2002), Worman et al (2002), Deng et al. (2006), Boano et al. (2007), Kelly at al. (2017). The Solute Transport an Multirate Mass Transfer-Linear Coordinates (STAMMT-L) proposed by Haggerty and Reeves (2002) was the first model used to represent wide ranges of storage timescales in rivers. It used an advection-dispersion mass transfer equation (ADMTE), where a source-sink term accounting for mass exchange with immobile (storage) domains is added to the advection-dispersion equation (ADE). Worman et al (2002) proposed the advective storage path model and expressed the hyporheic residence time distribution using the advective pumping theory. The fractional model of Deng et al. (2006) used the fractional advection-dispersion equation (FADE). FracFit (Kelly et al., 2017) is a parameter estimation tool supporting four different fractional models. In Boano et al. (2007) the continuous time random walks (CTRW) theory has been the framework for modelling the solute transport in stream.

Most of 2-storage-zones models have a "competing" structure, that is storage zones act in parallel allowing mass transfer with the main flow but not between storage zones Kerr et al. (2013) proposed a "nested" model, where storage zones are arranged in series: the stream exchanges with the STS, the STS exchanges with the HTS. This study demonstrated that calibrated model parameters are affected by the model structure, and this was achieved using a reactive tracer.

Transient storage zones also differ for their biogeochemical characteristics and this factor affects the biological activity. Conservative tracers provide information about water transport and arrival time, but they have limitations in distinguishing the different stream

compartments. In recent years, improvements have been obtained by the development of a "smart" tracer technique, that includes some information about microbiological activity and sediment-water interactions. Haggerty et al. (2008) proposed the use of Resazurin (Raz, blue colour) as smart tracer, converted in Resorufin (Rru, fluorescent pink colour) under reducing conditions. The Raz-Rru system has been used by researchers to quantify parameters and fluxes related to water-sediment interface and metabolically active zone in aquatic ecosystems and at multiple scales. The application of Raz as tracer technique at the reach-scale is widely demonstrated by several studies, for example Argerich et al. (2011), Lemke, Liao, et al. (2013), González-Pinzón et al. (2014, 2015, 2016). Together with the new technique, adequate models have been developed for the estimation of parameters representing exchange between the surface and hyporheic zones, trying to define parameters for describing both physical and biochemical features of the zones. As for conservative tracer, these models optimize their parameters by calculation of the best fit between measured and simulated breakthrough curves. For example, Argerich et al. (2011) developed a model separating the transient storage in a metabolically active part and a metabolically inactive storage (MATS-MITS model). Lemke, Liao, et al. (2013) demonstrated that a joint fit of conservative and reactive tracer gives a different transport parameters estimation from that obtained by fitting conservative data, and they used a Markov chain Monte Carlo approach to avoid the problem of dependency by initial guess. Yakirevich et al. (2017) developed a STS-HTS model for smart tracers and compared it with a MATS-MITS model, finding a better fit bur uncertain results when STS-HTS calibrates all reaction parameters for all model compartments.

In the present study, the general framework used in STIR has been used as basis for implementing an innovative tool, STIR-RST, for the modelling of reactive smart tracers dataset. Moreover, in this version, the option of choosing between two arrangements were included: nested (in-series) or competing (in-parallel) storage zones. The new software tool was applied to experimental concentration curves obtained in a field campaign.

5.2 Model

5.2.1 Time domain formulation

The transport of a solute along a river channel is represented as a stochastic process involving the motion of a large number of solute “particles”. To derive the fundamental model equations, we initially assume that the transport within the main flow channel (MFC) is affected by trapping in a single storage zone (SZ), and later extend the theory to the case of

multiple storage zones. We assume that any significant streamwise transport occurs only in the MFC and represent the storage zone as an immobile domain.

Resazurin (Raz) is transformed into Resorufin (Rru) according to a first-order reaction with constant kinetic rate λ_{W12} in the main channel, and λ_{S12} in the storage zones. For sake of generality, we also consider the potential decay of the solute according to first-order kinetics with decay rates λ_{W1} and λ_{S1} for Resazurin, and λ_{W2} and λ_{S2} for Resorufin, where the subscript W and S are associated with the MFC and the SZ, respectively, and numbers refer to the tracer type.

Let $\psi_C(x,t)\,dx$ be the probability that a particle of passive solute has traveled a distance between x and $x+dx$ in a time t knowing that the particle has never been trapped in the SZ. The probability density that a particle of Resazurin never trapped in the SZ has travelled a distance x without undergoing chemical transformations is:

$$\psi_C(x,t)e^{-(\lambda_{W1}+\lambda_{W12})t} \tag{5.1}$$

where $e^{-(\lambda_{W1}+\lambda_{W12})t}$ is the survival probability. The function ψ_C is referred to as the probability density function (PDF), or distribution, of jump length or traveled distance in the MFC.

Every time a particle is trapped in the SZ, the residence time in the SZ is assumed to be distributed according to the PDF $\varphi(t)$. Assuming that the residence times associated with different trapping events are conditionally independent, the overall residence time distribution in the SZ for a particle trapped n times along the MFC is:

$$\varphi^{*n}(t) = \underbrace{\varphi(t) * \varphi(t) * \ldots * \varphi(t)}_{\text{n times}} \tag{5.2}$$

where the symbol $*$ denotes convolution:

$$\varphi(t) * \varphi(t) = \int_0^t \varphi(\tau)\varphi(t-\tau)\,d\tau \tag{5.3}$$

The probability density that a Resazurin particle trapped in a storage zone is released from the storage zone after a time t without undergoing chemical transformations is therefore:

$$\varphi^{*n}(t)e^{-(\lambda_{S1}+\lambda_{S12})t} \tag{5.4}$$

Let $p(n|t)$ be the conditional probability that a particle is trapped n times in the SZ knowing that the particle has spent a time t in the MFC. The probability of a Resazurin particle travelling a distance x within a time t without chemically reacting is therefore:

$$\psi_{Raz}(x,t) = \sum_{n=0}^{\infty} \int_0^t \psi_C(x,\tau) e^{-(\lambda_{W1}+\lambda_{W12})\tau}\, p(n|\tau)\, \varphi^{*n}(t-\tau) e^{-(\lambda_{S1}+\lambda_{S12})(t-\tau)}\, d\tau \quad (5.5)$$

If the probability that a particle is trapped along the MFC is spatially uniform and constant in time, and if the trapping events are conditionally independent, the probability $p(n|t)$ is described by the Poisson distribution (*Marion et al., 2008*):

$$p(n|t) = \frac{(\alpha t)^n e^{\alpha t}}{n!} \quad (5.6)$$

where α is the trapping probability per unit time, equivalent to a transfer rate.

We assume that the hydrodynamic processes affecting the transport of Resorufin are the same as for Resazurin, but the chemical transformations are different. Following similar derivations as those presented above, the probability that a particle of Resorufin travels a distance x in a time t without chemical transformation is:

$$\psi^{\dagger}_{Rru}(x,t) = \sum_{n=0}^{\infty} \int_0^t \psi_C(x,\tau) e^{-\lambda_{W2}\tau}\, p(n|\tau)\, \varphi^{*n}(t-\tau) e^{-\lambda_{S2}(t-\tau)}\, d\tau \quad (5.7)$$

The probability density per unit time that a particle of Resorufin is generated in the MFC at position x at time t is:

$$g_W(x,t) = \lambda_{W12}\psi_{Raz}(x,t) \quad (5.8)$$

which is then transported according to equation (5.7). The probability density that a particle of Resazurin is transformed into Resorufin after spending a time t in the SZ is:

$$\lambda_{S12} e^{-\lambda_{S12}t} \quad (5.9)$$

Therefore, if different decay rates are considered for Resazurin and Resorufin, the probability of particle of Resazurin exiting the SZ as Resorufin at position x after spending a time t in a storage zone is:

$$\varphi(t) \int_0^t \lambda_{S12} e^{-\lambda_{S12}\tau} e^{-\lambda_{S1}\tau} e^{-\lambda_{S2}(t-\tau)} d\tau = \varphi(t) \frac{\lambda_{S12}\left(e^{-\lambda_{S2}t} - e^{-(\lambda_{S1}+\lambda_{S12})t}\right)}{\lambda_{S1}+\lambda_{S12}-\lambda_{S2}} \quad (5.10)$$

hence the generation of Resorufin per unit time at position x in the SZ time is:

$$g_S(x,t) = \alpha \int_0^t \varphi(\tau) \frac{\lambda_{S12}\left(e^{-(\lambda_{S1}+\lambda_{S12})\tau} - e^{-\lambda_{S2}\tau}\right)}{\lambda_{S1}+\lambda_{S12}-\lambda_{S2}} \psi_{Raz}(x, t-\tau) d\tau \quad (5.11)$$

Particles of Resorufin generated in the MFC and in the SZ are transported according to (5.7), hence:

$$\psi_{Rru}(x,t) = \int_0^t \int_{-\infty}^{\infty} (g_W(\xi,\tau) + g_S(\xi,\tau))\psi_{Rru}^{\dagger}(x-\xi, t-\tau)d\xi\, d\tau \qquad (5.12)$$

For a mass injection rate of Resazurin $\dot{M}_{Raz}(t)$ at point $x = 0$, the concentrations of Resazurin, C_{Raz}, and Resorufin, C_{Rru}, are respectively given by:

$$C_{Raz}(x,t) = \frac{1}{A}\int_0^t \dot{M}_{Raz}(\tau)\psi_{Raz}(x, t-\tau)\, d\tau \qquad (5.13)$$

$$C_{Rru}(x,t) = \frac{1}{A}\int_0^t \dot{M}_{Raz}(\tau)\psi_{Rru}(x, t-\tau)\, d\tau \qquad (5.14)$$

Alternatively, for a concentration of Resazurin specified at the upstream boundary, $C_{Raz,b}(t)$, one needs to look at the probability that a solute particle originally at the boundary travels a distance x in a time between t and $t + dt$. This is referred to as transit time probability or residence time probability. Indicating with $r_C(x,t)$ the transit time PDF for a segment of the MFC of length x in the absence of storage and reactions, and with $r_{Raz}(x,t)$ the transit time PDF for Resazurin, the expression for $r_{Raz}(x,t)$ is still given by (5.5), but with ψ_C now replaced by r_C. Similarly, if the transit time PDF for Resorufin is denoted by r_{Rru}, and $r_{Rru}^{\dagger}$ is the transit time PDF counterpart of $\psi_{Rru}^{\dagger}$ obtained by replacing ψ_C with r_C in (5.7) then r_{Rru} is given by (5.12) with $\psi_{Rru}^{\dagger}$ replaced by $r_{Rru}^{\dagger}$. The concentrations $C_{Raz}(x,t)$ and $C_{Rru}(x,t)$ can now be expressed as follows:

$$C_{Raz}(x,t) = \int_0^t C_{Raz,b}(\tau)\, r_{Raz}(x, t-\tau)\, d\tau \qquad (5.15)$$

$$C_{Rru}(x,t) = \int_0^t C_{Raz,b}(\tau)\, r_{Rru}(x, t-\tau)\, d\tau \qquad (5.16)$$

As a special case, it can be assumed that the transport of a passive solute in the MFC is described by the advection-dispersion equation (ADE):

$$\frac{\partial C}{\partial x} + U\frac{\partial C}{\partial x} - D\frac{\partial^2 C}{\partial x^2} = 0 \qquad (5.17)$$

where C is concentration, U is flow velocity, D is the longitudinal dispersion coefficient. The ADE implies that the distribution of jump length is

$$\psi_C(x,t) = \frac{1}{2\sqrt{\pi D t}}\, e^{-\frac{(x-Ut)^2}{4Dt}} \qquad (5.18)$$

and the transit time distribution is

$$r_C(x,t) = \frac{x}{2\sqrt{\pi D t^3}} e^{-\frac{(x-Ut)^2}{4Dt}} \quad (5.19)$$

If the storage zone has finite cross sectional area, A_S, and the interfacial transfer rate, α, is constant, the residence time follows an exponential distribution,

$$\varphi(t) = \frac{1}{T} e^{-t/T} \quad (5.20)$$

where $T = \alpha A / A_S$ is the average residence time.

5.2.2 Laplace domain formulation

The evaluation of the convolution integrals that appear in the time domain formulation can be simplified by using Laplace transform (LT). The LT of a function $\varphi(t)$ is defined as:

$$\tilde{\varphi}(s) = \int_0^\infty \varphi(t)\, e^{-st}\, dt \quad (5.21)$$

where s is the Laplace variable. Using the convolution theorem, the LT of (5.5) can be written as:

$$\tilde{\psi}_{Raz}(x,s) = \sum_{n=0}^{\infty} \left(\int_0^\infty \psi_C(x,t) e^{-(\lambda_{W1}+\lambda_{W12})t}\, p(n|t) e^{-st}\, dt \right) \tilde{\varphi}^n(s+\lambda_{S1}+\lambda_{S12}) \quad (5.22)$$

If the trapping probability follows a Poisson distribution, combining (5.6) with (5.22) gives:

$$\tilde{\psi}_{Raz}(x,s) = \sum_{n=0}^{\infty} \int_0^\infty \psi_C(x,t)\, \frac{[\alpha\tilde{\varphi}(s+\lambda_{S1}+\lambda_{S12})t]^n}{n!} e^{-(s+\lambda_{W1}+\lambda_{W12}-\alpha)t}\, dt \quad (5.23)$$

By using the identity

$$\frac{[\alpha\varphi(s+\lambda_{S1}+\lambda_{s12})t]^n}{n!} = e^{\alpha\tilde{\varphi}(s+\lambda_{S1}+\lambda_{S12})t} \quad (5.24)$$

and the shifting theorem of Laplace transforms, equation (5.24) gives:

$$\begin{aligned} \tilde{\psi}_{Raz}(x,s) &= \tilde{\psi}_C(x, s+\lambda_{W1}+\lambda_{W12}+\alpha(1-\tilde{\varphi}(s+\lambda_{S1}+\lambda_{S12}))) \\ &= \tilde{\psi}_C(x, \nu_{Raz}(s)) \end{aligned} \quad (5.25)$$

where

$$\nu_{Raz}(s) = s+\lambda_{W1}+\lambda_{W12}+\alpha(1-\tilde{\varphi}(s+\lambda_{S1}+\lambda_{S12})) \quad (5.26)$$

is a frequency variable. Similarly, the LT of $\psi^\dagger_{Rru}(x,t)$ can be written as:

$$\begin{aligned} \tilde{\psi}^\dagger_{Rru}(x,s) &= \tilde{\psi}_C(x, s+\lambda_{W2}+\alpha(1-\tilde{\varphi}(s+\lambda_{S2}))) \\ &= \tilde{\psi}_C(x, \nu_{Rru}(s)) \end{aligned} \quad (5.27)$$

where

$$\nu_{Rru}(s) = s + \lambda_{W2} + \alpha(1 - \tilde{\varphi}(s + \lambda_{S2})) \quad (5.28)$$

The LTs of the generation functions g_W and g_S are:

$$\tilde{g}_W(s) = \lambda_{W12}\tilde{\psi}_{Raz}(x, s) \quad (5.29)$$

and

$$\tilde{g}_S(x, s) = \alpha\frac{\tilde{\varphi}(s + \lambda_{S2}) - \tilde{\varphi}(s + \lambda_{S1} + \lambda_{S12})}{\lambda_{S1} + \lambda_{S12} - \lambda_{S2}}\tilde{\psi}_{Raz}(x, s) \quad (5.30)$$

respectively. Hence:

$$\begin{aligned}\tilde{\psi}_{Rru}(x, s) &= \left[\lambda_{W12} + \alpha\frac{\tilde{\varphi}(s+\lambda_{S2}) - \tilde{\varphi}(s+\lambda_{S1}+\lambda_{S12})}{\lambda_{S1}+\lambda_{S12}-\lambda_{S2}}\right]\int_{-\infty}^{\infty}\tilde{\psi}_{Raz}(\xi, s)\tilde{\psi}^{\dagger}_{Rru}(x - \xi, s)\, d\xi \\ &= \left[\lambda_{W12} + \alpha\frac{\tilde{\varphi}(s+\lambda_{S2}) - \tilde{\varphi}(s+\lambda_{S1}+\lambda_{S12})}{\lambda_{S1}+\lambda_{S12}-\lambda_{S2}}\right]\int_{-\infty}^{\infty}\tilde{\psi}_{C}(\xi, \nu_{Raz}(s))\tilde{\psi}_{C}(x - \xi, \nu_{Rru}(s\end{aligned} \quad (5.31)$$

As a special case, if the distribution (5.18) resulting from the classic ADE is assumed to represent the transport in the MFC, and the exponential distribution (5.20) is assumed for the SZ, the LT of (5.5) and (5.12) are, respectively:

$$\tilde{\psi}_{Raz}(x, s) = \frac{e^{\frac{x\left(U - \sqrt{4D\nu_{Raz}(s) + U^2}\right)}{2D}}}{\sqrt{4D\nu_{Raz}(s) + U^2}} \quad (5.32)$$

$$\begin{aligned}&\tilde{\psi}_{Rru}(x, s) \\ &= \left[\lambda_{W12} + \alpha\frac{\lambda_{S12}T}{(1 + sT + (\lambda_{S1} + \lambda_{S12})T)(1 + sT + \lambda_{S2}T)}\right] \\ &\cdot\frac{\sqrt{4D\nu_{Raz}(s) + U^2}e^{\frac{x\left(U - \sqrt{4D\nu_{Rru}(s) + U^2}\right)}{2D}} - \sqrt{4D\nu_{Rru}(s) + U^2}e^{\frac{x\left(U - \sqrt{4D\nu_{Raz}(s) + U^2}\right)}{2k}}}{[\nu_{Raz}(s) - \nu_{Rru}(s)]\sqrt{4D\nu_{Raz}(s) + U^2}\sqrt{4D\nu_{Rru}(s) + U^2}}\end{aligned} \quad (5.33)$$

where:

$$\nu_{Raz}(s) = s + \lambda_{W1} + \lambda_{W12} + \alpha\left[1 - \frac{1}{1 + (s + \lambda_{S1} + \lambda_{S12})T}\right] \quad (5.34)$$

$$\nu_{Rru}(s) = s + \lambda_{W2} + \alpha\left[1 - \frac{1}{1 + (s + \lambda_{S2})T}\right] \quad (5.35)$$

5.2.3 Exchange with multiple storage zones

The model equations derived above can be easily extended to the case of multiple zones in parallel. The expression for $\tilde{\psi}_{Raz}$ remains the same (equation (5.25)) but now the frequency variable $\nu_{Raz}(s)$ is:

$$\nu_{Raz}(s) = s + \lambda_{W1} + \lambda_{W12} + \sum_{i=0}^{N_S} \alpha_i (1 - \tilde{\varphi}_i(s + \lambda_{S1,i} + \lambda_{S12,i})) \quad (5.36)$$

where N_S is the number of storage zones. Taking into account the generation of Resorufin in the SZs, the expression for $\tilde{\psi}_{Rru}$ becomes:

$$\tilde{\psi}_{Rru}(x,s) = \left[\lambda_{W12} + \sum_{i=0}^{N_S} \alpha_i \frac{\tilde{\varphi}_i(s + \lambda_{S2,i}) - \tilde{\varphi}_i(s + \lambda_{S1,i} + \lambda_{S12,i})}{\lambda_{S1,i} + \lambda_{S12,i} - \lambda_{S2,i}}\right] \cdot \int_{-\infty}^{\infty} \tilde{\psi}_C(\xi, \nu_{Raz}(s)) \tilde{\psi}_C(x - \xi, \nu_{Rru}(s))\, d\xi \quad (5.37)$$

where:

$$\nu_{Rru}(s) = s + \lambda_{W2} + \sum_{i=0}^{N_S} \alpha_i (1 - \varphi_i(s + \lambda_{S2,i})) \quad (5.38)$$

Alternatively, we can consider the case of two storage zones in series, with the transfer rate α_2 representing the probability per unit time that a solute particle in the first SZ (denoted with the subscript 1 in the derivations that follow) can be trapped in the second SZ (denoted with the subscript 2). Similar considerations to those presented above for the exchange between the MFC and the SZ now apply to the exchange between the first and the second SZ. The PDF $\tilde{\psi}_{Raz}(x,s)$ is still given by (5.25), but now the frequency variable $\nu_{Raz}(s)$ is:

$$\nu_{Raz}(s) = s + \lambda_{W1} + \lambda_{W12} + \alpha_1 (1 - \varphi_1(\nu_{Raz,1}(s)) \quad (5.39)$$

where:

$$\nu_{Raz,1}(s) = s + \lambda_{S1,1} + \lambda_{S12,1} + \alpha_2 (1 - \tilde{\varphi}_2(s + \lambda_{S1,2} + \lambda_{S12,2})) \quad (5.40)$$

By modelling the exchange between the first and the second SZ in the same way as the exchange between the MFC and the SZ, we obtain:

$$\tilde{g}_S(s) = \left[\lambda_{S12,1} + \alpha_2 \frac{\tilde{\varphi}_2(s + \lambda_{S2,2}) - \tilde{\varphi}_2(s + \lambda_{S1,2} + \lambda_{S12,2})}{\lambda_{S1,2} + \lambda_{S12,2} - \lambda_{S2,2}}\right] \tilde{\varphi}_1(\nu_{Rra,1}(s)) \tilde{\varphi}_1(\nu_{Rru,1}(s)) \quad (5.41)$$

and

$$\tilde{\psi}_{Rru}(x,s) = [\lambda_{W12} + \tilde{g}_S(s)] \int_{-\infty}^{\infty} \tilde{\psi}_C(\xi, \nu_{Raz}(s)) \tilde{\psi}_C(x - \xi, \nu_{Rru}(s))\, d\xi \quad (5.42)$$

where:

$$\nu_{Rru}(s) = s + \lambda_{W2} + \alpha_1 (1 - \varphi_1(\nu_{Rru,1}(s)) \quad (5.43)$$

$$\nu_{Rru,1}(s) = s + \lambda_{S2,1} + \alpha_2(1 - \tilde{\varphi}_2(s + \lambda_{S2,2})) \quad (5.44)$$

5.3 The STIR-RST software

The stochastic formulation presented above represents a general modelling framework in which different storage processes can be represented by specific residence time distributions. The residence time formulation presented above has been implemented in a Matlab code which is released under the name STIR-RST, an acronym for "Solute Transport In Rivers – Reactive Smart Tracer". The software STIR-RST is provided as a particular implementation of the residence time formulation presented above that considers the exchange with two distinct storage zones, each characterized by an exponential residence time distribution, whereas the transport in the MFC in the absence of storage is represented by the classic advection-dispersion equation.

The class file *StirST2ExpModel* included in the software can be used as a starting basis to implement alternative versions of the model where storage processes are represented by different residence time distributions. This requires that the corresponding Laplace transform is provided as a separate Matlab function, and that the model class file is modified to handle the relevant input parameters. The simulation parameters can be read from an XML file or entered from the command line or Matlab script. A template input file for the two-exponential RTD model is provided with the software and includes a description for each of the parameters. Running the model and visualizing the results involves the following sequence of instructions:

```
model = StirST2ExpModel();
model.read('templates/StirST2ExpModel.xml');
model.run();
model.plot();
```

The software also allows for data calibration using a range of optimization methods for local and global optimization, including the Nelder-Mead method, simulated annealing, particle swarm, pattern search, and differential evolution. After loading the concentration data in the Matlab workspace, the model can be calibrated with the instruction

```
model.calibrate()
```

An example script for model calibration using smart tracer data is provided with the software. It is possible to define which model parameters should be calibrated and their range of variation by modifying an additional file containing the calibration settings. After calibration, the parameter valued can then be listed on screen,

model.printParameters()

or saved to an XML file:

model.write('output.xml')

The user can choose between calibration in linear, logarithmic and mixed scale. In the case of linear scale calibration, the root mean square error (RMSE) is calculated as:

$$\mathrm{RMSE} = \sqrt{\frac{1}{N_{\mathrm{obs}}} \sum_{j=1}^{N_{\mathrm{obs}}} \frac{(C_j - C_{\mathrm{obs},j})^2}{(C_{\mathrm{obs,max}} - C_{\mathrm{obs,min}})^2}} \quad (5.45)$$

where C_j are the simulated concentration values, $C_{\mathrm{obs},j}$ are the observations, $C_{\mathrm{obs,max}}$ is the maximum observed concentration value, and $C_{\mathrm{obs,min}}$ is the minimum observed value. For logarithmic scale,

$$\mathrm{RMSE} = \sqrt{\frac{1}{N_{\mathrm{obs}}} \sum_{j=1}^{N_{\mathrm{obs}}} \frac{(\log C_j - \log C_{\mathrm{obs},j})^2}{(\log C_{\mathrm{obs,max}} - \log C_{\mathrm{obs,min}})^2}} \quad (5.46)$$

where $C_{\mathrm{obs,min}}$ is the minimum observed concentration. In the application of (5.46) the STIR-RST software allows to exclude the lowest percentile of the observed concentrations. The default value is 5%, but can be modified from the software calibration options. For mixed scale, we use the same definition proposed by Bottacin-Busolin et al. (2011):

$$\mathrm{RMSE} = \sqrt{\frac{1}{N_{\mathrm{obs}}} \left(\sum_{j \in I_U} \frac{(C_j - C_{\mathrm{obs},j})^2}{(C_{\mathrm{obs,max}} - C_{\mathrm{obs,min}})^2} + \sum_{j \in I_L} \frac{(\log C_j - \log C_{\mathrm{obs},j})^2}{(\log C_{\mathrm{obs,max}} - \log C_{\mathrm{obs,min}})^2} \right)} \quad (5.47)$$

where I_U and I_L are the sets of observed values respectively higher and lower than a threshold concentration. The threshold value is defined in the STIR-RST software as a percentage of the peak concentration. The default value of the threshold is 20%, but can be modified from the calibration options. As for the logarithmic scale calibration, the expression (5.47) is applied by excluding a given percentage of the lowest concentrations.

For smart tracer studies, the Resazurin and Resorufin breakthrough curves are fit simultaneously by extending the summation in the above definitions of the RMSE to the observed concentrations of resazuin and Resorufin. Optionally, the software allows to simultaneously fit breakthrough curves from a conventional tracer and a smart tracer.

5.3.1 STIR-RST Parameters

In Table 5.1, the complete list of parameters in STIR-RST. Some of them are input parameters: injected mass M_{con} and/or M_{raz}, injection duration $T_{con,inj}$ and/or $T_{raz,inj}$, reach length L. It is suggested to measure cross-sectional area A and flow rates Q and to include them as input data in order to reduce the number of parameters to be calibrated.

Table 5.1. Parameters in STIR-RST model

Symbol	Description	*Units*
A	Channel cross-sectional area	m^2
D	Dispersion coefficient	$m^2 s^{-1}$
$d_{con,f}$	Dilution factor for the conservative tracer	-
$d_{Raz,f}$	Dilution factor for the smart tracer	-
L	Reach Length	m
M_{con} *	Injected mass for the conservative tracer	$g; mol$
M_{Raz} *	Injected mass for the smart tracer	$g; mol$
Q	Flow rate	$m^3 s^{-1}$
Q_L	Flow rate for the lateral inflow	$m^3 s^{-1}$
$\lambda_{W0,}\lambda_{W1},\lambda_{W2}$	Decay rates for conservative tracer (0), Raz (1), Rru (2) in the main channel	s^{-1}
$\lambda_{S0,1}$, $\lambda_{S1,1},\lambda_{S2,1}$	Decay rates for conservative tracer (0), Raz (1), Rru (2) in the Storage zone #1	s^{-1}
$\lambda_{S0,2}$, $\lambda_{S1,2},\lambda_{S2,2}$	Decay rates for conservative tracer (0), Raz (1), Rru (2) in the Storage zone #2	s^{-1}
λ_{W12} , $\lambda_{S12,1},\lambda_{S12,2}$	Transformation rates from Raz to Rru (12) in: main channel (W), Storage zone #1 (S12,1), Storage zone #2 (S12,2)	s^{-1}
T_1	Mean residence time for the storage zone #1	s
T_2	Mean residence time for the storage zone #2	s
$T_{con,inj}$	Injection duration for the conservative tracer	s
$T_{Raz,inj}$	Injection duration for the smart tracer (here Resazurin)	s
α_1	Exchange rate between storage zone #1 and MFC	s^{-1}
α_2	Exchange rate between storage zone #2 and MFC (for in parallel arrangement) or storage zone #2 and storage zone #1 (for in series arrangement)	s^{-1}

Note. * It is possible to use several units for mass, and input concentrations have to be consistent with mass and discharge units.

5.4 Applications: experimental test case

In this section a test case of STIR-RST is reported, where the model parameters were fitted to experimental data obtained from a field smart tracer test, considering two different arrangements of the storage zones (in series and in parallel).

5.4.1 Experimental test

The study site for the experimental tests was located in the countryside just outside the urban settlement of Monselice (Padua, Italy). The field experiments were carried in the Desturo canal, a small drainage canal, about 6 km long, used for irrigation purposes. The canal was affected by pollution due to distributed inputs of fertilizers used in the agricultural activity, of waters from a waste-water treatment plant and of non-treated water during rain periods from urban drainage systems. The study reach was located downstream the outlet point of the treatment plant for a total length of 220 m. The injection point (I0) was chosen just downstream that outlet point in order to ensure fast well-mixed condition for the injected tracer. Two measurement stations (St1 and St2) were placed at distances L_{01}=130 m and L_{02}=220 m from I0, respectively. From here on, we refer to the reach from I0 to St1 as R01, from I0 to St2 as R02, and from St1 toSt2 as R12. Sandy-silty material characterized the whole study reach and the bed presented submerged vegetation, mostly along R12. The canal in reach R01 presented an initial straight constant-width part, then an almost 90° bend with an enlarged section, and finally returned to almost the initial width. Vegetation on the banks was quite thin along R01, with few short portions in concrete or rocks. Reach 12 was characterized by almost straight path, with much more vegetation along the banks and the bed. Map of the study site and the location of the measurement stations are given in Figure 5.1, and some pictures taken along the study reach are shown in Figure 5.2.

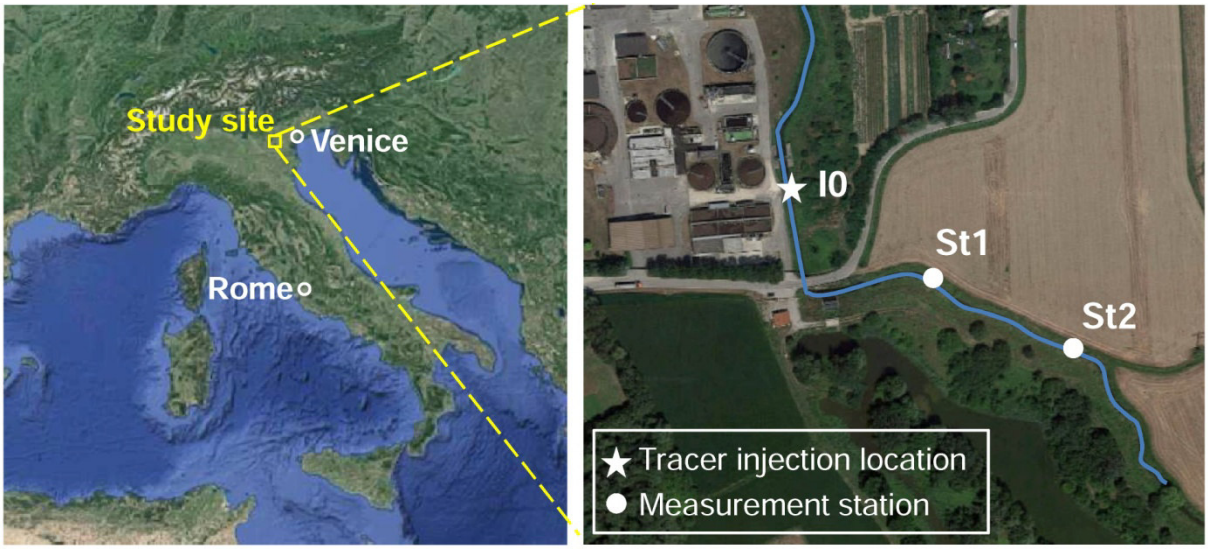

Figure 5.1 Study area in Monselice (Padua, Italy) and location of study sections along Desturo Canal downstream the treatment plant.

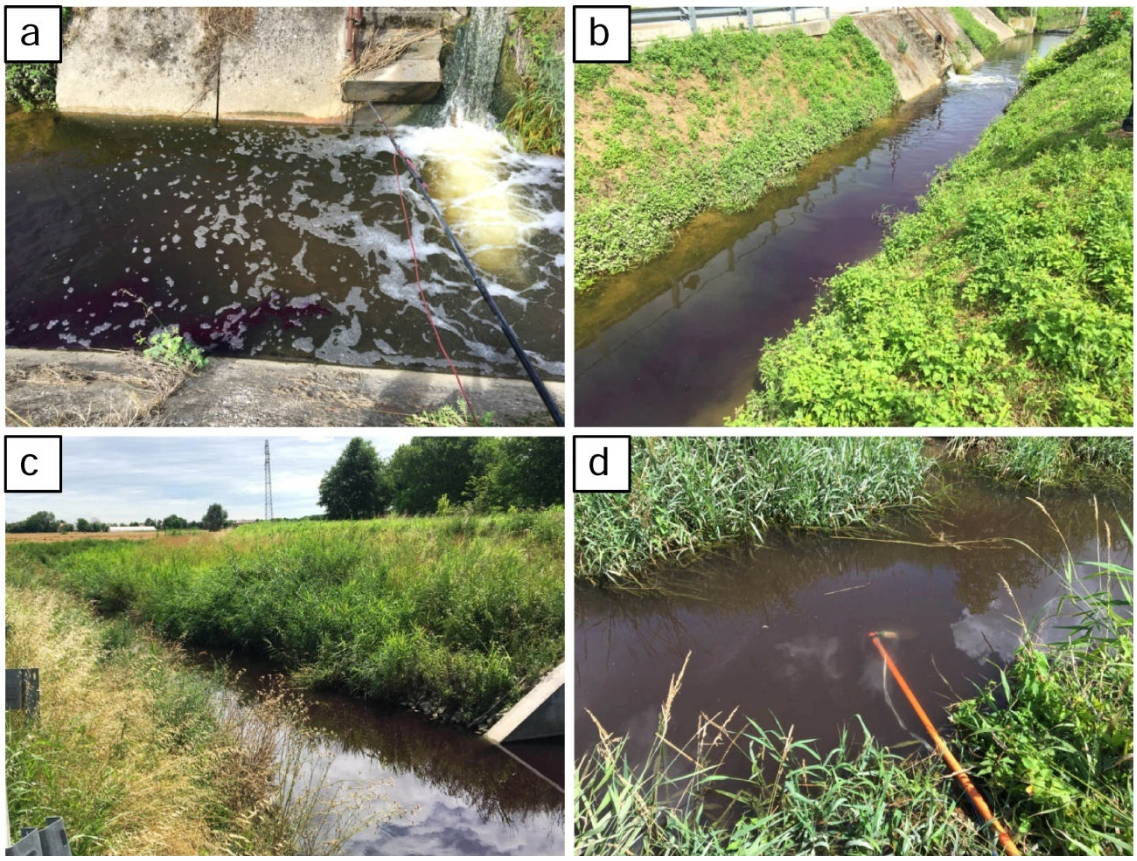

Figure 5.2 Canal characteristics along the study reach: a) station S0 and release of tracer downstream the outlet of the treatment plant; b) along reach R01, in its straight part, with quite cleaned banks and bed; c) after the bend of R01, and initial part of reach R12 (more vegetated); d) measurement station S2; submerged vegetation is visible along the river side.

The tracer test was carried in June 2018. It consisted of a continuous (step) injection of Raz solution at high concentration at station S0, using a peristaltic pump ensuring a constant rate of input for the injection duration (Figure 5.2a). The flow rate Q measured with a current meter was almost steady at 0.54 m^3s^{-1}. We determined an averaged cross-sectional area A_{01}=1.18 m^2 for reach R01 and A_{02}=0.93 m^2 for reach R02. The injection duration $T_{Raz,inj}$ was 1320 s (22 minutes), and total Raz mass injected $M_{Raz,inj}$ was 14.30 g (0.057 mol).

At the two stations St1 and St2 intensity fluorescence signals were recorded using two GGUN-FL30 on-line fluorometers (Albilia sarl, Switzerland), at a sampling rate of 20 s, for about 4 hours. This fluorometer is a flow-through instrument allowing simultaneous detection of three tracers, and measurements of turbidity and water temperature. Recorded intensity signals were converted into dye concentration values, based on calibrations of instruments and using manufacturer's software. Two breakthrough curves were obtained at each station, representing Raz and Rru concentrations over time. The use of on-line fluorometer allowed to have a high resolution dataset over several hours. In Figure 5.3 the concentration is expressed in [mol*10^{-3} m^3] and they are shown both in linear and semi-log scale, the latter to expand the

tail behaviour that is representative of retention processes. Passing from St1 to St2, the decrease of Raz peak concentration is apparent and so is the little increase of the peak value for Rru, and the extended tail of Rru at section St2. This suggests that retention processes are more effective in the reach R12 (downstream St1), affecting results of reach R02 that exhibits longer tail and higher Rru production.

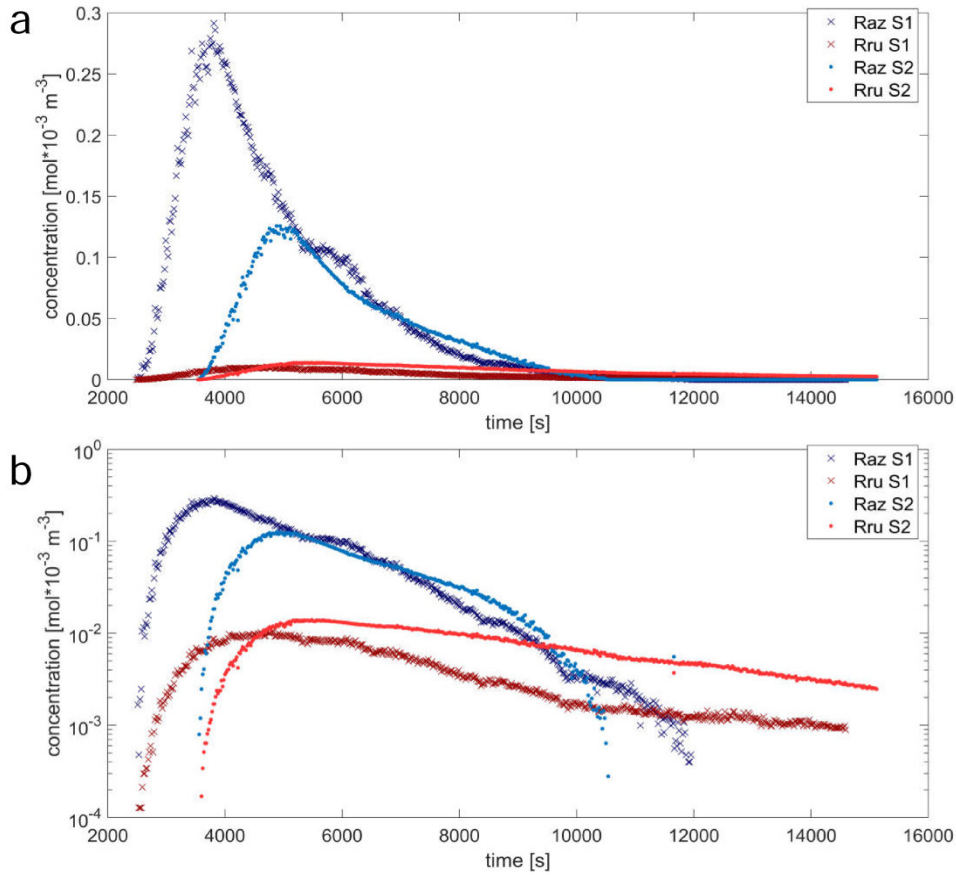

Figure 5.3 Concentration curves measured at the two stations S1 and S2, for Raz (blue shades) and Rru (red shades): in linear scale in panel a), in semi-log scale in panel b).

5.4.2 STIR-RST modelling

In this application, STIR-RST was used in its 2-storage-zone version adopting exponential residence time distribution. Measured data were used in STIR-RST for calibrating unknown parameters representing transport and retention properties. In particular, measured inputs were: concentrations of Raz and Rru in the time at sections St1 and St2, injection duration $T_{Raz,inj} = 1320\ s$, injected Raz mass $M_{Raz,inj} = 0.057\ mol$, flow rate $Q = 0.054\ m^3 s^{-1}$, averaged cross-sectional areas $A_{01} = 1.18\ m^2$ for reach R01 and $A_{02} = 0.93\ m^2$ for reach R02, reach lengths $L_{01} = 130\ m$ for reach R01 and $L_{02} = 220\ m$ for reach R02. Calibrated parameters were: the diffusive coefficient D, the exchange rates α_1 and α_2; the mean residence times T_1 and T_2, the rates describing Raz decay, Raz to Rru

transformation, Rru decay in main channel: $\lambda_{W1}, \lambda_{W12}, \lambda_{W2}$; the rates describing Raz decay, Raz to Rru transformation, Rru decay in the first storage zone: $\lambda_{S1,1}, \lambda_{S12,1}, \lambda_{S2,1}$; the rates describing Raz decay, Raz to Rru transformation, Rru decay in the second storage zone: $\lambda_{S1,2}, \lambda_{S2,2}, \lambda_{S12,2}$

For both reaches, first calibration was made using the Particle Swarm optimization method, then several runs were performed with a mixed-scale (linear and logarithmic) Nelder&Mead optimization method.

5.5 Results and Discussion

In Figure 5.4 calculated and measured concentration curves are presented, and in Table 5.2 calibrated parameter values are reported. Looking at the plots, in general a good fit is achieved for both sections and both tracers. In section St1 the calculated curve of Raz couldn't fit a little 'hump' present in the decreasing part of the curve, after the peak, at about 6000 s. In section St2 there is a poorer fit for Raz curve around about 8000 s, where the calculated curve decreases faster than the measured one. Section St1 is characterized by a better fitting than section St2, and this is expressed by a lower value of RMSE, estimated according to (5.47). In this application, the fitting quality is similar for in-series and in-parallel arrangements, with best fit values not significantly different and practically overlapping calculated curves.

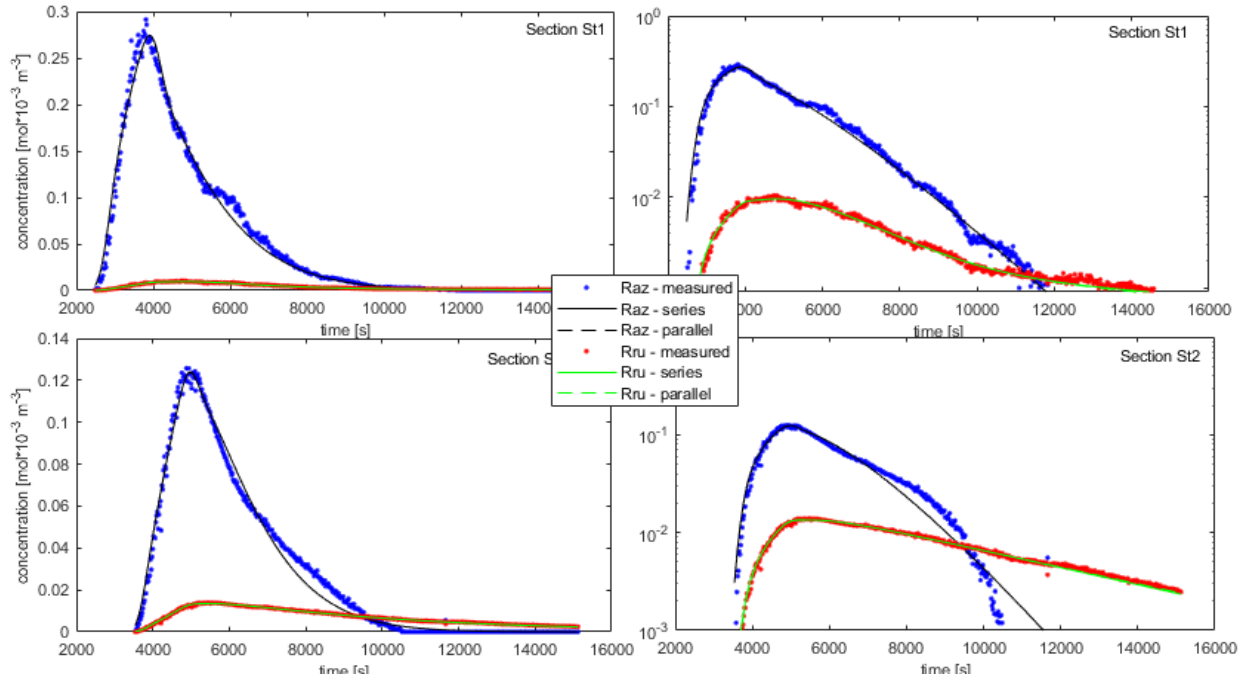

Figure 5.4. Breakthrough curves fitting comparisons of in-series (solid line) and in-parallel (dashed lines) arrangements, for both Raz and Rru. Fitting are showed in linear an logarithmic scales (on left and right plots respectively), for section S1 in the first row and section S2 in the second row.

Dispersion coefficients have similar values, about 0.016 and 0.014 $m^2 s^{-1}$ for section St1 and St2 respectively. In the presented model, where transient storage is represented by two exponential RTDs, mass exchange can be conceptually separated in a fast component associated to surface dead zones and a slow component typically associated to hyporheic zones. Having the two RTDs the same functional form, it is possible to directly compare the timescale parameter, T_i, that represents s the mean residence time for an exponential PDF.

Looking at values in Table 5.2, exchange rates α_i and retention times T_i have similar order of magnitude for section St1 and St2, comparing the same storage zone *i*. For both sections, the transfer rates α_1 associated to the shorter timescale retention component are significantly different from the transfer rate α_2 associated to the longer one. This seems more evident in the parallel arrangement where α_1 and α_2 differ of about one order of magnitude, for both sections. Almost an order of magnitude also characterizes the difference between $T_1$and T_2, for both arrangements and sections, and the higher values of T_2 can be associated to a significant second transient storage component. This is more evident for the first reach R01, where $\frac{T_2}{T_1} = 9.8 \div 11$, and the semi-log plot of Resorufin exhibits a bend and two slopes in the tail. For reach R02 the ratio $\frac{T_2}{T_1} = 4.9 \div 6.8$ indicates that the two storage zones are still present but with a less evident differentiation in the retention time scales than in R01, due to smaller T_2. The hyporheic flows, typically associated to high T_2, could be inhibited by bottom vegetation covering the second part of reach R02 (that is R12).

Focusing on the transformation rates of the smart tracer (highlighted in Table 5.2), a first consideration can be made looking at the "j" zones (main channel MFC, surface storage zone SZ1, deeper storage zone SZ2). For both sections and both arrangements, λ_{j12} increases from MFC to SZ1 to SZ2 of at least one order of magnitude ($\lambda_{W12} < \lambda_{S12,1} < \lambda_{S12,2}$), showing that conversion of Raz to Rru mostly happens in the storage zones, and in particular in the #2 (the slow retention zone). At least one order of magnitude also characterizes the increase of all rates λ_{j12} from section St1 to section St2. This is probably due to the fact that the final part of R02 (that is reach R12) is highly vegetated and with a less regular bed than reach R01, leading to a higher biological activity both in the main flow channel and in the two retention zones. These values suggest how the use of smart tracer allows characterizing the different river compartments not only based on physical transport mechanisms but also on the different biochemical features.

Decay rates of Raz for section St1, and both arrangements, are very small in zone MFC, λ_{W1}, and SZ1, $\lambda_{S1,1}$, and present much higher value in SZ2, $\lambda_{S1,2}$ (at least 7 order of

magnitude greater). For section St2 instead, these decay rates differ both from St1 values and between in-series and in-parallel structure: for St2_s the highest value is λ_{W1}=6.4×10^{-5} s^{-1} in MFC, for St2_p the highest rate is $\lambda_{S1,2}$=5.8×10^{-3} s^{-1} in SZ2. Decay rates of Rru are very small in MFC, λ_{W2} and in storage SZ2, $\lambda_{S2,2}$, and show the highest values in SZ1, $\lambda_{S2,1}$, for both sections and arrangements.

Table 5.2. Calibrated parameters. Highlighted rows refers to Raz-to-Rru transformations rates.

Section	St1		St2	
run arrangement	St1_s in series	St1_p in parallel	St2_s in series	St2_p in parallel
RMSE	0.0457	0.0458	0.0613	0.0612
A [m^2]	1.18	1.18	0.93	0.93
Q [m^3 s^{-1}]	0.054	0.054	0.054	0.054
D [m^2 s^{-1}]	0.01607	0.01612	0.01410	0.01454
α_1 [×10^{-4} s^{-1}]	7.04	6.12	8.25	6.15
T_1 [×10^3 s]	1.00	0.87	0.85	0.65
α_2 [×10^{-4} s^{-1}]	2.43	0.93	3.46	0.96
T_2 [×10^3 s]	9.80	9.80	4.17	4.44
λ_{W1} [×10^{-6} s^{-1}]	0.0015	0.00099	63.8	179
λ_{W12} [×10^{-6} s^{-1}]	6.8	6.6	17.7	12.3
λ_{W2} [×10^{-6} s^{-1}]	0.0016	0.0039	0.0056	0.53
$\lambda_{S1,1}$ [×10^{-6} s^{-1}]	0.046	0.0054	0.017	1.95
$\lambda_{S12,1}$ [×10^{-6} s^{-1}]	37.0	35.4	123	44.3
$\lambda_{S2,1}$ [×10^{-6} s^{-1}]	204	225	1810	3510
$\lambda_{S1,2}$ [×10^{-6} s^{-1}]	13000	21100	0.0094	5760
$\lambda_{S12,2}$ [×10^{-6} s^{-1}]	619	1050	2530	24500
$\lambda_{S2,2}$ [×10^{-6} s^{-1}]	0.0000011	0.0000086	0.00087	0.80

Total mass recovered M at the two sections is calculated for each breakthrough curve as:

$$M_{tracer} = Q * \int_{t_i}^{t_f} C_{tracer}(t)dt \qquad (5.48)$$

where $tracer$ represents either Raz, Rru or their summation (referred to as Tot), t_i is the initial measurement time, t_f is the final measurement time, and the integral represents the zero-th moment of the breakthrough curve. The results are summarized in Table 5.3. For section St1, for the measured dataset the recovered total mass M_{tot} is about 68.29% of the injected mass $M_{Raz,inj}$. The calculated datasets underestimate this percentage of about 0.6%. For section St2, the measured total recovered mass is about 39.90%, with again a little underestimation for the calculated datasets (about 0.55% lower than the M_{tot} estimated for the measured dataset). In both section, Raz and Rru are lost in physical, chemical or biological processes, and this is taken into account by the decay rates $\lambda_{W1}, \lambda_{W2}, \lambda_{S1,1}, \lambda_{S2,1}, \lambda_{S1,2}, \lambda_{S2,2}$.

Table 5.3. Mass recovered

Section	St1			St2		
dataset	measured	calculated		measured	calculated	
arrangement	-	in series	in parallel	-	in series	in parallel
M^{Raz} [$\times 10^{-3}$ mol]	36.423	36.080	36.081	18.248	17.965	17.976
M^{Rru} [$\times 10^{-3}$ mol]	2.503	2.484	2.481	4.496	4.463	4.474
M^{Tot} [$\times 10^{-3}$ mol]	38.926	38.565	38.563	22.744	22.428	22.450
M^{Tot} $/M_{Raz,inj}$[%]	68.29%	67.66%	67.65%	39.90%	39.35%	39.38%

This experimental application of STIR-RST showed its capability of achieving a good quality in fitting measured breakthrough curves of smart tracers. It allows to calibrate several parameters useful for understanding the transport properties of the stream and the biological activity associated to different storage compartments. Although in this particular application both in-series and in-parallel arrangements showed a good fitting with physically reasonable parameters, the chance to have two different conceptual arrangements for the storage compartments allows the modeller to choose the one that, case by case, seems more adapt to describe the experimental dataset and the physical characteristics of the studied reach. In order to avoid uncertainty due to problems of parameter equifinality, it is suggested to independently determine some parameters (for example, measuring flow rate, area, reach length) and to perform an equivalent test using conservative tracer. This test would provide some parameter calibration (i.e., dispersion coefficient, exchange area, etc) thus reducing the number of calibration parameters of the smart tracer application.

5.6 Conclusions

Solute transport numerical models and tracers techniques represent well established methods for studying the transport of nutrients and pollutants in stream corridors. Usually, parameters for these models are calibrated using the datasets obtained by field tracer tests carried in the reach of interest. In recent years, tracer technique has been improved by the development of "smart" tracer technique, providing information about microbiological activity and sediment-water interactions.

In the present study, a new numerical tool has been presented for the modelling of solute transport and exchange processes taking place in open channel flows, focusing on a physical meaningful description of the different compartments (main flow channel and two storage zones). In particular, the general stochastic formulation used in STIR (Marion et al, 2008) has been the basic framework for implementing STIR-RST for the modelling of

reactive smart tracers breakthrough curves. The new model contains defined parameters for quantifying the decay and transformation rates of the tracers in the physical compartments. It also includes the option of choosing between two arrangements: nested (in-series) or competing (in-parallel) storage zones. An experimental field campaign has been carried out with the smart tracers combination Raz-Rru and the breakthrough curves of Raz and Rru have been used for an application of STIR-RST. In this application, the model has performed successfully for both arrangements, showing a good fit of all curves. The estimated parameters show values well corresponding with the physical features of the two reaches and with the expected biochemical characteristics. More precise estimates of model parameters could be achieved by the simultaneously injection of smart and conservative tracers, and the different model options could be further tested on reaches with different properties.

STIR-RST has therefore the potential to upgrade our understanding about solute transport processes in rivers and, in particular, to expand our knowledge about retention mechanisms and their physical and biological properties.

5.7 Acknowledgments

The authors thank Dr. Giovanni Marco Carrer (Environmental System Analysis Lab - LASA- of Department of Industrial Engineering, University of Padova) for his scientific and technical support in lab and field activities with smart tracers.

5.8 Bibliography

Argerich, A., Haggerty, R., Marti, E., Sabater, F., & Zarnetske, J. (2011). Quantification of metabolically active transient storage (MATS) in two reaches with contrasting transient storage and ecosystem respiration. Journal of Geophysical Research, 116, G03034. https://doi.org/ 10.1029/2010JG001379

Bencala, K. E., & Walters, R. A. (1983). Simulation of solute transport in a mountain pool-and-riffle stream—A transient storage model. Water Resources Research, 19(3), 718–724. https://doi.org/10.1029/WR019i003p00718

Boano, F., A. I. Packman, A. Cortis, R. Revelli, and L. Ridolfi (2007b), A continuous time random walk approach to the stream transport of solutes, *Water Resour. Res.*, 33, W10425, doi:10.1029/2007WR006062.

Bottacin-Busolin, A., A. Marion, T. Musner, M. Tregnaghi, and M. Zaramella (2011), Evidence of distinct contaminant transport patterns in rivers using tracer tests and a multiple domain retention model, *Adv. Water Resour.*, 34, 737– 746.

Briggs, M. A., M. N. Gooseff, C. D. Arp, and M. A. Baker (2009), A method for estimating surface transient storage parameters for streams with concurrent hyporheic storage, *Water Resour. Res.*, 45, W00D27, doi:10.1029/2008WR006959

Choi, J., J. W. Harvey, and M. H. Conklin (2000), Characterizing multiple timescales of stream and storage zone interaction that affect solute fate and transport in streams, *Water Resour. Res.*, 36, 1511– 1518, doi:10.1029/2000WR900051.

Deng, Z.-Q., L. Bengtsson, and V. P. Singh (2006), Parameter estimation for fractional dispersion model for rivers, *Environ. Fluid. Mech.*, 6(5), 451– 475.

González-Pinzón, R., Haggerty, R., & Argerich, A. (2014). Quantifying spatial differences in metabolism in headwater streams. Freshwater Science, 33(3), 798–811. https://doi.org/10.1086/677555

González-Pinzón, R., Ward, A. S., Hatch, C. E., Wlostowski, A. N., Singha, K., Gooseff, M. N., et al. (2015). A field comparison of multiple techniques to quantify groundwater–surface-water interactions. Freshwater Science, 34(1), 139–160. https://doi.org/10.1086/679738

González-Pinzón,R.,Peipoch,M.,Haggerty,R.,Martí,E.,&Fleckenstein,J.H.(2016). Night time and day time respiration in a head water stream. Ecohydrology, 9(1), 93–100. https://doi.org/10.1002/eco.1615

Haggerty, R., A. Argerich, and E. Martí (2008), Development of a “smart” tracer for the assessment of microbiological activity and sediment-water interaction in natural waters: The Resazurin-Resorufin system, Water Resour. Res., 44, W00D01, doi:10.1029/2007WR006670.

Haggerty, R., and P. C. Reeves (2002), STAMMT-L 1.0, formulation and user's guide, *Tech. Rep. ERMS #520308*, Sandia Natl. Lab., Albuquerque, N. M.

Kelly, J. F., Bolster, D., Meerschaert, M. M., Drummond, J. D., and Packman, A. I. (2017), FracFit: A robust parameter estimation tool for fractional calculus models, *Water Resour. Res.*, 53, 2559– 2567, doi:10.1002/2016WR019748.

Kerr, P.C. , Gooseff, M.N., Bolster, D. (2013), The significance of model structure in one-dimensional stream solute transport models with multiple transient storage zones – competing vs. nested arrangements, Journal of Hydrology, Volume 497, 2013, Pages 133-144, doi:10.1016/j.jhydrol.2013.05.013.

Lemke, D., Liao, Z. J., Wohling, T., Osenbruck, K., & Cirpka, O. A. (2013). Concurrent conservative and reactive tracer tests in a stream undergoing hyporheic exchange. Water Resources Research, 49, 3024–3037. https://doi.org/10.1002/wrcr.20277

Marion, A., M. Zaramella, and A. Bottacin-Busolin (2008b), Solute transport in rivers with multiple storage zones: The STIR model, *Water Resour. Res.*, 44, W10406, doi:10.1029/2008WR007037

Runkel, R. L. (1998). One-dimensional transport with inflow and storage (OTIS): A solute transport model for streams and rivers, edited, US Department of the Interior, US Geological Survey.

Runkel, R. L., and S. C. Chapra (1993), An efficient numerical solution of the transient storage equations for solute transport in small streams, *Water Resour. Res.*, 29, 211–215, doi:10.1029/92WR02217.

Yakirevich, A.; Shelton, D.; Hill, R.; Kiefer, L.; Stocker, M.; Blaustein, R.; Kuznetsov, M.; McCarty, G.; Pachepsky, Y. Transport of Conservative and “Smart” Tracers in a First-Order Creek: Role of Transient Storage Type. Water 2017, 9, 485

Wörman, A., A. I. Packman, and K. Jonsson (2002), Effect of flow-induced exchange in hyporheic zones on longitudinal transport of solutes in stream and rivers, *Water Resour. Res.*, 38(1), 1001, doi:10.1029/2001WR000769

Chapter 6

6 Does the mass balance of the reactive tracers resazurin and resorufin close at the cellular scale? [4]

6.1 Introduction

Resazurin (Raz) is a redox-sensitive phenoxazine frequently used to estimate biological activity. In appropriate reducing conditions, Raz (blue in color) irreversibly loses an oxygen ion to become resorufin (Rru). Rru (pink in color) also can undergo a further reduction to colorless dihydroresorufin, but this reaction is reversible by sample exposure to oxygen. Importantly for research in aquatic ecosystems, the Raz-Rru tracer system mimics the behavior of a binary nano-switch capable of indicating water interactions with metabolic hotspots. Raz, the tracer injected, begins in state 0 (zero) when it is added and remains in that state unless it enters a reducing environment where it is irreversibly transformed to Rru and, thereafter, registers state 1 (one). States 1 and 0 can be identified at low concentrations (currently parts per billion) using fluorescent signatures. Field and laboratory studies have shown that the transformation of Raz in filtered water is negligible compared to that in sediments (Haggerty et al., 2008, 2009). Also, studies have shown that Raz can be reduced to

[4] The content of this chapter is described in the paper: Dallan E., Regier P., Marion A., González-Pinzón R., *Does the mass balance of the reactive tracers resazurin and resorufin close at the cellular scale?*. Paper submitted to: Journal of Geophysical Research: Biogeosciences, with assigned code at submission 2019JG005435

Rru by strict aerobes, facultative anaerobes, aerotolerant and microaerophile organisms, but not by strict anaerobes and thus preferentially indicates aerobic metabolism (Strotmann et al., 1993; McNicholl et al., 2007; O'Brien et al., 2000; Guerin et al., 2001; Karakashev et al., 2003; Mariscal et al., 2009; Min and Kang, 2011; Ziegler et al., 2011; González-Pinzon et al., 2012, 2014; Knapp et al., 2018). Combined, these ideal properties of the Raz-Rru system have helped hydrologists and ecologists quantify parameters and fluxes related to exchange with, and storage within, metabolically active transient storage zones in the near subsurface (e.g., benthic, hyporheic and riparian zones).

Like most hydrologic tracers, Raz and Rru have non-idealities that affect their mass balance. First, it is unclear if the irreversible transformation of Raz uniquely yields Rru or also other unidentified by-products that are not fluorescent (O'Brien et al., 2000) and thus cannot be quantified through fluorescence spectroscopy, which is currently the most accurate method available to quantify Raz and Rru. Second, both Raz and Rru undergo sorption, particularly at lower pH values (Lemke et al., 2014), and this may cause transient mass retention operating at timescales longer than the duration of field studies, effectively causing incomplete recovery of the tracers. Haggerty et al. (2009) and Lemke et al. (2014) conducted non-equilibrium (kinetic) and equilibrium sorption analyses, and found that linear sorption models are adequate, but emphasized differences between the sorption distribution coefficients of Raz and Rru. Third, being fluorescent tracers, Raz and Rru may undergo photodecay. However, studies have shown that the time scales of photodecay are several tens of hours for resorufin and hundreds of hours for resazurin (Haggerty et al., 2008, 2009), suggesting that it is usually negligible for the duration of most field studies.

As a result of non-idealities, most hydrologic studies where the Raz-Rru system has been used have consistently found that the total mass recovered (Raz and Rru) is smaller than the mass of Raz injected after accounting for dilution. Also, this difference has been typically larger than the uncertainty in the quantification of the tracer concentrations. For example, Haggerty et al. (2009) reported 15% loss of mass, Argerich et al. (2011) found mass loss of 62.8%, Stanaway et al. (2012) obtained mass balance range of 49 - 77% in column experiments, and Yakirevich et al. (2017) reported mass recovery of 13.7% (3.9% Raz + 9.8% Rru). To date, it is unclear if the unclosed Raz mass balance can be explained by the existence of additional reaction products that are produced during the transformation of Raz to Rru, the long-term sorption of the tracers, some degree of photodecay, all combined, or some other mechanism of uptake at the cellular scale.

This study seeks to answer the question: Does the mass balance of Raz and Rru close at the cellular scale? In our study, we minimized the effects that sorption and photodecay may have on the mass recovery of the tracers and used different microbial communities to investigate recovery patterns independent of specific microbial species. Our findings indicate a near complete mass recovery at the cellular scale and suggest that incomplete recovery is likely related to sorption and transient storage processes retaining the tracers over timescales longer than the field experiments.

6.2 Materials and Methods

6.2.1 Cellular Scale Experiments

In our microbial experiments we used 1) yeast cells (*Saccharomyces cerevisiae*, from commercial dry yeast) as generic facultative anaerobe cells, 2) naturally present microorganisms from the Rio Grande river (surface water sampled at locations near Albuquerque, New Mexico, USA), and 3) Bacillus subtilis (*B. Subtilis*) as a facultative anaerobe, Gram-positive soil and water-dwelling bacterium with demonstrated success in previous Raz-Rru studies (González-Pinzon et al., 2012).

All the tests had the same experimental setup, except for preparation of the initial solutions used with the different types of microorganisms. Yeast solution was prepared from 0.8 g dry yeast and 8.0 g sugar in 4 L ultrapure water (18 MΩ) at room temperature (~21°C). This solution was stirred for 15 minutes to dissolve the sugar and activate the yeast. For the experiment with unfiltered river water, ~10 L of surface water was collected from the Rio Grande river and stored overnight to allow suspended solids to settle out. The day of the experiment, a volume of about 4 L was collected from the superficial layer of the settled water. For the experiment using *B. subtilis*, cells were purchased from ATCC (ATCC® 23857) as freeze-dried stock, revived following manufacturer recommendations (i.e., hydrated in 10 mL of ATCC® medium 415), used to inoculate autoclaved vials containing medium 415, and incubated at 26°C for 24 hours. The final solution for the experiment was prepared using a total of 200 mL of incubated cultures, in a solution of 500 mL medium and 3.3L ultrapure water at 26°C to encourage the highest possible levels of bacterial activity. Although the other experiments were all started at room temperature, the *B. subtilis* experiment was started at 26°C to avoid shocking the incubated cultures, and allowed to return to room temperature (21°C) throughout the experiment.

The setup for each test was composed of 18 flasks, each with a starting volume of 205 mL, following the design presented in Figure 6.1 and Table 6.1. The 4 L of culture

solution was split into 200 mL aliquots and placed into acid-washed 250 mL Erlenmeyer flasks. Three flasks were used as controls in each experiment: one with ultrapure water only, one with ultrapure water and 200 ppb Raz but no culture, and one with ultrapure water and culture but no Raz. The remaining 15 flasks were dosed as triplicates of 5 Raz concentrations (50, 100, 200, 300, and 400 ppb). Flasks were wrapped in foil to eliminate potential photodecay, placed on a rotary shaker table, and agitated at 110 rpm for the duration of the experiment to minimize potential for anaerobic conditions. Dosing flasks was conducted as quickly as possible (within 15 minutes) to minimize variability between flasks and facilitate sampling as soon as possible after dosing to establish baseline readings. Four different tests were carried out in this study (Table 6.2). The first two tests used the yeast solution, where the first (Exp. 1) was run for about 5 hours and the second (Exp. 2) for about 2.5 days. Exp. 3 using settled Rio Grande river water was carried out for about 4 days, and Exp. 4, conducted with the *B. subtilis*, lasted about 1.5 days.

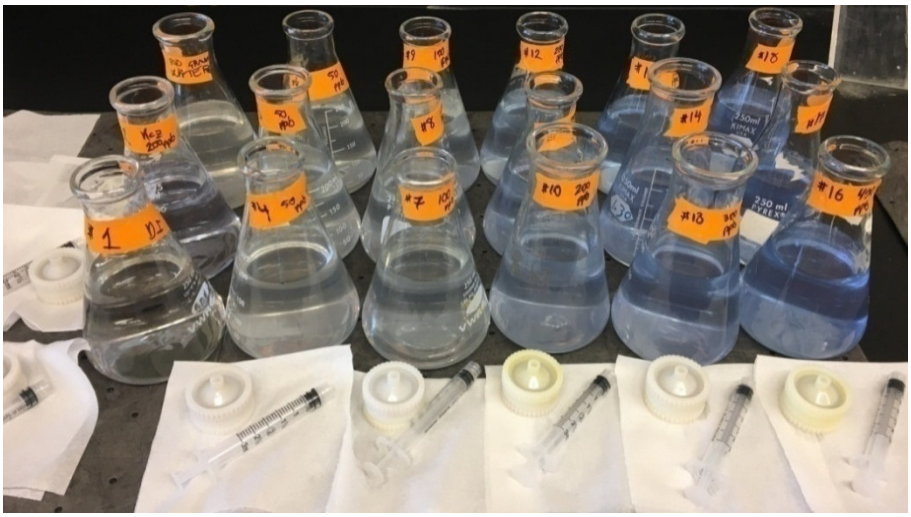

Figure 6.1. Experimental setup after Raz additions: 18 flasks include 3 controls (flasks #1-2-3) and 5 Raz concentrations series, each with 3 replicates (flasks #4 - 18).

Table 6.1. Experimental setup: Individual experiment arrangement.

Flask number	Main solution	Raz initial concentration [ppb]
1	Medium *	0
2	Medium + Raz	200
3	Initial solution**	0
4-5-6	Initial solution + Raz	50
7-8-9	Initial solution + Raz	100
10-11-12	Initial solution + Raz	200
13-14-15	Initial solution + Raz	300
16-17-18	Initial solution + Raz	400

Notes. * Medium is ultrapure water for yeast and Rio Grande tests; broth medium for bacteria test. ** Initial solution is: yeast solution for yeast tests, Rio Grande river water for the Rio Grande test, and bacteria solution for bacteria test.

Table 6.2. Experimental setup: type of cells, concentrations and test durations across experiments.

Experiment number	Initial solution	Raz initial concentrations [ppb]	Test duration
1	Yeast	0, 50, 100, 200, 300, 400	5.3 hours
2	Yeast	0, 50, 100, 200, 300, 400	71 hours
3	Rio Grande water	0, 50, 100, 200, 300, 400	91 hours
4	B. subtilis	0, 50, 100, 200, 300, 400	31 hours

6.2.2 Experimental Sampling, Storage and Readings

Tests were conducted at room temperature (21°C). Samples were taken after the addition of Raz at increasing time intervals, with higher frequency during the first 5-6 hours (sub-hourly), and with decreasing frequency thereafter. For Exp. 2, sampling started after 5 hours in an attempt to evaluate recovery behavior beyond the timescales measured in Exp. 1. For each sample, a small aliquot (~3 mL) was removed from each flask, with 2 mL filtered through 0.2 μm polycarbonate filters (Whatman) into cuvettes and buffered with 1 M sodium phosphate to reach pH of 8.5 (Haggerty et al., 2008; Gonzalez-Pinzon et al., 2012). All samples were refrigerated immediately after collection until analysis. Samples were analyzed using a Varian Cary Eclipse fluorescence spectrophotometer (Agilent), and all samples for a given experiment were analyzed on the same day to minimize day-to-day variation in instrument performance.

6.2.2.1 Data analysis and mass recovery

The concentrations of Raz and Rru were calculated from the fluorescence readings relative to standard curves using available Matlab codes (Knapp et al., 2018) to obtain Raz and Rru concentration values, $C_{i,j,k}^{Raz}$ and $C_{i,j,k}^{Rru}$ expressed in [μmol L^{-1}], where index i=1-5 and indicates concentration series (50, 100, 200, 300, and 400 ppb, respectively), index j=1-3 represents the relevant flask number for each triplicate (see Table 6.1), and index k refers to the sample number, corresponding to the time the sample was taken (see **Errore. L'origine iferimento non è stata trovata.**÷Table 8.4 in Appendix).

The total concentration of a flask at a given sampling time was calculated as:

$$C_{i,j,k}^{Tot} = C_{i,j,k}^{Raz} + C_{i,j,k}^{Rru} \quad (6.1)$$

6.2.3 Statistics

6.2.3.1 Error analysis

Preliminary tests were carried out to estimate the expected error associated with preparation of samples and readings from the spectrofluorometer. One 100 ppb Raz solution

in deionized water was prepared and shaken. From this solution, five 10-vials series were filled with 0.1 ml buffer and 1 ml solution using a 0.02-0.2 mL micropipette for buffer and a 0.1-1 mL micropipette for Raz solution.

The series were analyzed using the spectrofluorometer (following methods described in the article), and the mean value of the intensity signals I_p was calculated for each p series, for both wavelengths associated with Raz and Rru. For each p series, the variability v_p was estimated as:

$$v_p^{raz} = \frac{\text{std}\,(I_{j,p}^{raz})}{I_p^{raz}} \quad (6.2)$$

$$v_p^{rru} = \frac{\text{std}\,(I_{j,p}^{rru})}{I_p^{rru}} \quad (6.3)$$

where j ranges from 1 to 10 and represents the 10 vials of each series.

The mean variability of each wavelength was calculated over the 5 series:

$$v^{raz} = \frac{v_p^{raz}}{5} \quad (6.4)$$

$$v^{rru} = \frac{v_p^{rru}}{5} \quad (6.5)$$

The results of pipetting tests are shown in Table 6.3. Variability ranged 1.6-4% for Raz wavelength (602/632 nm) and 1.7-6.9% for Rru wavelength (571/584 nm). The obtained values were the sum of errors associated with pipette precision, pipetting technique (operator error), lamp variability and manufacturing defects of cuvettes.

Considering that concentrations were calculated from independent readings of the two wavelength pairs used for Raz and Rru, we estimated the expected relative error as the standard deviation of each fluorescence measurement, combined using propagation of error to calculate the standard deviation expected for full recovery (σ_r):

$$\sigma_r = \sqrt{v^{raz2} + v^{rru2}} \quad (6.6)$$

Based on data presented in Table 6.3, and the formula for relative error, we estimated σ_r = 5.1% for a given sample. Next, the range for full recovery was calculated as $2\sigma_r$, giving a range of +/-10.2%, equivalent of the 95% confidence interval (CI).

Table 6.3 Fluorescence intensity (counts per second) for experimental error tests

sample #	"Raz" Wavelength 602/632nm					"Rru" Wavelength 571/584nm				
	1p	6p	7p	2p	5p	1p	6p	7p	2p	5p
1	17.49	19.74	19.68	17.71	18.42	11.65	13.81	12.72	11.81	12.21
2	17.72	19.36	19.74	17.81	18.93	12.03	12.81	14.01	11.80	12.53
3	17.57	19.39	19.03	17.86	18.47	11.88	12.76	12.94	11.88	12.12
4	17.64	19.27	18.90	17.77	17.61	12.14	12.67	12.31	11.80	11.73
5	17.98	19.00	19.84	18.16	18.28	11.93	12.52	14.10	11.98	12.13
6	18.07	19.40	19.41	17.14	18.77	12.38	12.61	12.69	11.59	12.47
7	18.06	19.46	19.29	17.97	18.60	12.25	12.68	12.80	11.92	12.22
8	17.73	20.56	19.04	18.19	19.43	11.95	14.70	12.78	12.18	13.67
9	17.15	17.75	19.33	18.40	19.46	11.54	12.80	12.48	12.33	13.61
10	17.47	18.23	18.70	18.05	17.82	11.78	11.98	15.13	11.91	11.75
I_p	17.69	19.22	19.29	17.91	18.58	11.95	12.94	13.20	11.92	12.44
std_p	0.29	0.77	0.38	0.34	0.60	0.26	0.76	0.91	0.21	0.68
v_p	1.6%	4.0%	2.0%	1.9%	3.2%	2.2%	5.9%	6.9%	1.7%	5.5%

Note. Readings are reported for both the couples of excitation/emission wavelengths. I_p represents the averaged intensity value for each series; std_p represents the standard deviation calculated for the 10 intensity values of each series; v_p represents the variability of the readings for the same series, expressed in percentage.

6.2.3.2 Recovery analysis

Mean values of Raz, Rru and combined (Raz+Rru) concentrations for sampling time k were calculated using the three replicates ($j = 1,2,3$) of the same initial concentration series i:

$$\tilde{C}_{i,k}^{tracer} = \frac{\sum_{j=1}^{3} C_{i,j,k}^{tracer}}{3} \quad (6.7)$$

where $tracer$ represents either Raz, Rru or the summation of both (i.e., Raz+Rru, referred to as Tot).

The mean total concentration for each initial concentration series i, for all sampling times k, was:

$$\tilde{C}_{i}^{Tot} = \frac{\sum_{k=1}^{n_k} \tilde{C}_{i,k}^{Tot}}{n_k} \quad (6.8)$$

where n_k is the number of samples for each experiment.

For each initial concentration series i, we quantified the sample variability within comparable flasks (i.e., for $j = 1,2,3$) for each sampling event k, i.e.,$v_{i,k}$, and across sampling events ($k = 1,2,\dots,n_k$), i.e., v_i, as:

$$v_{i,k} = \frac{std(C_{i,j,k}^{Tot})}{\tilde{C}_{i,k}^{Tot}} \quad (6.9)$$

$$v_i = \frac{std(\tilde{C}_{i,k}^{Tot})}{\tilde{C}_i^{Tot}} \quad (6.10)$$

Recovery percentages were estimated for each initial concentration series i, at sampling event k as:

$$R_{i,k}^{tracer} = 100 \cdot \frac{\tilde{C}_{i,k}^{tracer}}{\tilde{C}_i^{tracer}} \quad (6.11)$$

The variability associated with $R^{Tot}{}_{i,k}$was calculated for each series i, i.e., V_i, and for each complete experiment (i.e., V for all five series i), as:

$$V_i = std\left(R_{i,k}^{tot}\right) \quad (6.12)$$

$$V = mean(V_i) \quad (6.13)$$

We examined several metrics to statistically quantify the mass recovery of Raz injected compared to the Raz+Rru retrieved. First, we conducted tests to evaluate errors associated with sample preparation and spectrofluorometer readings (see section 6.2.3.1).The standard deviation (σ_r) associated with these errors was 5.1%, and this value was used to establish a statistical complete recovery range of 100% ±5.1%. Therefore, values greater than 100%±10.2% ($2\sigma_r$) were interpreted as incomplete recovery or invalid. We also calculated standard deviations for the results of each experiment, following Eqs. (6.12) and (6.13), to compare the relative variation within a given experiment to other experiments. Finally, we assessed trends by fitting regression lines and report regression statistics in the results and discussion. Outliers were identified by total concentration variability $v_{i,k}$ larger than 100±15.3% ($3\sigma_r$), with a total of three values in Exp.2 (yeast long test) removed, all associated with improper sample preparation or handling (#16-17-18 at t=49.1 hours).

6.3 Results and Discussion

6.3.1 Mass recovery

Figure 6.2 shows an example of the evolution of the concentrations of Raz, Rru, and total molar concentrations (Raz+Rru) obtained for the short experiment with yeast (Exp.1). Equivalent plots for Exps. 2-4 are reported in the Appendix (Figure 8.1 - Figure 8.3). Consistent patterns were generally observed of decreasing Raz concentration through time, with steeper slopes for higher concentrations. Similarly, Rru concentrations increased, while Raz+Rru concentrations were steady (Figure 6.2).

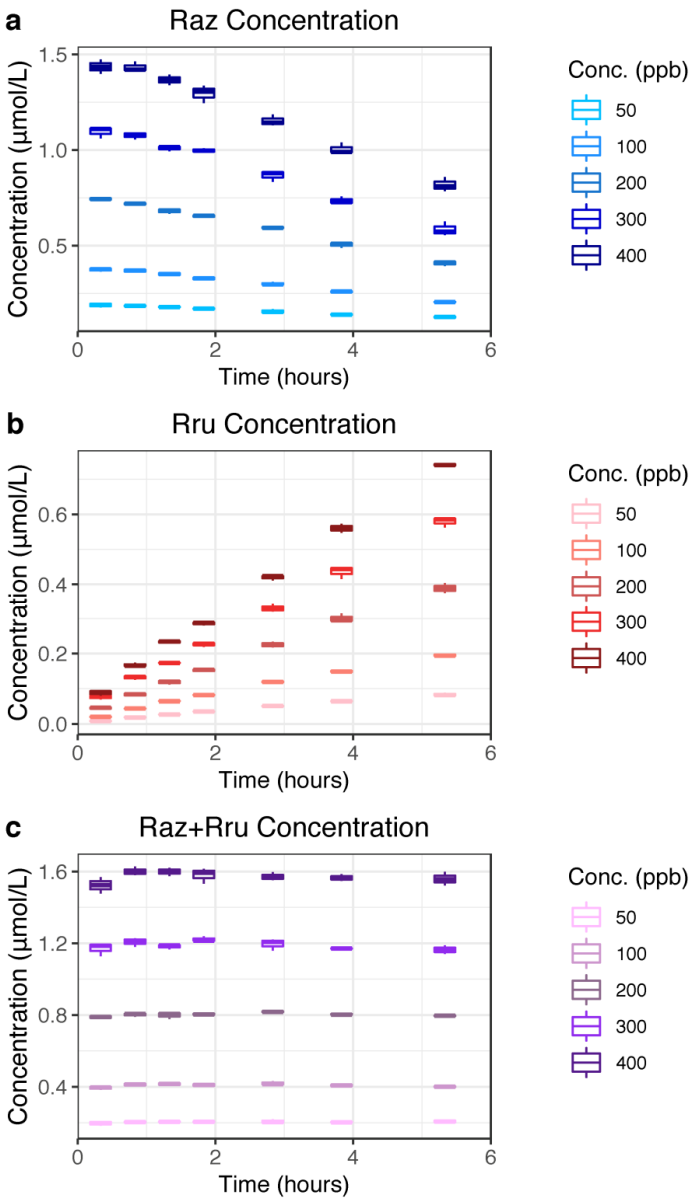

Figure 6.2. Example of the evolutions of a) Raz, b) Rru and c) Raz+Rru molar concentrations $C_{i,j,k}^{Raz}$, $C_{i,j,k}^{Rru}$, $C_{i,j,k}^{Tot}$ during the short experiment with yeast (Experiment 1 in Table 3). Flasks with different starting concentrations of Raz are shown in different colors. Boxplots represent the variability among triplicate flasks for each Raz concentration, with whiskers representing experiment-specific standard deviations.

Recovery percentage statistics are summarized in Table 6.4 (see Table 8.1÷Table 8.4 in Appendix for full datasets and statistics), and recovery time-series are plotted in Figure 6.3, along with complete recovery ranges, experiment-specific standard deviations, and linear regression trend lines.

For Exp. 1, the mass recovery $R_{i,k}^{tot}$ ranged from 96.4 to 103.0%, with a mean standard deviation V of 1.7% (Table 6.4). All values were within the complete recovery range ($\pm\sigma_r$) and no significant trend was observed (R^2=0.00, p=0.7831), indicating complete recovery throughout the experiment.

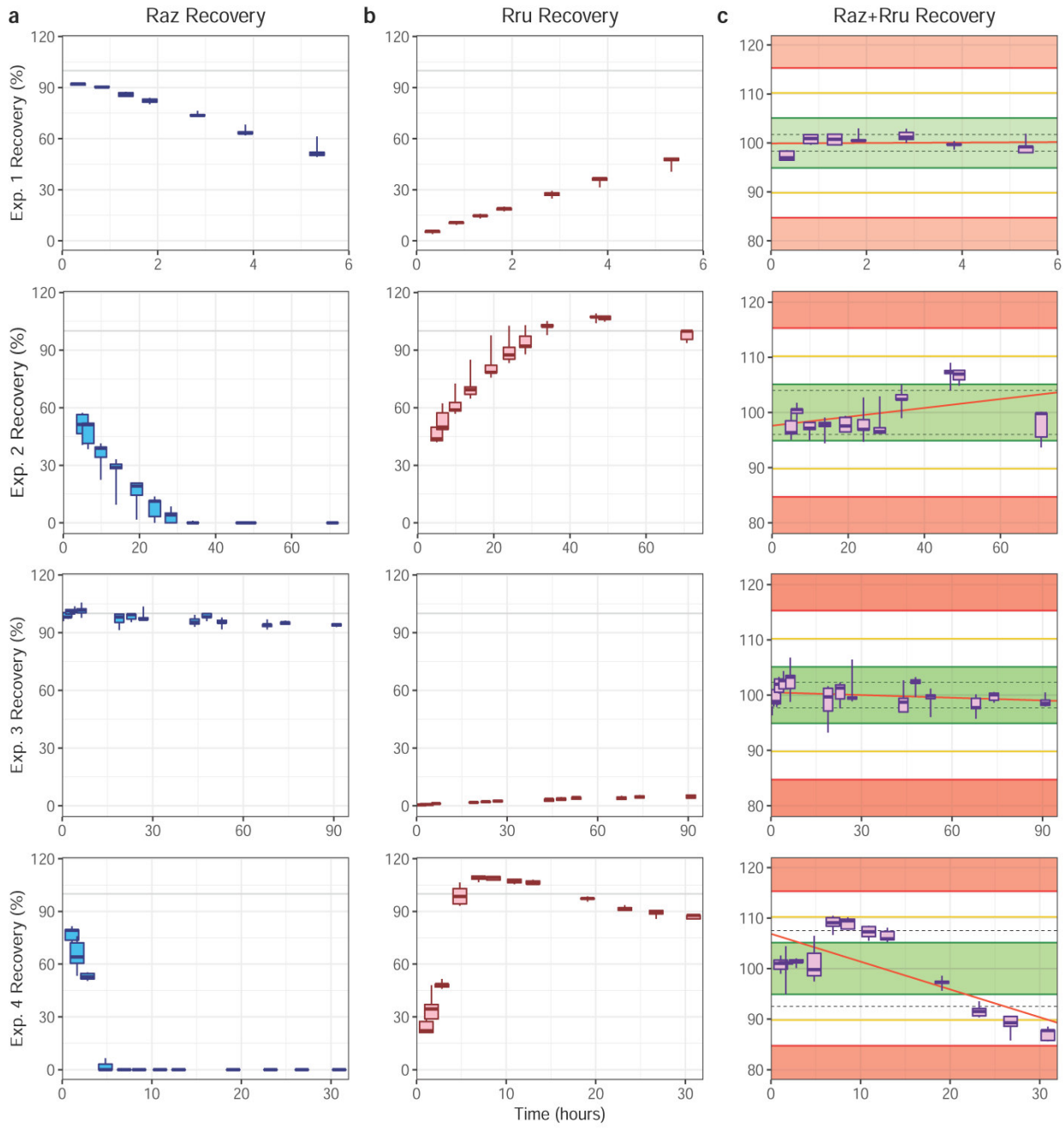

Figure 6.3. Percent recoveries $R_{i,k}^{tracer}$ for Exps. 1-4 for a) Raz, b) Rru, and c) Raz+Rru. Each box plot includes all Raz concentrations for each sampling point. Panel c is color-coded to recovery, where the green shaded region represents the range of complete recovery ($\pm\sigma_r$), while yellow lines show $\pm 2\sigma_r$ (suggesting incomplete recovery). Red shaded regions represent $\pm 3\sigma_r$. Dashed black lines represent experiment-specific standard deviations. Solid orange lines show best-fit linear regression lines.

Exp. 2 expanded the time-scale of Exp. 1, and showed mass recoveries $R_{i,k}^{tot}$ in the range 94.4÷109.0% and a standard deviation V of 3.9%. The standard deviation was less than the standard deviation for experimental errors (5.1%), and most individual points fell within the range of $\pm\sigma_r$, with no values greater than $2\sigma_r$. Statistically, there was a weak trend (R^2=0.16, p=0.0026) driven by abnormally increasing values between hours 30 and 50, but this behavior

disappeared before the end of the experiment. As such, Exp. 2 generally suggested mass closure in timescales approaching the longest published field experiments conducted with Raz (e.g., Argerich et al., 2011; Gonzalez-Pinzon et al., 2014).

For Exp. 3, we obtained recoveries $R_{i,k}^{tot}$ in the range of 93.2-106.8%, with a mean standard deviation V of 2.3%. As for Exps. 1 and 2, this value was within the complete recovery range. Moreover, only 3 of 75 measurements were greater than σ_r, with no values greater than $2\sigma_r$. A low R^2 and relatively high p-value indicated no significant trend was present over time (R^2=0.04, p=0.0797). As such, Exp. 3 consistently exhibited complete recovery of Raz using natural microbial communities, even at multi-day time-scales.

Finally, Exp. 4 mass recoveries $R_{i,k}^{tot}$ were in the range 85.6÷110.4%, with a standard deviation V of 7.5%. This experiment was characterized by higher variability than the previous three tests, and we observed incomplete recovery towards the end of the experiment (after 25 hours). Unlike the previous three tests, the standard deviation for the experiment was higher than σ_r, suggesting high variability during the test and several points fell outside the $2\sigma_r$ range (although no points fell outside the 3σ range). As shown in Figure 6.3 and quantified by linear regression of mass recovery over time (R^2=0.53, p<0.0001), the higher standard deviation was driven by incomplete recovery towards the end of the experiment. During the first ~20 hours of Exp. 4, a similar pattern to Exp. 2 was observed, where values increase, and then returned to baseline, yielding no linear trend (R^2=0.00, p=0.7722, n=45), and a standard deviation (4.5%) less than the standard deviation of the experimental error.

From the four experiments conducted, mass recoveries $R_{i,k}^{tot}$ ranged from 85.6% to 110.4%, with a maximum standard deviation for a single time-series of 8.5% (Table 6.4). Across the four experiments, average standard deviation was 3.9%, lower than the experimentally determined variability within the experimental error of 5.1%. As such, findings from this study generally suggested that the mass balance of the Raz-Rru system closed at the cellular scale. The *B. subtilis* experiment indicated lower recoveries (85.6-95.6%, Table A5 in Appendix) starting after ~13 hours of total Raz consumption. This timescale is arguably much longer than most field experiments (typically <8 hours), particularly considering that cellular scale experiments, unlike field experiments, feature near perfect mixing conditions and contact times between solutes and bacteria that approach the duration of the experiments. Furthermore, Exp. 4 was conducted under conditions optimized for bacterial activity (e.g., removal of nutrient and temperature limitations), which are not common in natural systems. In contrast to Exp. 4, the experiment conducted with natural microbial communities (Exp. 3) showed very low Raz transformation and Rru production,

even after 90 hours. The low values for conversion of Raz to Rru obtained in our experiments may be partially explained by lower microbial activity during the winter when samples were collected, but strongly suggest that the conditions required to replicate incomplete recovery in Exp. 4 do not represent activity of natural microbial communities used for Exp. 3.

Table 6.4. Summary of recovery results for each experiment.

1st exp	Raz 50	Raz 100	Raz 200	Raz 300	Raz 400
$\tilde{C}_i^{Tot}$ [µmol/L]	0.204	0.409	0.802	1.188	1.572
min $R_{i,k}^{tot}$[%]	96.5%	96.4%	98.3%	98.0%	96.9%
max $R_{i,k}^{tot}$[%]	101.9%	102.9%	102.1%	103.0%	101.9%
V_i[%]	1.8%	2.2%	1.2%	1.8%	1.7%
V[%]	1.7%				

2nd exp	Raz 50	Raz 100	Raz 200	Raz 300	Raz 400
$\tilde{C}_i^{Tot}$ [µmol/L]	0.995	1.018	1.005	0.999	1.006
min $R_{i,k}^{tot}$[%]	96.3%	95.1%	96.2%	94.7%	94.4%
max $R_{i,k}^{tot}$[%]	107.7%	109.0%	107.0%	107.3%	105.1%
V_i[%]	4.3%	4.7%	3.8%	3.8%	3.8%
V[%]	4.0%				

3rd exp	Raz 50	Raz 100	Raz 200	Raz 300	Raz 400
$\tilde{C}_i^{Tot}$ [µmol/L]	0.203	0.398	0.784	1.160	1.533
min $R_{i,k}^{tot}$ [%]	93.2%	95.7%	97.6%	97.6%	96.3%
max $R_{i,k}^{tot}$ [%]	103.3%	106.4%	106.8%	103.2%	104.3%
V_i[%]	2.7%	2.9%	2.3%	1.7%	2.3%
V[%]	2.3%				

4th exp	Raz 50	Raz 100	Raz 200	Raz 300	Raz 400
$\tilde{C}_i^{Tot}$ [µmol/L]	0.949	1.013	1.011	1.009	1.044
min $R_{i,k}^{tot}$[%]	88.5%	87.8%	87.7%	85.6%	85.7%
max $R_{i,k}^{tot}$[%]	109.5%	109.8%	110.2%	110.4%	110.1%
V_i[%]	7.4%	7.5%	7.5%	8.5%	7.8%
V[%]	7.5%				

Note. Mean Raz+Rru concentration $\tilde{C}_i^{Tot}$ for each series i, minimum and maximum recovery percentages $R^{tot}{}_{i,k}$ for each series i, recoveries variability V_i for each series i, and recovery variability V for each set of experiments with a given microbial group.

6.3.2 Anomalies in recovery time-series and potential drivers of incomplete Raz-Rru mass recovery

In Exp.2 and Exp.4 we observed slightly higher recovery percentages $R_{i,k}^{tot}$ after complete Raz consumption (i.e., after 30 hours for Exp.2 and 5 hours for Exp.4, Figure 3).

We estimated a recovery increase of about 7% from the difference between the mean recovery percentage before Raz total consumption (97.9% for Exp.2 between 5.0 - 28.3 hours, and 100.9% for Exp.4 between 1.1 - 4.8 hours) and the mean recovery percentage for the peak (105.2% for Exp.2 between 34 - 49.1 hours and 107.9% for Exp. 4 between 6.9 - 13.0 hours). Percentages greater than 100% in Exps. 2 and 4 are likely an artifact of the calculation of $\tilde{C}_i^{tot}$, considering that recoveries $R_{i,k}^{tot}$ are calculated with respect to the mean concentration $\tilde{C}_i^{tot}$ (Eq. 6), and lower recoveries towards the end would lower $\tilde{C}_i^{tot}$. In this context, O'Brien et al. (2000) and Chen et al. (2018) demonstrated that a secondary reaction from Rru to hydroresorufin is favored after all Raz has been reduced (as observed for Exps. 2 and 4), and that this reaction can happen both inside and outside cells. Another study using re-cellularized kidney scaffolds observed a fluorescence peak that gradually decreased throughout the assay, decaying to zero by 24 h, demonstrating that cells were capable of secondary reduction of Rru to hydroresorufin (Uzarski et al, 2017). Moreover, Vehniäinen et al. (2012) demonstrated that in the liver S9 fraction of some fish species, Resorufin was enzymatically reduced to a less fluorescent form. Together, these findings suggest that the decreasing Rru concentrations observed after complete Raz consumption in Exps. 2 and 4 are indicative of additional non-fluorescent product formation, and we recommend further investigation on this particular reaction pathway to find an accurate method to quantify the currently unmeasurable byproduct formation.

In light of the mass balance closure generally observed in the four tests conducted in this study, we do not find compelling evidence suggesting that microbial activity governs the lack of mass balance closure commonly observed in field studies. Instead, our results suggest that the incomplete Raz-Rru recovery observed in field experiments is largely associated with physical or chemical processes. Both Raz and Rru undergo photochemical decay, but Haggerty et al. (2008) demonstrated that the time-frame for photodecay is tens of hours for Raz and hundreds of hours for Rru. As such, minimizing photodecay during field experiments only requires storing samples in the dark, which is standard practice. Another potential explanation for incomplete recovery from both laboratory and field studies most strongly support a physicochemical mechanism, where sorption to particulates has been identified as a primary driver of incomplete Raz mass recovery (Lemke et al., 2014; Knapp & Cirpka, 2017), particularly when the sorption timescales are much longer than the experimental timescales.

6.4 Conclusions

We conducted laboratory experiments to investigate mass balance closure of the Raz-Rru system at the cellular scale. Four tests were performed, with three different microbial groups (yeast, native microbial communities and pure *B. subtilis* cells), different initial concentrations of Raz (0-400 ppb) and different test durations (5-91 hours). Our tests generally indicated full mass recovery, even under optimal conditions for microbial activity. One test conducted with *B. subtilis* exhibited incomplete mass recovery, but only after 25 hours. Natural microbial communities present in water collected from Rio Grande River converted less than 10% of Raz to Rru after 91 hours, and exhibited complete mass recovery throughout. Interestingly, these results support previous studies showing that the conversion of Raz to Rru is negligible in the water column and that this fact can be used to investigate the extent of reactive transport in different compartments of the stream network (e.g., main channel vs. surface transient storage zones, and benthic and hyporheic zones). Combining our results which suggest complete mass recovery at the cellular scale, and those from other characterizations of non-idealities of the Raz-Rru tracer system (i.e., photodecay and sorption), we conclude that sorption is likely the main driver of incomplete mass recovery in field studies.

6.5 Acknowledgments

This material is based upon work supported by the National Science Foundation under Award Nos. EAR-1642399 and HRD-1720912. The dataset of Raz and Rru concentrations generated and analyzed during this study will be archived using the CUAHSI-HIS repository. We thank Holly Wilkie, James Fluke, Justin Nichols and Jancoba Dorley for assistance in conducting laboratory tests.

6.6 Bibliography

Argerich, A., Haggerty, R., Martí, E., Sabater, F., and Zarnetske, J. (2011), Quantification of metabolically active transient storage (MATS) in two reaches with contrasting transient storage and ecosystem respiration, J. Geophys. Res., 116, G03034, doi:10.1029/2010JG001379.

Chen, JL, Steele, TWJ, Stuckey, DC. (2018) Metabolic reduction of resazurin; location within the cell for cytotoxicity assays. *Biotechnology and Bioengineering*. 2018; 115:351–358, doi:10.1002/bit.26475

González-Pinzón, R., R. Haggerty, and D. D. Myrold (2012), Measuring aerobic respiration in stream ecosystems using the resazurin-resorufin system, J. Geophys. Res., 117, G00N06, doi:10.1029/2012JG001965.

González-Pinzón, R., Haggerty, R., and Argerich, A. (2014). Quantifying spatial differences in metabolism in headwater streams. Freshwater Science, 33(3), 798–811. https://doi.org/10.1086/677555

Guerin, T., M. Mondido, B. McClenn, and B. Peasley (2001), Application of resazurin for estimating abundance of contaminant-degrading microorganisms, Lett. Appl. Microbiol., 32, 340–345, doi:10.1046/j.1472765X.2001.00916.x.

Karakashev, D., D. Galabova, and I. Simeonov (2003), A simple and rapid test for differentiation of aerobic from anaerobic bacteria, World J. Microbiol. Biotechnol., 19, 233–238, doi:10.1023/A:1023674315047.

Knapp, J. L. A., González-Pinzón, R., & Haggerty, R. (2018). The resazurin-resorufin system: Insights from a decade of "smart" tracer development for hydrologic applications. Water Resources Research, 54. https://doi.org/10.1029/ 2018WR023103

Haggerty, R., A. Argerich, and E. Martí (2008), Development of a "smart" tracer for the assessment of microbiological activity and sediment-water interaction in natural waters: The resazurin-resorufin system, Water Resour. Res., 44, W00D01, doi:10.1029/2007WR006670.

Haggerty, R., E. Martí, A. Argerich, D. von Schiller, and N. Grimm (2009), Resazurin as a "smart" tracer for quantifying metabolically active transient storage in stream ecosystems, J. Geophys. Res., 114, G03014, doi:10.1029/2008JG000942.

Lemke, D., Gonzalez-Pinzon, R., Liao, Z., Wohling, T., Osenbruck, K., Haggerty, R., &Cirpka, O. A. (2014). Sorption and transformation of the reactive tracers resazurin and resorufin in natural river sediments. Hydrology and Earth System Sciences, 18(8), 3151–3163. https://doi.org/ 10.5194/hess-18-3151-2014

Mariscal, A., R. Lopez-Gigosos, M. Carnero-Varo, and J. Fernandez Crehuet (2009), Fluorescent assay based on resazurin for detection of activity of disinfectants against bacterial biofilms, Appl. Microbiol. Biotechnol., 82, 773–783, doi:10.1007/s00253-009-1879-x.

McNicholl, B. P., J. W. McGrath, and J. P. Quinn (2007), Development and application of a resazurin-based biomass activity test for activated sludge plant management, Water Res., 41, 127–133, doi:10.1016/j.watres.2006. 10.002.

Min, T. G., and W. S. Kang (2011), Simple, quick and nondestructive method for Brassicaceae seed viability measurement with single seed base using resazurin, Hortic, Horticult. Environ. Biotechnol., 52, 240–245, doi:10.1007/s13580-011-0182-9.

O'Brien, J., I. Wilson, T. Orton, and F. Pognan (2000), Investigation of the Alamar Blue (resazurin) fluorescent dye for the assessment of mammalian cell cytotoxicity, Eur. J. Biochem., 267, 5421–5426, doi:10.1046/j.1432-1327.2000.01606.x.

Stanaway, D., Haggerty, R., Benner, S., Flores, A., and Feris, K. (2012): Persistent metal contamination limits lotic ecosystem heterotrophic metabolism after more than 100 years of exposure: a novel application of the resazurin resorufin smart tracer, Environ. Sci. Technol., 46, 9862–9871, doi:10.1021/Es3015666

Strotmann, U. J., B. Butz, and W. R. Bias (1993), A dehydrogenase assay with resazurin-practical performance as a monitoring-system and pH-dependent toxicity of phenolic-compounds, Ecotoxicol. Environ. Saf., 25, 79 –89, doi:10.1006/eesa.1993.1009.

Uzarski, J. S., DiVito, M. D., Wertheim, J. A. & Miller, W. M. (2017). Essential design considerations for the resazurin reduction assay to noninvasively quantify cell

expansion within perfused extracellular matrix scaffolds. Biomaterials, 129, 163–175, doi:10.1016/j.biomaterials.2017.02.015.

Yakirevich, A.; Shelton, D.; Hill, R.; Kiefer, L.; Stocker, M.; Blaustein, R.; Kuznetsov, M.; McCarty, G.; Pachepsky, Y. (2017) Transport of Conservative and "Smart" Tracers in a First-Order Creek: Role of Transient Storage Type. Water 2017, 9, 485

Vehniäinen, E., Schultz, E., Lehtivuori, H., Ihalainen, J., Oikari, A., (2012) More accuracy to the EROD measurements—The resorufin fluorescence differs between species and individuals, Aquatic Toxicology, Volumes 116–117, 2012, doi.org/10.1016/j.aquatox.2012.03.007.

Zhou, M., Diwu, Z., Panchuk-Voloshina, N., Haugland, R., (1997) A Stable Nonfluorescent Derivative of Resorufin for the Fluorometric Determination of Trace Hydrogen Peroxide: Applications in Detecting the Activity of Phagocyte NADPH Oxidase and Other Oxidases, Analytical Biochemistry, Volume 253, Issue 2, 1997, doi.org/10.1006/abio.1997.2391.

Ziegler, V. G., J. Knaup, D. Stahl, B. Krammer, and K. Plaetzer (2011), Fluorescence detection and depletion of T47D breast cancer cells from human mononuclear cell-enriched blood preparations by photodynamic treatment: Basic in vitro experiments towards the removal of circulating tumor cells, Lasers Surg. Med., 42, 548

Chapter 7

7 Conclusions and future work

My 3-years research focused on the study of solute transport processes in both wetland and streams, developing numerical methods (two-dimensional for wetlands and one-dimensional for streams) and experimental techniques. In this perspective, several topics were investigated in these fields by using both classical and innovative techniques and by collaborating with some international experts.

Ensuring quality and health safety of rivers and streams is of primary importance for terrestrial environments and human activities. Considering that water quality degradation is mostly caused by the transport and transformation of solutes (pollutants) in rivers, the understanding of solute transport processes has a fundamental role for improving water quality actions and ecological services in these water bodies. The research carried in this context aimed at improving numerical and experimental methods for the study of the fate of solutes in natural stream and factors influencing it, like surface hydrodynamics, mass exchanges between the surface water and retention zones, biogeochemical processes.

The achieved aims are briefly described below and possible future work is highlighted for each topic and for an integrated approach.

7.1 Sedimentation in wetlands

Conclusions	*Future work foreseeing*
The numerical modelling of wetlands focused on free water surface constructed wetlands (FWS CWs) which are artificial vegetated aquatic systems similar in appearance to equivalent natural water bodies. The study of sedimentation in vegetated wetlands gave a first insight of this process, and even if it used simplifying assumptions on the settling/re-suspension rate, it showed that the presence of vegetation affects sedimentation mechanisms. The proposed model was intended as a possible conceptual model to study sediment transport processes in constructed wetlands	In future studies, the formulation of the settling and the re-suspension rate could be further refined and heterogeneous vegetation distributions could be investigated. More detailed simulations and improved theoretical models of sediment transport in wetlands will underpin the development of improved criteria for wetland design. It appears also necessary to identify which contaminants can be associated to particulate matter at the colloidal size and their relative impact in actual environmental conditions.

7.2 Heterogeneous bathymetry in wetlands

Conclusions	*Future work foreseeing*
For the study of heterogeneous bathymetry in wetland a new modelling system was implemented, which was composed by a random bathymetry generator, an hydrodynamic model (Telemac 2D), and a solute transport model. It showed that bathymetric configuration of a wetland affects its hydrodynamics and removal performance. The first simulations gave higher efficiency for isotropic topographies with lower correlation lengths of the bed forms, that is smaller “patches” and higher	More simulations are needed to obtain a robust comparison between different bathymetric configurations and a better correlation between removal efficiency trend and morphological features. Interesting further developments are: the study of heterogeneous distribution of roughness, the effect of poorer resolution in the bathymetric information (mimicking limited or incomplete availability of bathymetric data), the removal effect of vegetation, the processes of mass exchange

bed forms "frequency". One configuration, with transversal bed forms, gave contrasting results: significant worsening with respect the flat case for the higher vertical magnitude of the bed forms and a significant improvement with lower bed forms.	in the hyporheic zone, the interference of biological activity.

7.3 New modeling of transport processes in streams

Conclusions	*Future work foreseeing*
The experimental application of STIR represented a classical approach that permitted to obtained confidence in the management of experimental conservative tracer datasets, in their numerical analysis and in the physical meaning of classical retention parameters. This research moved into innovative aspects in both the numerical and experimental approaches for the study of solute transport in streams. The new software tool STIR-RST was developed for studies based on smart tracer datasets. Its experimental application on Resazurin-Resorufin datasets showed its capability of achieving a good quality in fitting measured breakthrough curves. It allowed calibrating several parameters useful for describing the diffusive properties of the stream and the biological activity associated with the different storage compartments.	Results could be replicated using smart tracer datasets taken in different streams and conditions. This is expected to further improve the modelling system and give new insights on the mechanisms affecting the transport and degradation of reactive solutes in rivers.

7.4 Laboratory observations of smart tracers

Conclusions	*Future work foreseeing*
Results obtained from lab tests on mass conservation of Raz and Rru showed that complete mass recovery is achieved at the cellular scale. Combining these results and those from other characterizations of non-idealities of the Raz-Rru tracer system (i.e., photodecay and sorption), the conclusion was that sorption is likely the main driver of incomplete mass recovery in field studies.	Since two experiments indicated additional production of non-fluorescent compounds, and further investigation is foreseen looking at the chemistry of the reaction, aiming at the finding of an accurate method to quantify the currently unmeasurable byproduct formation.

As above described, future work could further developed each topic but also an integrated approach is suggested for advancing the knowledge about solute fate in water bodies. Prospective research should be addressed for studying in a comprehensive way the different aspects investigated in my research. In particular tracers biologically reactive (as smart tracers are) could be used for both river and wetland experiments. Results from innovative tracer tests could be helpful for improving numerical frameworks including new biologically-related parameters for describing the fate of solute in natural or constructed water bodies.

Appendix

8 Appendix

Chapter 6 Experiments results

The present Appendix contains tables and figure referring to Chapter 6, in order to give the whole series of calculated values for the four experiments.

In the tables, for each i series and each sampling time k, they are reported: concentrations $\tilde{C}_{i,k}^{Tot}$, that represents the average concentration for the 3 replicates of each series; $std_{i,k}$ the standard deviation of the concentrations associated at the 3 replicates, and the recovery $R_{i,k}$ at each sampling time k. In the last two rows, for each i series, we reported the averaged total concentration $\tilde{C}_{i}^{Tot}$ and the variability V_i (standard deviation) associated at the recovery percentages.

The figures, as made for first experiment in Figure 6.2, shows the evolutions of a) Raz, b) Rru and c) Raz+Rru molar concentrations $C_{i,j,k}^{Raz}$, $C_{i,j,k}^{Rru}$, $C_{i,j,k}^{Tot}$ for the other three experiments. Flasks with different starting concentrations of Raz are shown in different colors. Box plots represent the variability among triplicate flasks for each Raz concentration, with whiskers representing experiment-specific standard deviations.

Table 8.1. 1st Experiment results

Series i	Raz 50			Raz 100			Raz 200			Raz 300			Raz 400		
Time k	$\tilde{C}_{i,k}^{Tot}$	$std_{i,k}$	$R_{i,k}$	$\tilde{C}_{i,k}^{Tot}$	$std_{i,k}$	$R_{i,k}$	$\tilde{C}_{i,k}^{Tot}$	$std_{i,k}$	$R_{i,k}$	$\tilde{C}_{i,k}^{Tot}$	$std_{i,k}$	$R_{i,k}$	$\tilde{C}_{i,k}^{Tot}$	$std_{i,k}$	$R_{i,k}$
[hh]	[µmol/L]		%	[µmol/L]		%	[µmol/L]		%	[µmol/L]		%	[µmol/L]		%
0.3	0.197	0.014	96.5	0.394	0.010	96.4	0.789	0.009	98.3	1.170	0.036	98.5	1.524	0.046	96.9
0.8	0.204	0.005	99.6	0.412	0.010	100.9	0.801	0.010	99.9	1.208	0.024	101.7	1.601	0.025	101.9
1.3	0.206	0.003	100.7	0.416	0.009	101.8	0.799	0.019	99.6	1.182	0.014	99.5	1.599	0.023	101.8
1.8	0.205	0.003	100.5	0.410	0.010	100.3	0.805	0.006	100.4	1.223	0.014	103.0	1.581	0.043	100.6
2.8	0.207	0.012	101.2	0.420	0.011	102.9	0.819	0.004	102.1	1.196	0.033	100.7	1.572	0.023	100.0
3.8	0.204	0.003	99.7	0.407	0.007	99.7	0.805	0.004	100.4	1.171	0.001	98.6	1.566	0.019	99.6
5.3	0.208	0.009	101.9	0.400	0.004	98.0	0.796	0.003	99.3	1.164	0.024	98.0	1.559	0.038	99.2
$\tilde{C}_i^{Tot}$ [µmol/L]	0.204			0.409			0.802			1.188			1.572		
V_i	1.8%			2.2%			1.2%			1.8%			1.7%		

Table 8.2. 2nd Experiment results

Series i	Raz 50			Raz 100			Raz 200			Raz 300			Raz 400		
Time k	$\tilde{C}_{i,k}^{Tot}$	$std_{i,k}$	$R_{i,k}$	$\tilde{C}_{i,k}^{Tot}$	$std_{i,k}$	$R_{i,k}$	$\tilde{C}_{i,k}^{Tot}$	$std_{i,k}$	$R_{i,k}$	$\tilde{C}_{i,k}^{Tot}$	$std_{i,k}$	$R_{i,k}$	$\tilde{C}_{i,k}^{Tot}$	$std_{i,k}$	$R_{i,k}$
[hh]	[µmol/L]		%	[µmol/L]		%	[µmol/L]		%	[µmol/L]		%	[µmol/L]		%
5.0	0.180	0.003	96.3	0.350	0.000	95.1	0.709	0.008	98.5	1.080	0.047	100.1	1.400	0.043	96.1
6.5	0.185	0.001	98.6	0.375	0.010	101.8	0.724	0.026	100.5	1.077	0.011	99.9	1.465	0.064	100.6
9.9	0.181	0.004	96.9	0.362	0.002	98.3	0.707	0.011	98.2	1.048	0.022	97.1	1.383	0.033	95.0
13.9	0.184	0.007	98.2	0.359	0.007	97.5	0.705	0.002	97.9	1.069	0.043	99.1	1.375	0.043	94.4
19.3	0.185	0.006	99.1	0.360	0.002	97.6	0.694	0.025	96.4	1.041	0.009	96.5	1.447	0.056	99.4
24.0	0.181	0.002	96.9	0.364	0.007	98.7	0.697	0.006	96.8	1.021	0.012	94.7	1.495	0.057	102.7
28.3	0.180	0.002	96.3	0.356	0.002	96.5	0.692	0.011	96.2	1.049	0.030	97.2	1.498	0.017	102.9
34.0	0.185	0.002	99.0	0.377	0.014	102.4	0.737	0.019	102.3	1.113	0.038	103.2	1.530	0.028	105.1
46.9	0.201	0.007	107.6	0.402	0.005	109.0	0.771	0.016	107.0	1.157	0.030	107.3	1.514	0.034	104.0
49.1	0.201	0.003	107.7	0.397	0.003	107.6	0.765	0.009	106.3	1.131	0.003	104.8			
70.7	0.193	0.031	103.3	0.352	0.025	95.5	0.719	0.013	99.8	1.080	0.029	100.1	1.453	0.032	99.8
$\tilde{C}_i^{Tot}$ [µmol/L]	0.187			0.369			0.720			1.079			1.456		
V_i	4.3%			4.7%			3.8%			3.8%			3.8%		

Table 8.3. 3rd Experiment results

Series i	Raz 50			Raz 100			Raz 200			Raz 300			Raz 400		
Time k	$\tilde{C}_{i,k}^{Tot}$	$std_{i,k}$	$R_{i,k}$	$\tilde{C}_{i,k}^{Tot}$	$std_{i,k}$	$R_{i,k}$	$\tilde{C}_{i,k}^{Tot}$	$std_{i,k}$	$R_{i,k}$	$\tilde{C}_{i,k}^{Tot}$	$std_{i,k}$	$R_{i,k}$	$\tilde{C}_{i,k}^{Tot}$	$std_{i,k}$	$R_{i,k}$
[hh]	[µmol/L]		%	[µmol/L]		%	[µmol/L]		%	[µmol/L]		%	[µmol/L]		%
0.4	0.201	0.010	99.0	0.395	0.006	99.1	0.771	0.011	98.2	1.137	0.003	98.0	1.477	0.013	96.3
0.9	0.200	0.016	98.6	0.396	0.016	99.4	0.781	0.003	99.6	1.136	0.003	97.9	1.507	0.012	98.4
1.7	0.200	0.012	98.9	0.403	0.012	101.2	0.772	0.004	98.4	1.172	0.022	101.0	1.508	0.024	98.4
2.7	0.209	0.008	103.3	0.400	0.010	100.5	0.786	0.024	100.3	1.183	0.014	102.0	1.577	0.036	102.9
4.2	0.208	0.004	102.6	0.409	0.015	102.7	0.790	0.005	100.7	1.174	0.010	101.1	1.599	0.030	104.3
6.4	0.209	0.009	103.2	0.412	0.006	103.5	0.838	0.036	106.8	1.146	0.021	98.8	1.551	0.058	101.2
18.9	0.189	0.004	93.2	0.387	0.005	97.1	0.797	0.029	101.6	1.175	0.034	101.2	1.528	0.015	99.7
22.9	0.207	0.006	102.3	0.395	0.014	99.3	0.766	0.021	97.6	1.182	0.024	101.9	1.552	0.036	101.3
26.9	0.202	0.003	99.5	0.424	0.031	106.4	0.779	0.002	99.3	1.156	0.033	99.6	1.515	0.043	98.9
43.9	0.196	0.003	96.9	0.409	0.010	102.7	0.774	0.019	98.7	1.154	0.040	99.4	1.486	0.035	96.9
47.9	0.208	0.006	102.4	0.397	0.009	99.7	0.801	0.022	102.1	1.198	0.027	103.2	1.575	0.025	102.7
52.9	0.203	0.008	100.0	0.382	0.004	96.0	0.779	0.022	99.4	1.159	0.021	99.8	1.551	0.076	101.2
67.9	0.201	0.010	99.4	0.381	0.005	95.7	0.766	0.027	97.7	1.132	0.049	97.6	1.535	0.040	100.2
73.9	0.203	0.005	100.1	0.393	0.014	98.6	0.789	0.013	100.5	1.164	0.016	100.3	1.518	0.015	99.1
90.9	0.204	0.005	100.5	0.390	0.019	98.0	0.777	0.024	99.1	1.139	0.017	98.1	1.510	0.067	98.5
$\tilde{C}_i^{Tot}$ [µmol/L]	0.203			0.398			0.784			1.160			1.533		
V_i	2.7%			2.9%			2.3%			1.7%			2.3%		

Table 8.4 4th Experiment results

Series i	Raz 50			Raz 100			Raz 200			Raz 300			Raz 400		
Time k	$\tilde{C}_{i,k}^{Tot}$	$std_{i,k}$	$R_{i,k}$	$\tilde{C}_{i,k}^{Tot}$	$std_{i,k}$	$R_{i,k}$	$\tilde{C}_{i,k}^{Tot}$	$std_{i,k}$	$R_{i,k}$	$\tilde{C}_{i,k}^{Tot}$	$std_{i,k}$	$R_{i,k}$	$\tilde{C}_{i,k}^{Tot}$	$std_{i,k}$	$R_{i,k}$
[hh]	[µmol/L]		%	[µmol/L]		%	[µmol/L]		%	[µmol/L]		%	[µmol/L]		%
1.1	0.189	0.002	99.0	0.371	0.009	101.0	0.736	0.007	101.7	1.058	0.029	99.9	1.420	0.021	102.6
1.7	0.181	0.008	94.9	0.372	0.013	101.3	0.732	0.008	101.1	1.069	0.023	100.9	1.446	0.002	104.4
2.8	0.194	0.006	102.0	0.368	0.006	100.1	0.733	0.003	101.3	1.072	0.021	101.2	1.408	0.040	101.7
4.8	0.196	0.005	103.0	0.366	0.005	99.8	0.706	0.015	97.5	1.128	0.039	106.5	1.365	0.023	98.6
6.9	0.203	0.005	106.7	0.398	0.013	108.4	0.790	0.006	109.1	1.170	0.012	110.4	1.524	0.009	110.1
8.6	0.208	0.004	109.5	0.403	0.008	109.8	0.798	0.010	110.2	1.141	0.022	107.8	1.493	0.035	107.8
10.9	0.207	0.002	108.5	0.398	0.012	108.3	0.777	0.004	107.3	1.117	0.015	105.5	1.472	0.051	106.3
13.0	0.206	0.007	108.1	0.388	0.005	105.7	0.767	0.009	105.9	1.137	0.006	107.3	1.458	0.024	105.3
19.1	0.185	0.004	97.3	0.356	0.004	97.1	0.692	0.021	95.6	1.044	0.020	98.5	1.349	0.018	97.4
23.3	0.175	0.004	92.1	0.332	0.007	90.3	0.677	0.009	93.5	0.960	0.019	90.6	1.267	0.009	91.5
26.8	0.172	0.003	90.5	0.332	0.009	90.5	0.646	0.014	89.3	0.908	0.048	85.8	1.226	0.083	88.6
30.9	0.168	0.006	88.5	0.322	0.011	87.8	0.635	0.004	87.7	0.906	0.005	85.6	1.187	0.027	85.7
$\tilde{C}_i^{Tot}$ [µmol/L]	0.190			0.367			0.724			1.059			1.385		
V_i	7.4%			7.5%			7.5%			8.5%			7.8%		

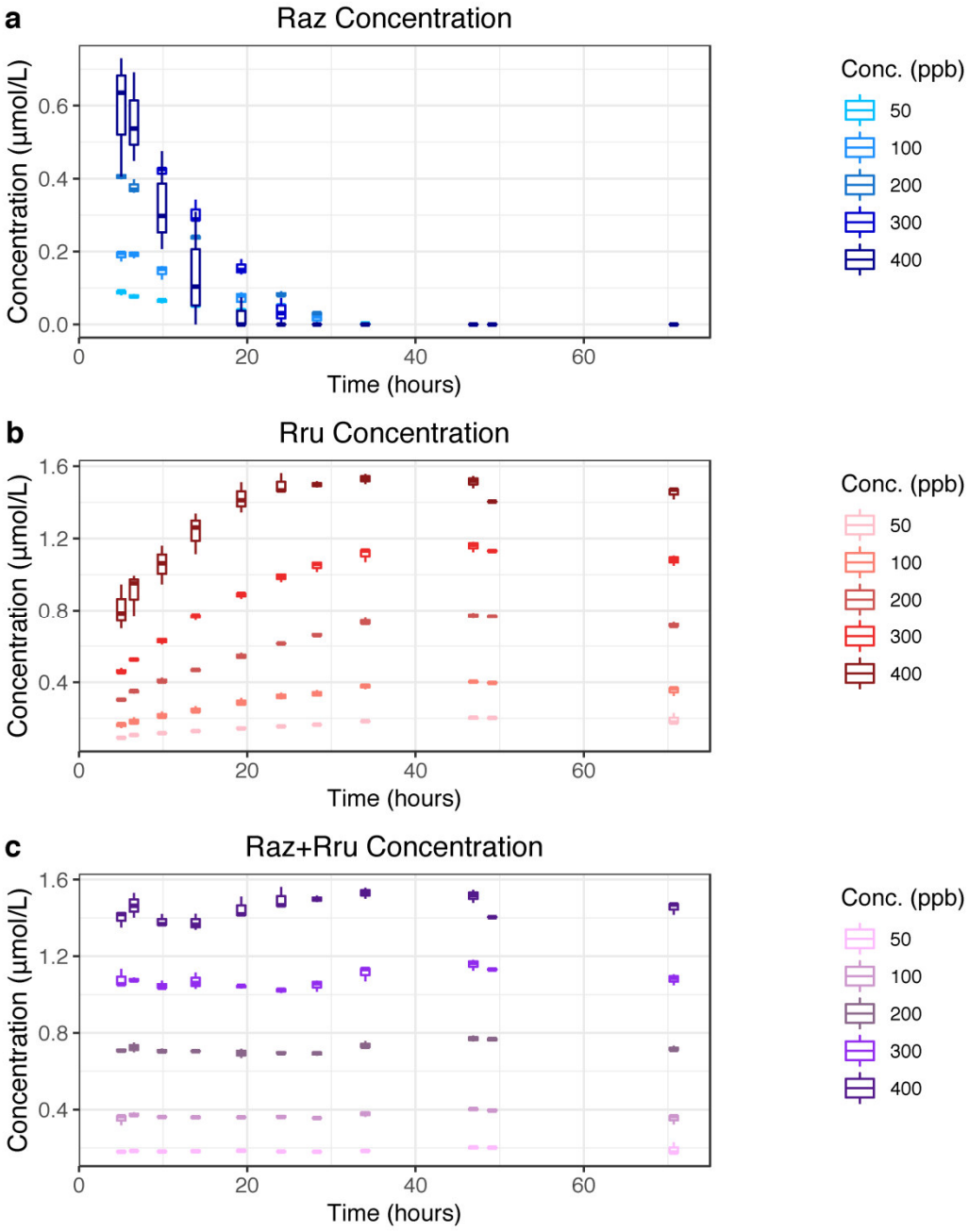

Figure 8.1. Evolutions of a) Raz, b) Rru and c) Raz+Rru molar concentrations during the long experiment with yeast (Exp. 2)

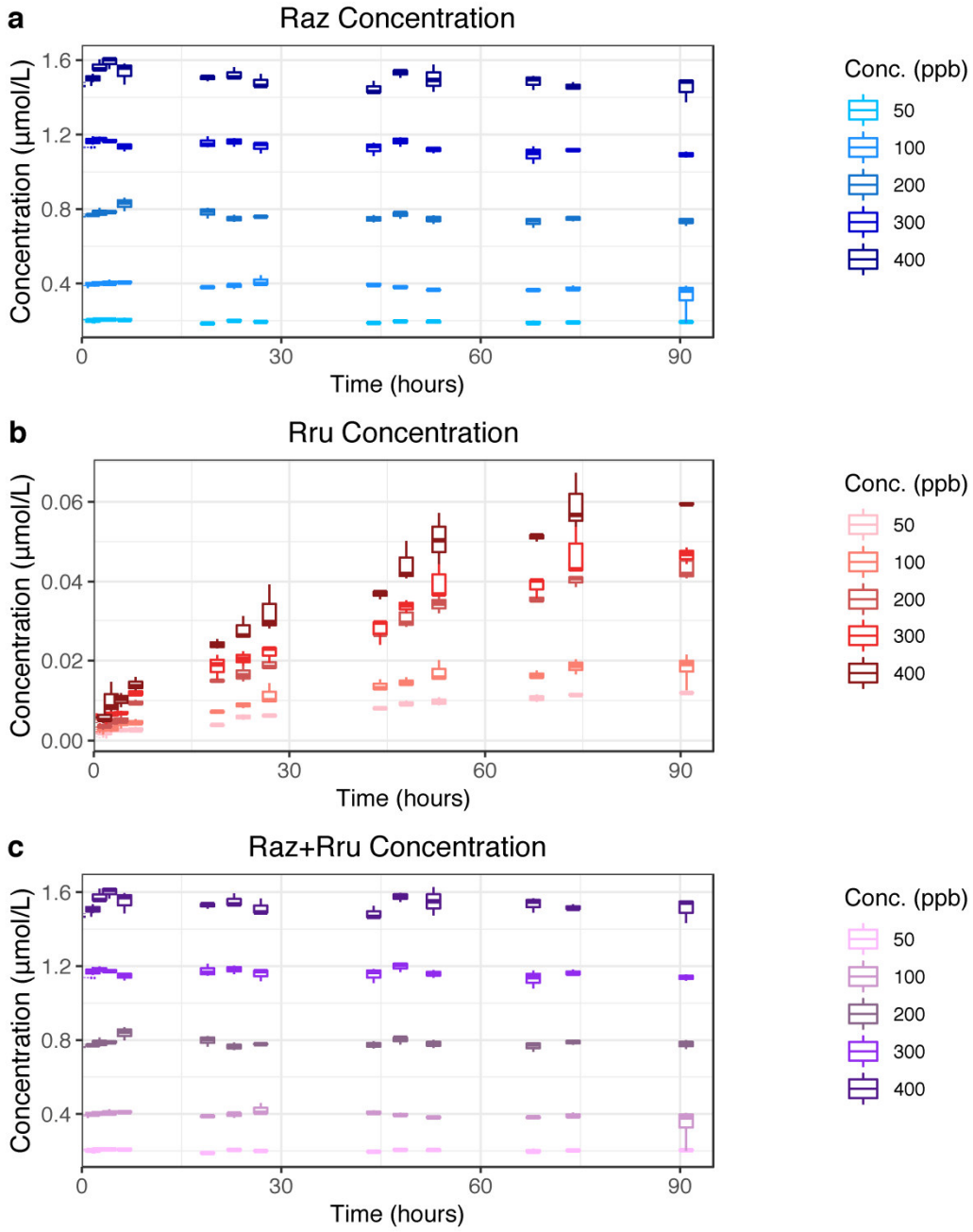

Figure 8.2 Evolutions of a) Raz, b) Rru and c) Raz+Rru molar concentrations during the experiment with Rio Grande water (Exp. 3)

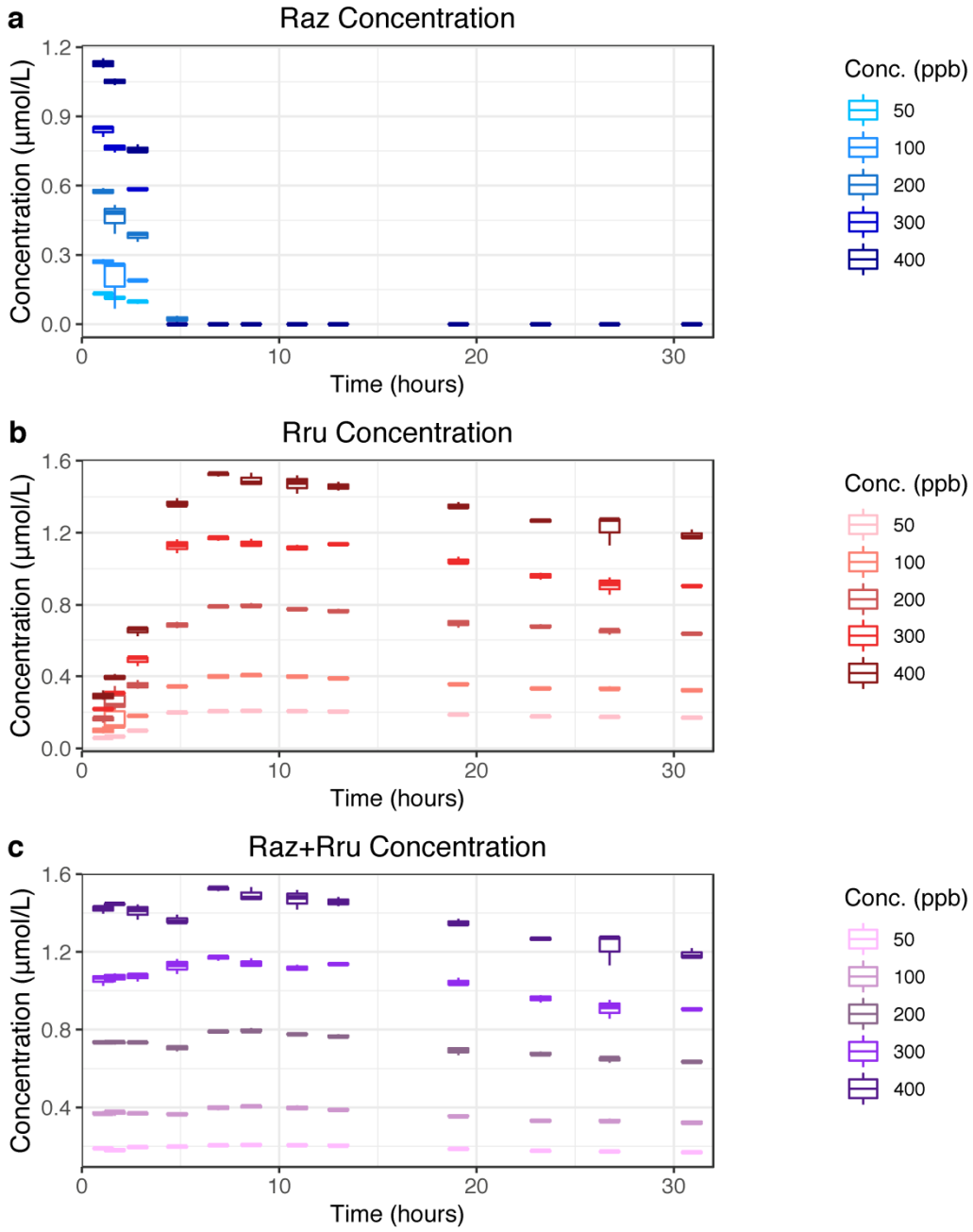

Figure 8.3 Evolutions of a) Raz, b) Rru and c) Raz+Rru molar concentrations during the experiment with *B. subtilis* (Exp. 4)

Acknowledgments

I'd like to thank my supervisor, prof. Andrea Marion, for trusting me and giving me the opportunity to walk this path supported by his suggestions but also leaving me great autonomy. This allowed me going beyond my apparent limits and increasing the awareness about my weakness and my talents. I thank my co-supervisor, prof. Andrea Bottacin-Busolin, for his fundamental contribute on the numerical modelling presented in this thesis, his helpful comments and answers to my research questions, and his personal example on how to be a passionate researcher. I'm sincerely grateful to prof. Ricardo González-Pinzón and his guys I worked with: Peter Regier, Justin Nichols, Jancoba Dorley, Aashis Khandelwal, James Fluke, Nicole Caruana. I obtained excellent research results but much more I acquired confidence with experimental techniques and I could live with you true collaboration spirit and sharing of ideas. I felt part of the team.

I desire to thank all the guys I met in my Department that went along with me in these three years, for few moments or for longer periods, listening to me when frustrated and sharing interesting or funny talks: Andrea Gredelj, Matteo Tregnaghi, Nima Sabokrouhiyeh, Alberto Barausse, Dario Smania, Eleonora Dal Lago, to mention the most present.

And above everything, the greatest thanks goes to my Family, who accepted and supported this path, not always easy and straightforward, and who has always accompanied me with love, not only in these last three years. My Mum Caterina, my Dad Mario, my brother Raffaele and his beautiful family, my sister Valentina with Alessandro, my sister Daniela, you all are essential presences in my life. And Stefano, every single day you were with me, during my dark days, my crazy moments, and my joyful experiences. You help me to know my Truth, to trust more and more in my-self, to explore the real meaning of the words "love" and "freedom". Simply, I'm grateful to have met you.

The Doctorate course has been a challenging path in my Life, arrived by chance and by choice. It represented a journey that allowed me to discover what Life is: to make experience, with love, curiosity and trust.

Eleonora

Ringraziamenti

Vorrei ringraziare il mio supervisore, prof. Andrea Marion, per aver creduto in me ed avermi dato l'opportunità di avanzare in questo percorso supportata dai suoi consigli ma anche per avermi lasciato grande autonomia. Ciò mi ha permesso di superare miei apparenti limiti e di aumentare la consapevolezza dei miei punti deboli e talenti. Ringrazio il mio co-supervisore, prof. Andrea Bottacin-Busolin, per il suo fondamentale contributo alla modellazione numerica presentata in questa testi, per i suoi utili suggerimenti, e per il suo esempio personale di come essere una ricercatore appassionato. Sono sinceramente grata al prof. Ricardo González-Pinzón e ai suoi collaboratori con cui ho lavorato: Peter Regier, Justin Nichols, Jancoba Dorley, Aashis Khandelwal, James Fluke, Nicole Caruana. Ho ottenuto eccellenti risultati nella ricerca, ma principalmente ho acquisito sicurezza nelle tecniche sperimentali ed ho potuto vivere con voi vero spirito di collaborazione e condivisione di idee. Mi sono sentita parte della squadra.

Desidero ringraziare tutti i ragazzi del mio Dipartimento che sono stati al mio fianco in questi tre anni, per pochi momenti o per lunghi periodi, ascoltandomi quando frustrata e condividendo interessanti o divertenti chiacchiere: Andrea Gredelj, Matteo Tregnaghi, Nima Sabokrouhiyeh, Alberto Barausse, Dario Smania, Eleonora Dal Lago, per nominare i più presenti.

E sopra ad ogni cosa, il più grande ringraziamento va alla mia Famiglia, che ha accettato e supportato questo percorso, non sempre facile e lineare, e che mi ha sempre accompagnato con amore, non solo in questi ultimi tre anni. Mamma Caterina, papà Mario, mio fratello Raffaele e la sua splendida famiglia, mia sorella Valentina con Alessandro e mia sorella Daniela, voi tutti siete presenze essenziali nella mia vita. E Stefano, ogni singolo giorno tu eri con me, durante i miei giorni bui, i miei momenti folli, e le mie esperienze gioiose. Tu mi aiuti a riconoscere la mia Verità, ad avere sempre più fiducia in me stessa, ad esplorare il vero significato delle parole "amore" e "libertà". Semplicemente, sono grata di averti incontrato.

Il corso di Dottorato è stato un percorso impegnativo nella mia Vita, arrivato per caso e per scelta. Ha rappresentato un viaggio che mi ha permesso di scoprire che cosa sia la Vita: fare esperienza, con amore, curiosità e fiducia.

Eleonora